

Stellingen behorend bij het proefschrift

Reactiviteitseffecten in een kernreactor van het kogelbedtype

1. Het effect van de eindige meettijd op de Feynman- α methode is belangrijker dan dat van de kanaalophoogtijd van een meerkanaals analysator.
Y. Yamane en Y. Hayashi, Ann. Nucl. Energy, 22 533-542 (1995), dit proefschrift, par. 2.4 en 6.2
2. De door Misawa e.a. voorgestelde methode om tot een groter aantal combinaties van korte teltijden te komen dan gebruikelijk is in een Feynman- α analyse, is niet correct.
T. Misawa e.a., Nucl. Sci. & Eng. 104 53-65 (1990)
3. Het gebruik van de Simmons-King methode verdient de voorkeur boven de Gozani methode om gepulste-neutronenbronexperimenten te analyseren.
Dit proefschrift, par. 2.3
4. In plaats van de reactiviteit zou de vervalconstante van de promptneutronen gebruikt moeten worden om berekeningen met kinetische experimenten te vergelijken.
T. Williams, 'The calculation of kinetics data for use in the Simmons-King Analysis of Pulsed Neutron Measurements', rapport TM-41-93-36, Paul Scherrer Instituut, Villigen, Switzerland.
5. In tegenstelling tot wat Ratemi en Eshabo beweren, heeft de parameter b van de abc-waarden, die voorkomen in de door hen afgeleide formules voor de coëfficiënten in een alternatieve representatie van de 'inhour'-vergelijking, geen universele waarde voor verschillende typen reactoren.
W.M. Ratemi en A.E. Eshabo, Ann. Nucl. Energy, 25 377-386 (1998)
6. De tweede fase in de onderwijsvernieuwing, waarin de vrije pakketkeuze vervangen wordt door een keuze uit vier profielen, dient te worden gevolgd door een derde fase waarin verplicht examen wordt gedaan in alle vakken.
7. Een opleiding kan pas op studeerbaarheid worden beoordeeld nadat er een goede toelatingselectie heeft plaatsgevonden.
8. Ludieke stellingen horen in het theater thuis.
9. Het monteren van zogenaamde bull-bars op auto's moet worden verboden.
10. De begrippen tolerantie en onverschilligheid worden vaak door elkaar gehaald.
11. Met nucleaire energie wordt zorgvuldiger omgesprongen dan met seksuele energie.
12. Het belangrijkste verschil tussen het oosten en westen van Nederland is de afstand tot de Noordzee.

Propositions belonging to the thesis

Reactivity effects in a pebble-bed type nuclear reactor

1. The effect of the finite measurement time on the Feynman- α method is more important than that of the channel advance time of a multi-channel scaler.
Y. Yamane and Y. Hayashi, Ann. Nucl. Energy, 22 533-542 (1995), this thesis, sections 2.4 and 6.2
2. The method proposed by Misawa et al. to achieve a larger number of combinations of short counting intervals than is usual in Feynman- α analysis, is not correct.
T. Misawa et al., Nucl. Sci. & Eng. 104 53-65 (1990)
3. To analyse pulsed neutron source experiments, the Simmons-King method rather than the Gozani method is the analysis technique to be preferred.
This thesis, section 2.3
4. Instead of the reactivity, the prompt neutron decay should be the point of comparison between calculations and kinetic experiments.
T. Williams, 'The calculation of kinetics data for use in the Simmons-King Analysis of Pulsed Neutron Measurements', report TM-41-93-36, Paul Scherrer Institute, Villigen, Switzerland.
5. In contrast to the claim of Ratemi and Eshabo, the parameter b of the abc -values, appearing in the formulas which they have derived for the coefficients of an alternative representation of the 'inhour'-equation, does not have an universal value for different reactor types.
W.M. Ratemi and A.E. Eshabo, Ann. Nucl. Energy, 25 377-386 (1998)
6. The second phase in the education renewal comprising a replacement of a free choice of courses by a choice of four profiles, should be followed by a third phase in which an examination in all courses is compulsory.
7. A training can only be judged on so-called 'studibility' in case a sound admission selection has taken place.
8. Playful propositions belong in the theatre.
9. The mounting of so-called bull-bars on cars should be forbidden.
10. The ideas of tolerance and indifference are often confused.
11. Nuclear energy is more carefully managed than sexual energy.
12. The most important difference between the regions in the east and west of The Netherlands is the distance to the North Sea.

12.01.2012
3.1.2012
10.01.2012

3165
3103
TR3165

Reactivity effects in a pebble-bed type nuclear reactor

An experimental and calculational study

**Reactiviteitseffecten in een kernreactor
van het kogelbedtype**

Een experimentele en numerieke studie

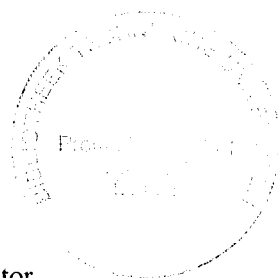


The research described in this thesis was performed within the unit General Reactor Physics of the Reactor Physics Department of the Interfaculty Reactor Institute, Delft University of Technology, Mekelweg 15, 2629 JB Delft, The Netherlands. This research has been supported by the Ministry of Economic Affairs in the framework of PINK (Programme to maintain nuclear competence).

Reactivity effects in a pebble-bed type nuclear reactor

An experimental and calculational study

PROEFSCHRIFT



ter verkrijging van de graad van doctor
aan de Technische Universiteit Delft,
op gezag van de Rector Magnificus Prof. ir. K.F. Wakker,
in het openbaar te verdedigen ten overstaan van een commissie,
door het College voor Promoties aangewezen,
op maandag 22 juni 1998 te 13.30 uur
door

Erik Johannes Maria WALLERBOS

natuurkundig ingenieur
geboren te Lichtenvoorde

Dit proefschrift is goedgekeurd door de promotor:
Prof. dr. ir. H. van Dam

Toegevoegd promotor:
Dr. ir. J.E. Hoogenboom

Samenstelling promotiecommissie:

Rector Magnificus, voorzitter

Prof. dr. ir. H. van Dam, Technische Universiteit Delft, promotor

Dr. ir. J.E. Hoogenboom, Technische Universiteit Delft, toegevoegd promotor

Prof. dr. K. Kugeler, Rheinisch-Westfälische Technische Hochschule Aachen, Duitsland

Prof. dr. R. Chawla, Ecole Polytechnique Fédérale de Lausanne, Zwitserland

Prof. dr. ir. A.H.M. Verkooijen, Technische Universiteit Delft

Prof. dr. ir. C.W.E. van Eijk, Technische Universiteit Delft

Prof. dr. I.T. Young, Technische Universiteit Delft

Published and distributed by:

Delft University Press

Mekelweg 4

2628 CD Delft

~~The Netherlands~~

Telephone +31 15 2783254

Fax +31 15 2781661

E-mail: DUP@DUP.TUDELFT.NL

ISBN 90-407-1662-5 / CIP

NUGI: 841

Copyright © 1998 by E.J.M. Wallerbos

All rights reserved. No part of the material protected by this copyright notice may be reproduced or utilized in any form or by any means, electronic or mechanical, including photocopying, recording or by any information storage and retrieval system, without permission from the publisher: Delft University Press.

Printed in the Netherlands

CONTENTS

| | |
|---|----|
| 1. INTRODUCTION | 1 |
| 1.1 HTR-PROTEUS | 6 |
| 1.2 CORE CONFIGURATIONS | 7 |
| 1.3 OUTLINE OF THE THESIS | 8 |
| REFERENCES | 9 |
| 2. REACTIVITY MEASUREMENT TECHNIQUES | 11 |
| 2.1 KINETIC REACTOR MODEL | 12 |
| 2.2 INVERSE KINETICS TECHNIQUE | 16 |
| 2.2.1 Correction factors | 16 |
| 2.2.2 Special case of inverse kinetics: the stable period technique ... | 18 |
| 2.2.3 Experimental details | 19 |
| 2.3 PULSED NEUTRON SOURCE TECHNIQUE | 21 |
| 2.3.1 Area-ratio methods | 21 |
| 2.3.2 Inhour methods | 23 |
| 2.3.3 Experimental details | 23 |
| 2.4 NOISE TECHNIQUES | 24 |
| 2.4.1 Introduction to the theory of selected noise analysis techniques | 24 |
| 2.4.2 First and second order moments of the neutron distribution ... | 25 |
| 2.4.3 Feynman- α technique | 28 |
| 2.4.4 Bennets δ -variance technique | 30 |
| 2.4.5 Covariance technique | 30 |
| 2.4.6 Auto-correlation technique | 31 |
| 2.4.7 Cross-correlation technique | 32 |
| 2.4.8 Effect of the finite measurement time in subcritical systems ... | 33 |
| 2.4.9 Experimental details | 37 |
| 2.4.10 Conclusions | 38 |
| REFERENCES | 38 |
| APPENDIX | 41 |
| 3. THE KINETIC PARAMETER β_{eff}/Λ | 43 |
| 3.1 INTRODUCTION | 43 |
| 3.2 THEORY | 43 |
| 3.2.1 The k-eigenvalue | 44 |
| 3.2.2 The α -eigenvalue | 45 |
| 3.2.3 The derivation of the point-kinetics equations | 45 |
| 3.3 THE CALCULATION OF THE KINETIC PARAMETERS | 46 |
| 3.3.1 The choices of the weighting and shape functions | 47 |
| 3.3.2 Calculational methods | 47 |
| 3.4 THE KINETIC PARAMETER β_{eff}/Λ AT CRITICAL | 50 |
| 3.4.1 Calculation of β_{eff}/Λ | 50 |
| 3.4.2 Measurement of β_{eff}/Λ | 51 |
| 3.4.3 Results | 53 |
| 3.4.4 Discussion and conclusions | 55 |
| REFERENCES | 57 |

| | |
|---|--------|
| 4. CRITICAL BALANCES OF CORE CONFIGURATIONS | 59 |
| 4.1 COMPUTATIONAL METHODS | 59 |
| 4.1.1 INAS - the IRI reactor physics code system | 59 |
| 4.1.2 Calculation of the Dancoff factor | 61 |
| 4.1.3 The cross-section generation procedure | 62 |
| 4.2 MODELLING HTR-PROTEUS | 64 |
| 4.2.1 Two-dimensional model in deterministic codes | 64 |
| 4.2.2 Three-dimensional model in KENO-Va | 66 |
| 4.3 RESULTS | 66 |
| 4.3.1 Homogenised core region | 66 |
| 4.3.2 Explicit modelling of pebbles | 67 |
| 4.4 STREAMING CORRECTION IN DIFFUSION THEORY | 67 |
| 4.5 DISCUSSION AND CONCLUSIONS | 68 |
| REFERENCES | 69 |
| 5. THE SPATIALLY DEPENDENT REACTIVITY EFFECTS OF VARIOUS SMALL SAMPLES | 71 |
| 5.1 EXPERIMENTAL SET-UP | 71 |
| 5.1.1 The samples oscillated | 71 |
| 5.1.2 The instrumentation | 72 |
| 5.1.3 Data processing | 74 |
| 5.2 EVALUATION OF THE USE OF DIFFERENT EXPERIMENTAL PROCEDURES | 75 |
| 5.2.1 Dynamic effects | 75 |
| 5.2.2 Effect of the low-pass filter | 76 |
| 5.2.3 Validity of point-kinetic theory | 77 |
| 5.2.4 Conclusions | 78 |
| 5.3 CALCULATIONS | 78 |
| 5.3.1 Flux distributions | 79 |
| 5.3.2 The reactivity effect of a sample | 81 |
| 5.4 RESULTS | 83 |
| 5.4.1 The fission rates | 83 |
| 5.4.2 The reactivity effects of the samples | 87 |
| 5.5 DISCUSSION AND CONCLUSIONS | 96 |
| REFERENCES | 98 |
| 6. THE REACTIVITY WORTH OF REFLECTOR-BASED ABSORBER RODS | 99 |
| 6.1 AN OVERVIEW OF ABSORBER RODS | 99 |
| 6.2 AN INTERCOMPARISON OF THREE DIFFERENT ROD-WORTH MEASUREMENT TECHNIQUES | 101 |
| 6.2.1 Introduction | 101 |
| 6.2.2 The calculation of kinetics parameters and correction factors | 102 |
| 6.2.3 Results | 103 |
| 6.2.4 Conclusions | 108 |

| | |
|--|---------|
| 6.3 THE REACTIVITY WORTH OF THE AUTO-ROD | 109 |
| 6.3.1 Calculations | 109 |
| 6.3.2 Measurements | 110 |
| 6.3.3 Results | 110 |
| 6.4 THE REACTIVITY WORTH OF THE FINE CONTROL RODS | 112 |
| 6.4.1 Calculations | 112 |
| 6.4.2 Measurements | 112 |
| 6.4.3 Results | 113 |
| 6.5 THE REACTIVITY WORTH OF THE SHUTDOWN RODS | 115 |
| 6.5.1 Calculation of the rod worth | 115 |
| 6.5.2 Measurement of the rod worth | 116 |
| 6.5.3 Calculation of correction factors | 117 |
| 6.5.4 Results | 121 |
| 6.6 DISCUSSION AND CONCLUSIONS | 124 |
| REFERENCES | 125 |
| 7. EFFECTS OF ACCIDENTAL WATER INGRESS | 127 |
| 7.1 INTRODUCTION | 127 |
| 7.2 EFFECT ON THE KINETIC PARAMETER $\beta_{\text{eff}}/\Lambda$ | 128 |
| 7.3 EFFECT ON THE MULTIPLICATION CONSTANT | 128 |
| 7.4 EFFECT ON REFLECTOR-BASED ABSORBER-RODS | 129 |
| 7.5 SIMULATION OF WATER INGRESS IN CORE 5 | 130 |
| 7.6 SUMMARY | 132 |
| REFERENCES | 132 |
| SUMMARY | 133 |
| SAMENVATTING | 137 |
| LIST OF PUBLICATIONS | 141 |
| CURRICULUM VITAE | 143 |
| ACKNOWLEDGEMENT | 145 |

Chapter 1

Introduction

There is a renewed interest in the high-temperature reactor (HTR) in several countries, e.g. in Indonesia, where design studies are made of modularised, small-size HTRs [1], and in the Republic of South Africa, where a techno-economic evaluation is made of a modular HTR with a direct cycle power conversion [2]. In the Netherlands, the ministry of economic affairs had the applicability of the HTR in the Netherlands investigated [3], and in 1997, the INCOGEN (Inherently safe Nuclear COGENeration) design was presented [4]. In this design, the production of both electricity and heat is foreseen, leading to an overall plant efficiency of about 90%. In China and Japan, test reactors are under construction. The HTR-10 in China is a small HTR (10 MWth) planned to become operational in the beginning of 1999 [5] whereas the first criticality of the HTTR (30 MWth) in Japan is scheduled for the end of 1997 [6].

This renewed interest in the HTR is mainly the result of the growing demand for an enhancement of the safety standards of nuclear plants, which can be fulfilled by the inherent safety characteristics of the HTR. Furthermore, the power conversion efficiency is higher than that of a light-water reactor (LWR), leading to a more efficient use of the fuel. This is the result of the higher coolant outlet temperature in the HTR: about 900 °C compared to about 300 °C in a LWR. The inherent safety characteristics of the HTR are the result of several design features, e.g.

- the use of coated fuel particles embedded in a graphite matrix which practically completely retain the fission products up to a fuel temperature of 1600 °C, as confirmed by experiments [7]
- the use of graphite as both moderator for the neutrons and as construction material. In contrast to metals, graphite does not melt. Furthermore, its sublimation point is at a very high temperature (about 5100 K at atmospheric pressure)
- the use of helium as coolant
- the low power density (2 to 6 MW/m³, compared to at least 50 MW/m³ for a LWR)
- a continuous fuel supply in case the core consists of spherical fuel elements, limiting the excess reactivity in the core to a minimum

Because of the excellent retention capabilities of the coated fuel particles (figure 1.1), very high burn-ups are possible and the coolant circuit remains practically free of contamination. Helium is chosen as coolant because it hardly absorbs neutrons, is not activated by neutrons, is chemically inert, does not undergo a phase change, has good heat-exchange properties, and is naturally available in sufficient quantities.

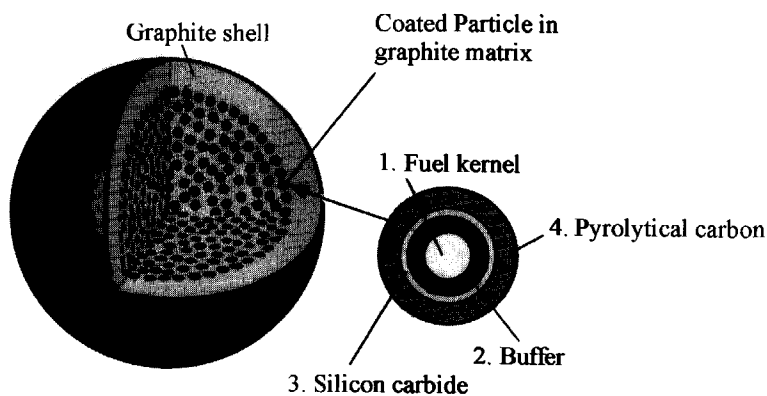


Figure 1.1 Spherical fuel element and coated fuel particle

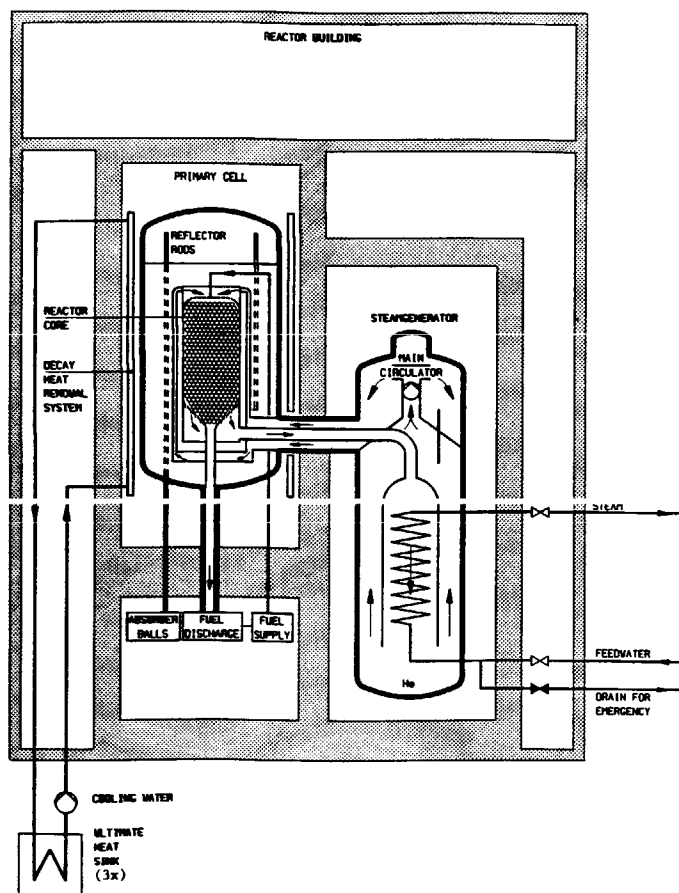


Figure 1.2 Sectional view of the HTR-M, a modular, low power version of the HTR concept

If the core of an HTR consists of spherical fuel elements (fuel pebbles, see figure 1.1), the core cavity at start-up is filled with just enough fuel pebbles to make the system critical and to take it to full power. During operation, the reactivity decrease due to burn-up of fuel is compensated by continuously adding fresh fuel pebbles. In this way, the excess reactivity is kept minimal and large reactivity accidents are not to be expected. In the past, three different fuelling strategies have been considered:

1. the multipass scheme. In this scheme pebbles are continuously added from the top, and simultaneously pebbles are extracted at the bottom. The burn-up of extracted pebbles is measured and in case the target burn-up has not been reached yet, the pebbles are re-circulated and will (later) be added to the core again (from the top). In this scheme, the pebbles pass the core numerous times before being discarded. It was applied in the AVR where a single pass through the core took about half a year and a pebble passed the core ten times on average [8]. It is also proposed for the HTR-M, see figure 1.2. The multipass scheme allows an optimal control of the burn-up for each individual pebble but also requires complex refuelling equipment, e.g. equipment for burn-up measurement, pebble re-circulation, and extraction of burnt-up elements.
2. the Once-Through-Then-Out (OTTO) scheme. This scheme is similar to the multipass scheme. The difference is that the extracted pebbles are immediately discarded, thus avoiding the need of the equipment for burn-up measurement and pebble re-circulation. If this scheme is applied, the pebbles pass the core only once.
3. the peu-à-peu scheme. In contrast to the multipass and OTTO schemes, in this scheme no pebbles are extracted from the core during operation. Hence, the core height increases steadily. After the core cavity is completely filled, the reactor is shutdown and the cavity is entirely unloaded. This strategy is foreseen in the INCOGEN design, where just after start-up about two pebbles per hour have to be added and at the end of the cycle about one pebble per two hours. Shutdown of the reactor is anticipated every ten years.

The multipass and OTTO schemes require extra equipment compared to the peu-à-peu scheme but avoid the necessity for reactor shutdown for refuelling. An HTR with prismatic block-type fuel elements (figure 1.3), like the HTTR, is just like a LWR loaded with an amount of fuel required for continuous operation for a period of about one year. As a result, the excess reactivity at the beginning of the cycle is considerable and is normally compensated by adding neutron absorbing material to the fuel elements (burnable poisons, like boron carbide and gadolinium oxide).

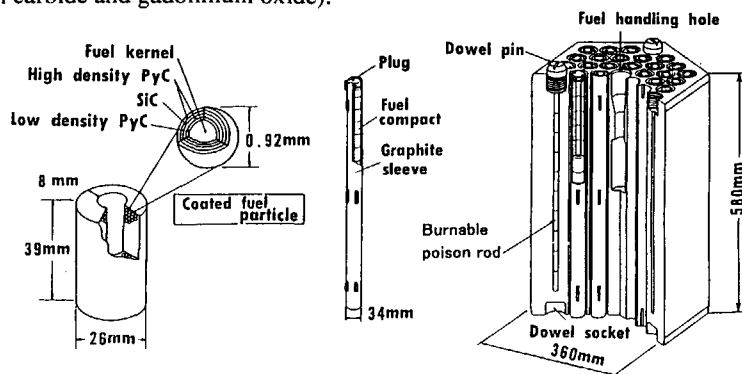


Figure 1.3 Prismatic block-type fuel element as used in the HTTR

One of the most important safety requirements for reactor designs is the removal of decay heat from the reactor core in the case of an accident in order to prevent serious damage to the reactor and the release of radioactivity into the environment. First of all, the HTR core is temperature resistant, as only ceramic materials are used. Furthermore, due to the large amounts of graphite in an HTR, the core has a very high heat storage capacity, which is retained in the case of a loss-of-coolant accident. In such an accident, the combination of the large amounts of graphite and the low power density ensure a self-acting decay heat removal (by thermal radiation, heat conduction and free convection) and a maximum fuel temperature that remains within an acceptable range. Hence, the HTR excludes melting of the core and the release of radioactive fission products from the fuel elements under all conceivable accident conditions and thus satisfies the requirements of catastrophe-free nuclear technology [9].

The HTR concept is by no means new but originates in the late 1950s. It was further developed and tested in a number of critical experiments (for example in the KAHTER facility in Germany [10]) and test reactors, like the 20 MWth DRAGON reactor in England [11], the 115 MWth Peach Bottom reactor in the USA [12], and the 46 MWth AVR pebble-bed reactor in Germany [8,13]. The first two test reactors employed a prismatic core, whereas the core of the AVR consisted of a randomly packed bed of fuel pebbles. Later, two much larger test reactors were built: a prismatic block-type HTR in Fort St. Vrain (Colorado, USA) of 842 MWth [14] and the THTR-300 (figure 1.2) in Uentrop-Schmehausen (Germany), a pebble-bed type HTR of 750 MWth [8,15]. These reactors demonstrated the feasibility of the HTR concept and confirmed the favourable characteristics claimed for it.

All previously mentioned test reactors used high-enriched uranium (HEU) and thorium as fertile material. Furthermore, the prototype designs, except for the DRAGON reactor, had a large core diameter (3 - 6 m), as a result of which it was necessary to have control rods in the core region itself. Particularly in the pebble-bed systems, this involved a number of serious engineering difficulties centred around the practical problem of rapidly inserting control rods through the pebble-bed without damaging the fuel. To avoid these difficulties, the AVR had no control rods in the pebble bed itself, but they were moved within so-called graphite noses, protruding into the core. In new designs, like the modular-HTR [16] and INCOGEN [4], the core diameter is reduced. This increases the neutron leakage to the reflector so that control rods in the reflector suffice and control rods in the core region are no longer required. Also, with priorities having shifted from fuel conservation to non-proliferation, the new designs use low-enriched uranium (LEU) with ^{235}U instead of ^{233}U as fertile material.

Although some measurements were made in LEU systems, there was a perceived need for integral physics data relating to small-sized, LEU-HTR systems, against which design and safety evaluation procedures could be validated. To fill the gap in the validation database, a programme of integral experiments at the PROTEUS facility of the Paul Scherrer Institute in Switzerland, was designed. From July 1992 to July 1996, this programme was carried out, comprising investigations of the safety-related reactor physics properties of LEU-HTR systems. In particular, properties relating to the effects of neutron streaming and of accidental water ingress on the criticality and neutron balance components of typically undermoderated cores and on the reactivity effect of control rods situated in the radial reflector were of importance [17]. Table 1.1 summarises the configurations investigated and gives an impression of the investigations conducted and the corresponding measurements made.

Table 1.1. Summary of the configurations investigated and measurements made

| | | | | SUBCRIT CORE | SHUTDOWN RODS | | | CONTROL RODS | | UPPER REFL | β/A | MEAS RODS | CENT CONT ROD |
|----------|--------------------------|-----|---------|-----------------|------------------|----|----|-----------------|-----|---------------|-----|--------------|---------------------|
| CORE | DATES | F:M | PACKING | PNS | PNS | IK | SP | PNS | PNS | PNS | PNS | PNS | PNS |
| G1 | 3/92-5/92 | - | - | | | | | | | | | | |
| 1 | 7/92-6/93 | 2:1 | HCP | ✓ | ✓ | ✓ | ✓ | ✓ | | ✓ | | ✓ | |
| 1A | 6/93-8/93, 2/94-3/94 | 2:1 | HCP | | ✓ | ✓ | ✓ | | | | | | |
| 2 | 8/93-10/93 | 2:1 | HCP | | ✓ | ✓ | ✓ | ✓ | ✓ | ✓ | | | |
| G2 | 10/93 | - | - | | | | | | | | | | |
| 3 | 10/93-2/94 | 2:1 | HCP | ✓ | ✓ | ✓ | ✓ | ✓ | | ✓ | | | |
| 4(1,2,3) | 3/94-6/94 | 1:1 | RANDOM | | ✓ | ✓ | ✓ | | | | | | |
| 5 | 7/94-4/95, 11/95-1/96 | 2:1 | P-O-P | | ✓ | ✓ | ✓ | ✓ | ✓ | ✓ | | ✓ | ✓ |
| 6 | 4/95-5/95 | 2:1 | P-O-P | | | | ✓ | | | | | | |
| 7 | 5/95-10/95 | 2:1 | P-O-P | | ✓ | ✓ | ✓ | ✓ | ✓ | ✓ | | ✓ | ✓ |
| 8 | 1/96-2/96 | 2:1 | P-O-P | | | | | ✓ | | | | | |
| 9 | 2/96-5/96 | 1:1 | P-O-P | | | ✓ | ✓ | ✓ | ✓ | ✓ | | ✓ | |
| 10 | 5/96-6/96 | 1:1 | P-O-P | ✓ | | ✓ | ✓ | ✓ | ✓ | ✓ | | ✓ | |

F:M = fuel-to-moderator ratio

HCP = hexagonal close packed

P-O-P = point-on-point (column hexagonal)

PNS = pulsed-neutron source

IK = inverse kinetics

SP = stable period

✓ = planned and executed

Table 1.1. cont'd.

| | TEMP. COEFF | COM- PONENT WORTHIS | REACTION RATE DISTRIBUTIONS | | | | REACTION RATE RATIOS | | | |
|----------------|----------------|---------------------------|--------------------------------|--------------------|------------------|----------------|-------------------------|----------------|-------------------|-----------------|
| | | | IN CORE | | | IN PEBBLE | | AT CORE CENTRE | | |
| METHOD CORE | COMP | COMP | FOILS | FISSION CHAMBER | γ SCAN | FOILS | PARTICLE FOILS | FOILS | PARTICLE FOILS | WHOLE PEBBLE |
| G1 | | | F: 5 C: 8 | F: 5,8,7,9,2,1 | | | | | | |
| 1 | | ✓ | F: 5, 8 C: 8 | F: 5,8,7 | | | | | | |
| 1A | | | | F: 5,8,7 | | | | | | |
| 2 | | | F: 5, 8 C: 8 | F: 5,8,7 | | | | | | |
| G2 | | | | F: 5,8 | | | | | | |
| 3 | | | | | | | | | | |
| 4(1,2,3) | | | | | | | | | | |
| 5 | ✓ | ✓ | F:5, 8 C8 | F:5,8,7 | C8, Ftot | F: 5,8,9 C8 | Ftot C8 | F:5,8,9 C8 | C8/Ftot | C8/Ftot |
| 6 | | | | | | | | | | |
| 7 | ✓ | | F:5, 8 C8 | F:5,8,7 | C8, Ftot | F: 5,8,9 C8 | Ftot C8 | F:5,8,9 C8 | C8/Ftot | C8/Ftot |
| 8 | | | | | | | | | | |
| 9 | | | F:5 | F:5,8,7,9 | C8, Ftot | F: 5,8,9 C8 | | | | |
| 10 | | | F:5 | F:5,8,7,9 | C8, Ftot | F: 5,8,9 C8 | | | | |

F=fission, C=capture, 5=U-235, 8=U-238, 9=Pu-239, 7=Np-237, 2=Pu-242, G2=graphite (no fuel in core), COMP. = compensation with calibrated control rods

This experimental programme played a central role in an IAEA Co-ordinated Research Programme (CRP) [18], in which eight separate institutes, representing seven countries, were actively involved. The work described in this thesis was also performed within the framework of the CRP. It comprises both theoretical and experimental investigations of reactivity effects in HTR-PROTEUS. A description of the facility can be found in section 1.1, which is followed by an overview in section 1.2 of all core configurations in which the experiments described in this work, were conducted. These experiments were additional and/or complementary to the main programme summarised in table 1.1. Section 1.3 gives an outline of the thesis.

1.1 HTR-PROTEUS

A schematic side view of the HTR-PROTEUS facility is shown in figure 1.4. The system can be described as a graphite cylinder of 3.26 m diameter and 3.3 m height with a cylindrical cavity with a radius of 62.5 cm and ~170 cm in height located 78 cm above the base of the system. The core region consists of moderator (pure graphite) and fuel (16.7% enriched) HTR-type pebbles¹ of 6 cm diameter, arranged in either deterministic or random arrangements. The deterministic loadings were chosen to improve the benchmarking quality of the measurements and for experimental convenience. Above the pebble-bed is a cavity of typical height 70 cm (depending on the particular configuration) surmounted by an upper graphite reflector of thickness 78 cm. As the maximum power is limited to 1 kW, no active cooling systems are required.

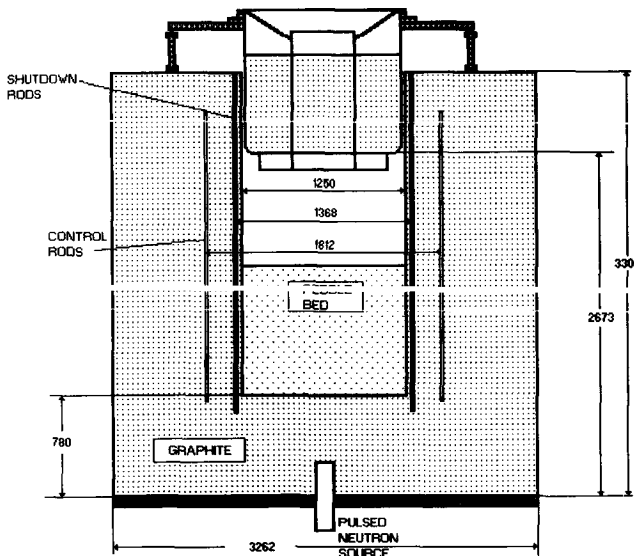


Figure 1.4. A schematic side view of the HTR-PROTEUS facility (dimensions in mm)

¹ originally intended for use in the AVR

Shutdown of the reactor is achieved by means of borated-steel rods situated in the radial reflector at a radius of 68 cm. In total there are eight, identical rods divided into two groups of four rods each. One of these groups is selected as the safety rod group and the other as the shutdown rod group. Also situated in the radial reflector but at a radius of 90 cm, are four withdrawable stainless-steel rods (the fine control rods) which are used for reactor control. Criticality can be maintained by means of an automatic control rod (autorod) positioned at a similar radius as the fine control rods. More detailed information about the facility can be found elsewhere [19].

1.2 Core configurations

The four cores discussed in this work were all columnar-hexagonal (orthorhombic) pebble lattices with a filling factor of 0.6046. The simulation of accidental water ingress conditions was achieved using polyethylene (CH_2) rods inserted into the vertical inter-pebble channels, see figure 1.5. Note that in the columnar-hexagonal packing geometry with 6 cm diameter pebbles, the inter-pebble channels have a diameter of 9 mm in the vertical direction and 19.7 mm in the horizontal direction.

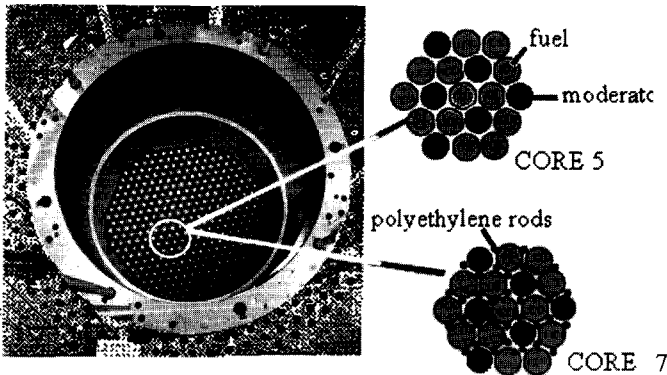


Figure 1.5. A view from above of HTR-PROTEUS with the upper reflector removed. Also indicated are the columnar-hexagonal loading patterns of cores 5 and 7 with a moderator-to-fuel pebble ratio of 1:2. Core 7 is the same as core 5 but with water-ingress simulation.

Cores 5 and 7 had a moderator-to-fuel pebble ratio of 1 to 2, whereas in cores 9 and 10 this ratio was 1:1. The actual value of the ratio may be slightly different because of the presence of a partially fuelled top layer. Such a layer was sometimes required to achieve a critical balance within the range of the fine control rods. Cores 7 and 10 were variants of cores 5 and 9, respectively, with polyethylene rods inserted to simulate water-ingress conditions. In core 7, these rods had a diameter of 8.3 mm, whereas in core 10, the rod diameter was only 6.5 mm. Hence, the rods occupied 8.8 % and 5.4 % of the inter-pebble volume in core 7 and 10, respectively. Table 1.2 summarises some characteristic figures of the four cores. More detailed information about the core configurations can be found elsewhere [20].

-
- [6b] Shiozawa S., "Status of HTTR Project", Proc. (working material) 13th Mtg. of the International Working Group on Gas Cooled Reactors, 26-28 March 1996, Vienna, Austria
- [7] Schenk W. et.al., "Fission Product Release Profiles from Spherical HTR-Fuel Elements at Accident Temperatures", *Kernforschungsanlage Jülich*, Jül-2234, Jülich (1988)
- [8] Kugeler K. and Schulten R., "Hochtemperaturreaktortechnik", Springer-Verlag, Berlin (1989)
- [9] Kugeler K. and Philippen P.W., "The potential of the self-acting safety features of high-temperature reactors", *Kerntechnik* **61** (5-6) 239-244 (1996)
- [10] Drücke V. and Filges D., "The Critical HTGR Test Facility KAHTER - An Experimental Program for Verification of Theoretical Models, Codes and Nuclear Design Bases", *Nucl. Sci. & Eng.* **97** 30 (1987)
- [11] Della Loggia V.E. et al., "Zero Energy Experiments on the Dragon Reactor Prior to Charge IV Startup", DP820, Dragon Project, AEEW, Winfrith, UK, (1973)
- [12] Preskitt C.A and Nephew E.A., "Interpretation of Pulsed Source Experiments in the Peach Bottom HTGR", *Nucl. Sci. & Eng.* **29** 283-295 (1967)
- [13] Knüfer H., "Preliminary operating experiences with the AVR at an average hot gas temperature of 950 °C", *Nucl. Eng. & Design* **34** (1975)
- [14] Brown J.R. et al., "Physics Testing at Fort St. Vrain - A Review", *Nucl. Sci. & Eng.* **97** 104 (1987)
- [15] Brandes S. et al., "Core Physics Tests of Thorium High-Temperature Reactor (THTR) Pebble-Bed Core at Zero Power", *Nucl. Sci. & Eng.* **97** 89 (1987)
- [16] Lohnert G.H., "Technical Design Features and Essential Safety Related Properties of the HTR-Module", *Nucl. Eng. & Design* **121** 259-275 (1990)
- [17] Chawla R., "Generic Reactor Physics Studies in the Framework of the PROTEUS LEU-HTR Programme", *Invited Paper IXth Brazilian Mtg. on reactor physics and Thermal Hydraulics*, Oct 25-29 1993, Caxambu, Brazil.
- [18] Scherer W., "Summary of Discussions on the Future HTGR PROTEUS Experiments and Other Planned Experiments", IAEA Specialists' Meeting, Villigen, 1990; *proc IAEA-IWGGCR/24* p. 145 (1991)
- [19] Mathews D. and Williams T., "LEU-HTR PROTEUS System Component Description", *PSI Internal report TM-41-93-43*, November 1996
- [20] Williams T., "LEU-HTR PROTEUS: Configuration Descriptions and Critical Balances for the Cores of the HTR-PROTEUS Experimental Programme", *PSI Internal report TM-41-95-18*, November 1996
- [21] Duderstadt J.J. and Hamilton L.J., "Nuclear Reactor Analysis", John Wiley & Sons, New York, 1976, p. 324

Chapter 2

Reactivity measurement techniques

The reactivity of a system quantifies the balance between the neutron production and destruction rates and is thus directly related to the rate at which the neutron population changes in a multiplying system without a neutron source. With a detector, the time dependence of the neutron population can be measured but not the reactivity. Hence, a model which describes the kinetic behaviour of the neutron population is needed to convert the measured time dependence to the reactivity. Section 2.1 deals with the kinetic reactor model which is used in all three applied reactivity measurement techniques. These techniques, namely the inverse-kinetics (IK) technique, the Pulsed Neutron Source (PNS) technique, and noise analysis techniques, were selected as they are complimentary to each other:

- both IK and PNS determine the reactivity by measuring the response of the reactor to an external perturbation, namely a change in reactivity (e.g. by control rod movements) and a pulse of neutrons from an external neutron source, respectively. In noise measurements, on the other hand, the reactivity is derived from the fluctuations in the detector signal which are due to the inherent fluctuations in the fission process.
- The PNS and noise analysis techniques are sensitive to the decay of the prompt neutrons and hence to the generation time, whereas the IK technique is very insensitive to the value of the generation time (but sensitive to the delayed neutron parameters).
- IK can be regarded as a dynamic technique (i.e. the measurement always starts in a critical state and then the reactivity is changed by, for example, moving a control rod) whereas both PNS and noise are static techniques, i.e. these techniques can be applied directly to a subcritical configuration without reference to the critical state.

These techniques are all well-known techniques and are extensively described in the literature, for example IK in Ref. 1-10, PNS in Ref. 11-21, and noise analysis in Ref. 25-30. The IK and PNS techniques were already chosen as standard measurement techniques at HTR-PROTEUS. Therefore, a detailed description of the theory, execution and analysis of these two techniques as they are applied to the PROTEUS experiments can be found elsewhere [9]. However, for completeness, they are reviewed briefly in sections 2.2 and 2.3, respectively. The application of noise analysis in HTR-PROTEUS was introduced by the author. Although the techniques are well-known, some shortcomings were discovered, see section 2.4.

2.1 Kinetic reactor model

The basic equation in reactor physics is the transport equation. In general, however, this equation is far too complicated to solve analytically or numerically, and therefore one usually resorts to approximations. One of the most frequently used approximations for zero-power reactors is the point reactor model, in which all space and energy dependence is neglected, i.e. the whole phase space is contracted to one point. The equations of this model - usually referred to as the kinetic equations - can be written as [32]:

$$\frac{dn(t)}{dt} = \frac{\rho(t) - \beta_{eff}}{\Lambda} n(t) + \sum_{i=1}^6 \lambda_i C_i(t) + Q(t) \quad (2.1)$$

$$\frac{dC_i(t)}{dt} = \frac{\beta_{i,eff}}{\Lambda} n(t) - \lambda_i C_i(t) \quad (2.2)$$

where:

- n is the neutron population in the system
- ρ is the reactivity
- β_{eff} is the effective total fraction of delayed neutrons
- Λ is the generation time
- $\lambda_i, \beta_{i,eff}$ are the decay constant and abundance of delayed neutron precursor group i , respectively
- C_i is the population of delayed neutron precursors of group i
- Q is an external source of neutrons

The effective fraction of delayed neutrons β_{eff} is larger than the actual fraction of delayed neutrons β , since the probability that the delayed neutrons eventually cause a fission is somewhat larger than that of the prompt neutrons. This is due to the lower average energy with which the delayed neutrons are born as compared to the prompt neutrons.

Note that in the kinetic equations, the reactor parameters ρ , β_{eff} , and Λ only occur in ratios. As a consequence, from experiments analysed with methods based on these equations, only ratios like ρ/β_{eff} and Λ/β_{eff} can be determined. For this reason, it is advantageous to introduce the reduced parameters:

$r = \rho/\beta_{eff}$, the reactivity in dollar units

$\Lambda^* = \Lambda/\beta_{eff}$, the reduced generation time

$b_i = \beta_{i,eff}/\beta_{eff}$, the relative delayed neutron fraction ($\sum_{i=1}^6 b_i = 1$)

One might wonder whether one can use the point reactor model to describe the physical behaviour of HTR-PROTEUS. Keijzer [33] argued that if the physical size of the system is small compared to the root mean square length of the prompt neutron chain, the different parts of a system are tightly coupled and therefore changes in the spatial dependence of the neutron flux (which is the product of the neutron density and the neutron velocity) are not to be expected, i.e. the point reactor model can be used. For a homogeneous system this condition can be written as:

$$\frac{S}{\sqrt{\langle l^2 \rangle}} = \frac{S}{\sqrt{\frac{6M^2}{\beta_{eff} - \rho}}} = \frac{S}{\sqrt{\frac{6M^2}{\beta_{eff}}}} \sqrt{1-r} < 1 \quad (2.3)$$

where S is the characteristic physical size of the reactor, $\langle l^2 \rangle$ is the mean square length of the prompt neutron chain, and M^2 is the migration area. In fact, Eq. (2.3) is frequency dependent. In the presented form, it only holds for frequencies below the prompt decay constant, which means in HTR-PROTEUS frequencies below ~ 1 Hz (see chapter 3). Typical values for HTR-PROTEUS are $S=125$ cm (the core diameter) and $\beta=0.0072$. The value of M^2 varies between 1250 cm^2 (for core 5, the worst moderated core) and 575 cm^2 (for core 7, the best moderated core). With these values, condition (2.3) is satisfied for reactivities larger than $-66 \text{ \$}$ and $-30 \text{ \$}$ in core 5 and 7, respectively, and hence in all practical circumstances the point reactor model can be applied for the analysis of low-frequency reactivity disturbances (for instance the reactivity worth of small material samples which will be discussed in chapter 5).

Returning again to the kinetic equations, the solution $n(t)$ is often required for two cases:

1. for a given $r(t)$ and a constant external source Q
2. for a given $Q(t)$ and constant r

The first problem involves solving a non-linear equation. For small changes $\delta r(t)$ and $\delta n(t)$ from the stationary values r_0 and n_0 , the kinetic equations can be linearised. It turns out that these linearised equations are equal to the kinetic equations themselves, except that $r(t)$ is replaced by r_0 and the source $Q(t)$ is given by $n_0 \delta r(t) / \Lambda^*$. Hence, except for an amplitude factor, both cases have the same solution. This solution can be found by Laplace transforming the (linearised) kinetic equations, yielding $\bar{n}(s) = n_0 G(s) \bar{\rho}(s)$ for small reactivity changes and $\bar{n}(s) = \Lambda G(s) \bar{Q}(s)$ for changes in the external neutron source. Here, $G(s)$ is the zero-power reactor transfer function which is given by

$$G(s) = \frac{1}{\Lambda s + \sum_{i=1}^6 \frac{\beta_i s}{s + \lambda_i} - \rho_0} \quad (2.4)$$

where the subscript 'eff' has been dropped for convenience. This function has six zeros $s = -\lambda_i$ and seven poles which can be found by setting the denominator of Eq. (2.4) to zero:

$$\Lambda s + \sum_{i=1}^6 \frac{\beta_i s}{s + \lambda_i} - \rho_0 = 0 \quad (2.5)$$

Equation (2.5) is the famous 'inhour equation' which relates the reactivity to the decay constants of both prompt and delayed neutrons. In figure 2.1 the reactivity is plotted versus the variable s where use was made of parameter values representative for HTR-PROTEUS. The solutions of Eq. (2.5) are the intersections of this curve with a horizontal line, which values have to be calculated numerically. In this work, the prompt decay - the most negative root of Eq. (2.5) - was determined via a Newton-Raphson search procedure, the subsequent five roots via Regula-Falsi (bisection) where the decay constants of the precursors are taken as boundaries. The procedure to compute the largest root depends on the reactivity:

1. $\rho_0 < 0$: Regula-Falsi with $-\lambda_1$ and zero as left and right boundary, respectively
2. $\rho_0 = 0$: trivial, root is also zero
3. $\rho_0 > 0$: Newton-Raphson search

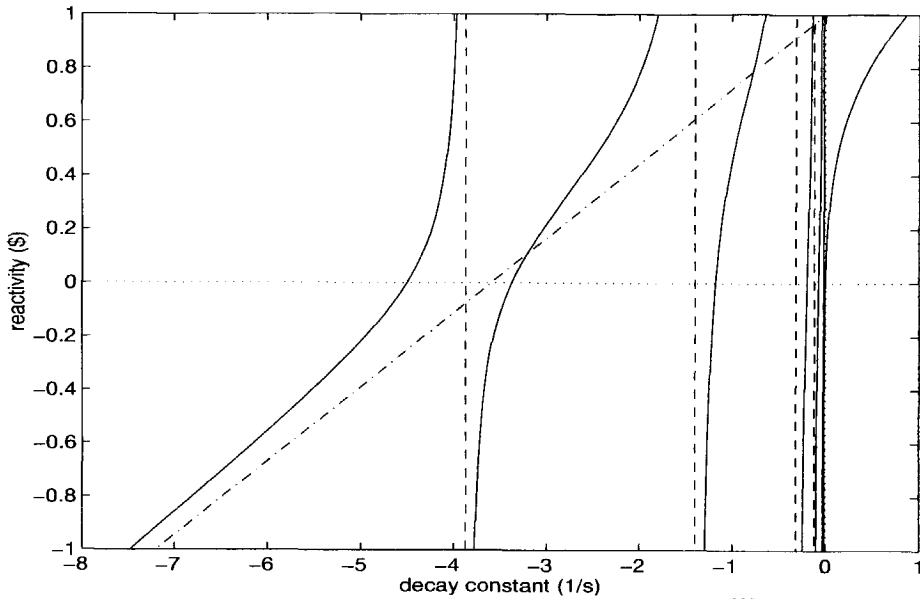


Figure 2.1 Visualisation of the inhour equation. Delayed neutron data of ^{235}U was taken from the JEF-1.1 library. The generation time was assumed to be 2 ms and β_{eff} was set to 0.0072. The dashed lines indicate the decay constants of the delayed neutron precursors. The dash-dotted line represents the asymptote $\rho = 1 + \Lambda^*$.

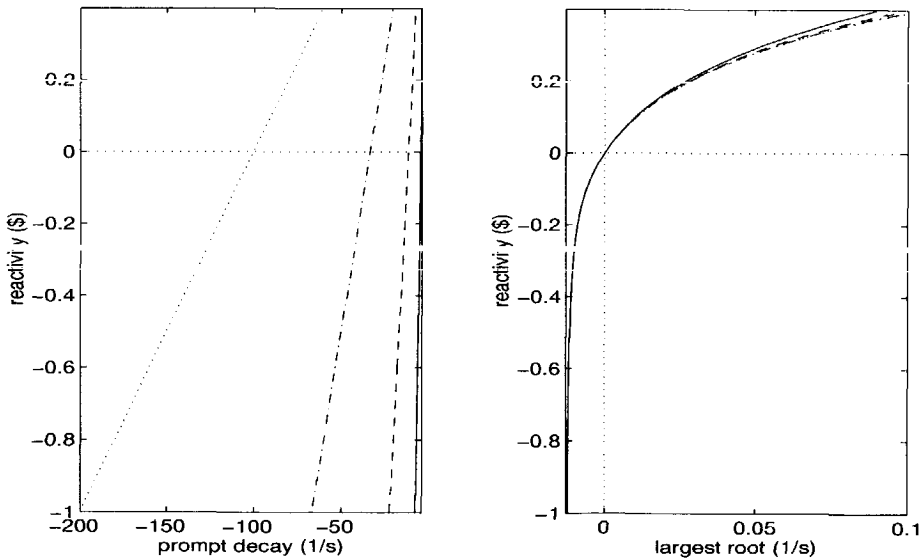


Figure 2.2 The effect of the value of the reduced generation time on the smallest (i.e. the prompt decay constant) and the largest root of the inhour equation. Indicated are the roots corresponding to $\Lambda^* = 0.2778$ s (solid line, HTR-PROTEUS), $\Lambda^* = 0.09$ s (dashed line), $\Lambda^* = 0.03$ s (dash-dotted line), and to $\Lambda^* = 0.01$ s (dotted line, a typical LWR).

The thus computed roots were checked by substituting them back into the inhour equation. If $|s| \gg \lambda_i$, the inhour equation can be simplified to $r = 1 + \Lambda^* s$. Indeed, in an LWR (with a reduced generation time of typically 0.01 s) the prompt decay constant s_0 is an order of magnitude larger than the decay constants of the precursor groups and hence, to a very good degree $s_0 = (r-1)/\Lambda^*$. This approximation is very often encountered in the literature, but as figure 2.1 clearly shows, this approximation does not hold in HTR-PROTEUS because s_0 is of the same order of magnitude as the precursor decay constants. This is due to the long generation time of HTR-PROTEUS (1.5 to 2 ms). Figure 2.2 shows how the magnitude of the prompt decay constant s_0 strongly increases with decreasing generation time. In contrast to this root, the largest root of the inhour equation is in practical situations, where the reactivity is limited to about 0.25 \$, not sensitive to the value of the generation time, as is also illustrated by figure 2.2.

The contribution of the prompt neutron decay is dominant in the PNS and noise techniques, which are therefore sensitive to the value of the (reduced) generation time. Both the experimental determination and the calculation of this parameter are outlined in chapter 3. The IK technique on the other hand, computes the reactivity corresponding to transients recorded on longer time scales than PNS and noise techniques, and such slower transients are dominated by the largest root(s) of the inhour equation which was seen to be very insensitive to the value of the generation time (but sensitive to the delayed neutron parameters).

Quite often, it is convenient to express the transfer function $G(s)$ in terms of its zeros and poles or in terms of its residues and poles:

$$G(s) = \frac{\prod_{i=1}^6 (s + \lambda_i)}{\Lambda \prod_{p=0}^6 (s + s_p)} = \sum_{p=0}^6 \frac{A_p}{s + s_p} \quad (2.6)$$

where the poles are denoted as $-s_p$ and the residues A_p are equal to

$$A_p = \lim_{s \rightarrow -s_p} (s + s_p) G(s) = \frac{1}{\Lambda + \sum_{i=1}^6 \frac{\beta_i \lambda_i}{(\lambda_i - s_p)^2}} \quad (2.7)$$

Again, it is worthwhile to point out the difference between an LWR and an HTR. In an LWR, $s_0 \gg \lambda_i$ and hence $A_0 \rightarrow \Lambda^{-1}$. Therefore, A_0 is of the order of 10^4 s^{-1} , whereas the remaining residues are of the order of 10 s^{-1} , as can be seen by substituting typical LWR parameter values in Eq. (2.7). In a critical HTR-PROTEUS configuration on the other hand, A_0 is about 250 s^{-1} , A_1 about 185 s^{-1} , A_2 about 34 s^{-1} , and the other residues about 10 s^{-1} or smaller. These results, in combination with the roots of the inhour equation, indicate that in contrast to a typical LWR, in HTR-PROTEUS it is difficult to separate the prompt and delayed neutron contributions to transients.

Now $G(s)$ is known, it is possible to compute the response of the neutron population to a given source function or reactivity change. If, for example, $Q(t) = \delta(t)$, the neutron response is

simply the inverse Laplace transform of the zero-power reactor transfer function (Eq. 2.6) times the generation time:

$$n(t) = \Lambda \sum_{p=0}^6 A_p e^{-\lambda_p t} \quad (2.8)$$

This equation can be used to check the computed residues: Since $n(0) = 1$, the sum of all residues should be equal to the reciprocal generation time. We will encounter Eq. (2.8) again in subsequent sections.

2.2 Inverse kinetics technique

To obtain an expression for the reactivity $r(t)$ in terms of the neutron population $n(t)$, first equation (2.2) is integrated which results in the following expression for the delayed neutron precursors:

$$C_i(t) = \frac{b_i}{\Lambda^*} \int_{-\infty}^t e^{-\lambda_i(t-\tau)} n(\tau) d\tau \quad (2.9)$$

where use was made of the reduced parameters. Substituting this result in Eq. (2.1), and re-arranging yields:

$$r(t) = 1 - \frac{1}{n(t)} \sum_{i=1}^6 b_i \lambda_i \int_{-\infty}^t e^{-\lambda_i(t-\tau)} n(\tau) d\tau + \frac{\Lambda^*}{n(t)} \frac{dn}{dt} - \frac{\Lambda^* Q}{n(t)} \quad (2.10)$$

Note that in the expression above, $n(t)$ can be replaced by any quantity proportional to $n(t)$ as long as the source term $c\Lambda^*Q$, which has the same dimension as $cn(t)$, where c is the proportionality constant, is known. However, under many practical circumstances the source term can be ignored. Furthermore, the third term in the right hand side of Eq. (2.10) is small with the consequence that the dependence of the IK technique on the generation time is only weak. The integral in Eq. (2.10) can be calculated recursively from a sampled version of $n(t)$, using linear interpolation between two consecutive samples $n_{k-1}=n(t_{k-1})$ and $n_k=n(t_k)$ at a time interval Δt apart [3]:

$$I_{i,k} = \int_{-\infty}^t e^{-\lambda_i(t_k-\tau)} n(\tau) d\tau = e^{-\lambda_i \Delta t} I_{i,k-1} + \frac{n_k}{\lambda_i} \left(1 - \frac{1 - e^{-\lambda_i \Delta t}}{\lambda_i \Delta t} \right) - \frac{n_{k-1}}{\lambda_i} \left(e^{-\lambda_i \Delta t} - \frac{1 - e^{-\lambda_i \Delta t}}{\lambda_i \Delta t} \right) \quad (2.11)$$

Assuming that the system was in a stationary state before and at the start of the measurement, it can be shown easily that $I_{i,0}=n_0/\lambda_i$. This method to solve the integral is also recommended by Báez et al. [10], as it was seen to yield the most precise results of the seven different methods which they have investigated.

2.2.1 Correction factors

One has to realise that the standard IK technique, as described above, is based on the point reactor model, i.e. it is assumed that the source of the reactivity change, e.g. inserting an absorber rod, does neither change the spatial flux distribution nor the energy distribution. However, especially in case of strong reactivity disturbances, these local effects can have a

significant effect on the experiments. Difilippo [4,5] (see also [6,9]) described a method which involves the use of calculated correction factors to convert the measured response of a detector at position r_{det} to the global change in neutron density $n(t)$ appearing in Eq. (2.10). The detector response $q_{\text{det}}(r_{\text{det}}, t)$ can be written as

$$q_{\text{det}}(r_{\text{det}}, t) = \iint \Sigma_{\text{det}}(r, E) \phi(r, E, t) dV dE \quad (2.12)$$

where Σ_{det} is the macroscopic cross section of the detector and the integrations are performed over the entire energy range and over the detector volume. Now, the flux can be factorised into a purely time-dependent amplitude function, $n(t)$, and a space-, energy-, and time-dependent shape function, $\psi(r, E, t)$ [34]:

$$\phi(r, E, t) = \psi(r, E, t)n(t) \quad (2.13)$$

The employment of the factorisation is particularly advantageous if the flux variation with time consists primarily of flux amplitude changes with comparatively small time variations of the shape function. For example, in case of dropping a shutdown rod, the shape function ψ is time dependent during the rod drop, but ψ is static before and after the drop (ignoring harmonic effects). The amplitude function $n(t)$ represents the global time dependence of the neutron population due to the decay of the prompt and delayed neutron populations after the rod drop. To make the factorisation unique, a second equation is required. This second equation can be used to shift the major time dependence into the amplitude function by constraining the time variation of the magnitude of the shape function. Usually the following constraint is chosen:

$$\iint \phi_0^+(r, E) \frac{1}{v(E)} \psi(r, E, t) dV dE = K_0 \quad (2.14)$$

where K_0 is a constant, v the neutron velocity, and ϕ_0^+ is the adjoint function in a reference state. Equation (2.14) implies that the shape function ψ must be defined as follows:

$$\psi(r, E, t) = \frac{K_0 \psi_{\text{arb}}(r, E, t)}{\iint \phi_0^+(r, E) \frac{1}{v(E)} \psi_{\text{arb}}(r, E, t) dV dE} = \frac{K_0}{K_{\text{arb}}} \psi_{\text{arb}}(r, E, t) \quad (2.15)$$

where ψ_{arb} represents an arbitrarily normalised shape function and K_{arb} a corresponding constant. Substituting Eq. (2.13) and (2.15) into Eq. (2.12) yields

$$q_{\text{det}}(r_{\text{det}}, t) = n(t) \frac{K_0}{K_{\text{arb}}} \iint \Sigma_{\text{det}}(r, E) \psi_{\text{arb}}(r, E, t) dV dE \quad (2.16)$$

Defining the relative changes $Q_{\text{det}}(r_{\text{det}}, t) = \frac{q_{\text{det}}(r_{\text{det}}, t)}{q_{\text{det}}(r_{\text{det}}, 0)}$ and $N(t) = \frac{n(t)}{n(0)}$, and using Eq. (2.16), the relation between $N(t)$ and $Q_{\text{det}}(r, t)$ can be written as

$$N(t) = Q_{\text{det}}(r_{\text{det}}, t) A(r_{\text{det}}, t) B(t) \quad (2.17)$$

where

$$A(r_{\text{det}}, t) = \frac{\iint \Sigma_{\text{det}}(r, E) \psi_{\text{arb}}(r, E, 0) dV dE}{\iint \Sigma_{\text{det}}(r, E) \psi_{\text{arb}}(r, E, t) dV dE} \quad (2.18)$$

and

$$B(t) = \frac{K_{\text{arb}}(t)}{K_{\text{arb}}(0)} \quad (2.19)$$

The first correction term $A(r_{\text{det}}, t)$ depends on the position r_{det} of the detector and accounts for the shadowing effect of a control rod. Examples of the correction surface in HTR-PROTEUS can be found in chapter 6 and in Ref. 6. The notation $K_{\text{arb}}(t)$ in Eq. (2.19) is somewhat misleading since K_{arb} is a constant and thus independent of time. Hence, one would expect $B(t)$ to be equal to unity for all t . However, in this thesis the shape function is calculated twice: before and after a rod drop. These are two independent calculations and since the calculated shape functions are normalised to an user specified fission rate (i.e. reactor power), usually two different values for K_{arb} are obtained. Consequently, $B(t)$ equals unity before the rod drop, but after the rod drop $B(t)$ equals $B_1 = K_{\text{arb}}(\text{after rod drop}) / K_{\text{arb}}(\text{before rod drop})$. If use is made of the definition of the generation time (see section 3.2.3),

$$\Lambda(t) = \frac{\iint \phi_0^+(r, E) \frac{1}{v(E)} \psi_{\text{arb}}(r, E, t) dV dE}{\iiint \phi_0^+(r, E) \chi(E) v \Sigma_f(E') \psi_{\text{arb}}(r, E', t) dV dE dE'} = \frac{K_{\text{arb}}(t)}{F_{\text{arb}}(t)} \quad (2.20)$$

where $F_{\text{arb}}(t)$ is an arbitrarily normalised weighted neutron production, the correction factor $B(t)$ can also be written as

$$B(t) = \frac{\Lambda(t) F_{\text{arb}}(t)}{\Lambda(0) F_{\text{arb}}(0)} \quad (2.21)$$

This expression for $B(t)$ is used in this work since both Λ and F_{arb} are calculated by a code applied at IRI. If the weighted neutron production F_{arb} is kept constant, i.e. $F(t) = F(0)$, $B(t)$ reduces to the ratio of the generation times in the rodged and unrodged configurations. It has been found to vary roughly linearly with the reactivity $\bar{\rho}$.

In summary, to apply the inverse kinetics technique, first the measured response $Q_{\text{det}}(r_{\text{det}}, t)$ is converted to the global change in neutron population $N(t)$ according to Eq. (2.17), using the calculated correction factors $A(r_{\text{det}}, t)$ and $B(t)$. Subsequently, $N(t)$ can be substituted in the inverse kinetics equation (2.10) to obtain the correct reactivity. If only the integral worth of a control rod is of interest, then the shape function ψ has to be calculated only before and after the rod drop. Consequently, both $A(r_{\text{det}}, t)$ and $B(t)$ equal unity before the rod drop, and equal $A_1(r_{\text{det}})$ and B_1 after the rod drop. During the drop, $A(r_{\text{det}}, t)B(t)$ can be assumed to change linearly from unity to $A_1(r_{\text{det}})B_1$.

2.2.2 Special case of inverse kinetics: the stable period technique

In case the reactivity remains constant after t_1 , the point kinetic equations are linear for $t > t_1$. Thus, the equations can be directly Laplace-transformed, and a solution can be found for $t > t_1$.

which can be written in the form of Eq. (2.8):

$$N(t) = \sum_{p=0}^6 R_p e^{-s_p(t-t_1)} \quad t > t_1 \quad (2.22)$$

The residues R_p depend on the time history of the reactivity before t_1 and are in general unknown. For a positive reactivity, only the last root $-s_6$ of the inhour equation is positive (i.e. s_6 is negative), see also figures 2.1 and 2.2. As a result, the first 6 terms of Eq. (2.22) die out leaving the asymptotic solution

$$N_{\text{asym}}(t) = R_6 e^{-s_6(t-t_1)} \quad t > t_1 \quad (2.23)$$

Hence, $-s_6$ is the root that ultimately determines the positive period of the system. Therefore, by fitting an exponential curve to the measured transient (omitting the beginning of the transient from the fit interval), a value of $-s_6$ is obtained which can be substituted into the inhour equation (2.5) to obtain the reactivity.

2.2.3 Experimental details

For the measurements, use was made of uncompensated ionisation chambers of type 'RC7' originally developed by A.E.R.E., Harwell. These chambers employ the ^{10}B (n, α) ^7Li reaction for the detection of neutrons, the ^{10}B being incorporated in a thin film of 90% enriched boron coated on to the electrodes. The currents from these detectors were amplified and filtered by electronic instrumentation identical to the electronics of the linear channel of the nuclear instrumentation of HTR-PROTEUS. The measured frequency response of this instrumentation can be approximated well by a second-order low-pass filter with a bandwidth of about 0.24 Hz, see figure 2.3.

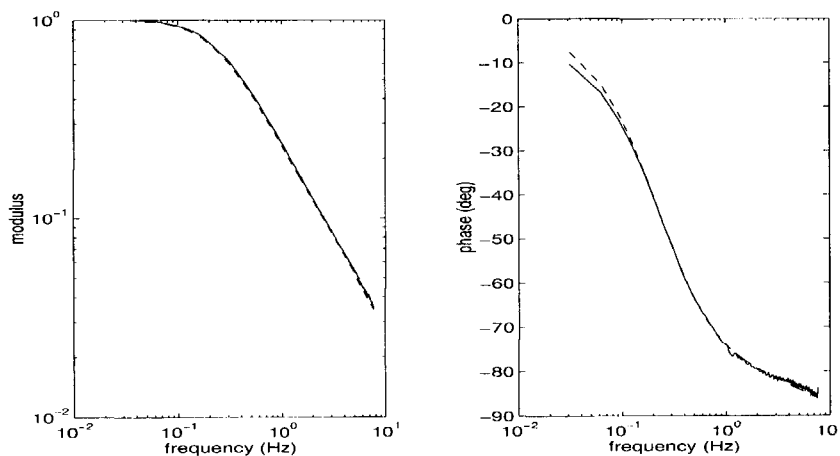


Figure 2.3 The measured frequency response of the linear channel electronics (solid line). The dashed line indicates the second-order low-pass filter approximation. The two poles and the zero of this filter were determined to be -15.88 s^{-1} , -1.45 s^{-1} , and -13.71 s^{-1} , respectively.

The advantage of such a frequency response is that the signal noise is suppressed. The disadvantage is that signal changes are retarded as illustrated in figure 2.4. This effect has to be considered if the reactivity as a function of time is of importance. On the other hand, it is not important when for example the integral reactivity worth of a control rod has to be measured as in this case, only the difference has to be known between the reactivity states before and a sufficient waiting time (depending on the slowness of the amplifier) after the rod movement. Later, more modern current amplifiers developed at IRI became available with a much larger bandwidth (> 8 Hz). The signal noise at the normal PROTEUS operating fluxes of 10^6 - 10^8 n.cm⁻².s⁻¹ turned out not to be significant.

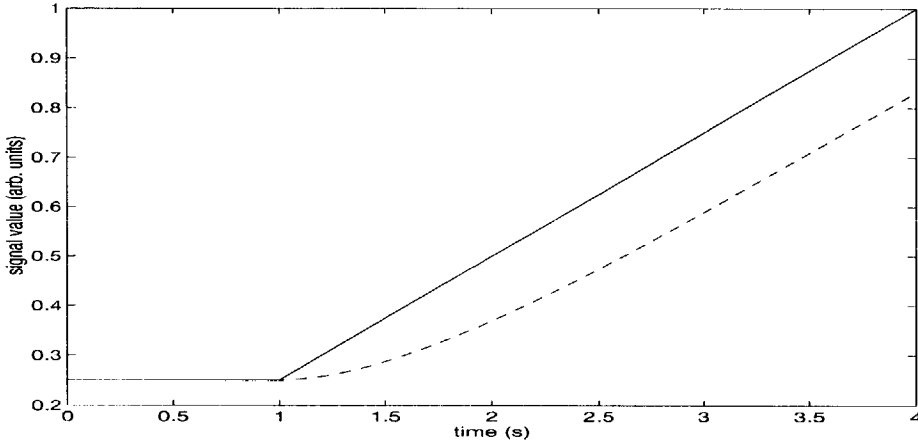


Figure 2.4. The response of the linear channel electronics to a ramp. The solid line indicates the input signal and the dashed line the output signal which is seen to be delayed by 0.682 s.

The amplified detector signal is sampled with the PC-based measurement system DSA-2 [35], developed at the department of nuclear energy of the energy research foundation ECN, Petten, The Netherlands. This system can sample two signals with a maximum of 4 Hz. For both signals, the reactivity is calculated on-line according to Eqs. (2.10) and (2.11). The maximum sampling frequency of 4 Hz poses problems in the estimation of the derivative if the signal changes fast relative to this frequency, for example in rod drop experiments. The procedure used to estimate the derivative is a least squares fit of a second-order polynomial to $2M+1$ consecutive points, centred on the point of interest. The derivative in the central point is then given by:

$$\left. \frac{dn}{dt} \right|_{t=t_k} = \frac{\sum_{k=-M}^M k n_k}{2\Delta t \sum_{k=1}^M k^2} \quad (2.24)$$

In the DSA-2 system, M is set to 3. In case the sampling frequency is too low and the DSA-2 derivative estimator fails, the reactivity was recalculated off-line using a simple first-order estimate:

$$\left. \frac{dn}{dt} \right|_{t=t_k} = \frac{n_{k+1} - n_k}{\Delta t} \quad (2.25)$$

The disadvantage of this estimator is the higher sensitivity to signal noise. Since the problem of the derivative estimation arises because of the too low maximum sampling frequency, another data-acquisition program was developed which allowed higher sampling frequencies (up to 100 Hz) and the use of eight input channels instead of only two. The reactivity then has to be calculated off-line. However, when the correction factors described in section 2.2.1 have to be applied, this has to be done anyway.

2.3 Pulsed Neutron Source technique

The determination of the subcriticality via the analysis of the response of a system to a pulsed neutron source was suggested in the 1950s by Sjöstrand [11] and by Simmons and King [14]. Although several modifications to these basic techniques have been suggested, the current analysis methods fall into one of two categories associated with the previously mentioned authors. These categories are the area-ratio methods, the concept of which is attributed to Sjöstrand, and the inhour methods associated with Simmons and King.

2.3.1 Area-ratio methods

In section 2.1 the response of a point reactor to a unit pulse of neutrons at $t=0$ was calculated to be (viz. Eq. (2.8):

$$n(t) = \Lambda \sum_{p=0}^6 A_p e^{-s_p t} \quad (2.26)$$

The prompt and delayed neutron areas are:

$$A_p = \int_0^{\infty} n_p(t) dt = \int_0^{\infty} \Lambda A_0 e^{-s_0 t} dt = \Lambda \frac{A_0}{s_0} \quad (2.27)$$

$$A_d = \int_0^{\infty} n_d(t) dt = \int_0^{\infty} \Lambda \sum_{j=1}^6 A_j e^{-s_j t} dt = \Lambda \sum_{j=1}^6 \frac{A_j}{s_j} \quad (2.28)$$

Figure 2.5 illustrates the response of a subcritical system to a pulse of neutrons, and shows the decay of the prompt and delayed neutron populations. The prompt and delayed areas are simply the areas below the dash-dotted and dotted lines, respectively.

It can be shown [19] that the reactivity is related to the prompt-to-delayed area ratio as

$$r = -\frac{A_p}{A_d} \sum_{i=1}^6 \frac{b_i}{\left(1 - \frac{\lambda_i}{s_0}\right)^2} \quad (2.29)$$

Only in systems with a very short generation time in which s_0 is very large compared to the decay constants of the delayed neutrons (see section 2.1), the reactivity becomes equal to the ratio of the prompt to delayed area.

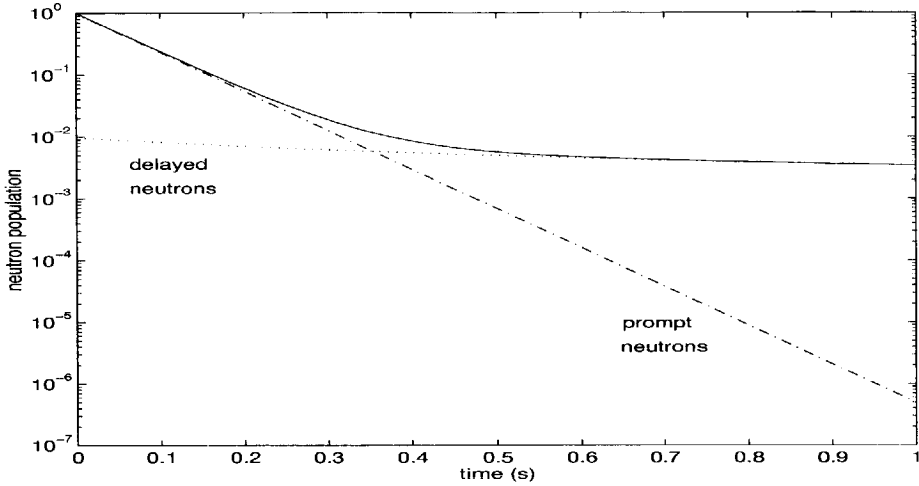


Figure 2.5 A typical pulse response of a subcritical system. The reactivity was assumed to be -3% . The other reactor parameters were the same as used for figure 2.1. Shown are the decay of the total (solid), prompt (dash-dotted) and delayed (dotted) neutron population.

The problem with this Sjöstrand method is the determination of the prompt area. Short-lived flux modes are generated which can be significant on a time scale of milli-seconds, distorting the response shown in figure 2.5. To overcome the difficulty associated with these prompt harmonics, Gozani [12] proposed to extrapolate a fit to the linear part (on a logarithmic scale) of the prompt decay curve back to $t=0$. In this way, a prompt area can be obtained which is free from harmonic distortion.

A second problem associated with the area-ratio methods is the kinetic distortion [9]. Very generally, it means that the pulse response in a strongly absorbing region (e.g. the core) of the system tends to have a higher relative delayed background than in a weakly absorbing region (e.g. the reflector). This effect makes the area-ratio methods space dependent. Difilippo [18] showed that the true reactivity can be obtained from the Gozani reactivity via two calculated correction factors:

$$r_{true} = r_{Gozani} K_d H_d \quad (2.30)$$

The factor K_d corrects for the kinetic distortion and H_d represents the effects of delayed harmonics, which in general, are smaller than the effects of prompt harmonics. The expressions for K_d and H_d can be found in Ref. 18 and 9. The total correction factor is significant at most detector positions, but eventually yield results that are consistent with other measurement techniques, indicating that no significant systematic errors are being introduced via the calculated parameters [22]. However, in order to reduce the space dependence of the area-ratio method, the use of epithermal neutron detectors is investigated at PSI [23, 24].

2.3.2 Inhour methods

The basis of the inhour methods is to isolate the prompt decay from the delayed background, determine the prompt decay constant α ($= -s_0$) and substitute this into the inhour equation to obtain the reactivity:

$$r = \Lambda^* \alpha + \sum_{i=1}^6 \frac{b_i \alpha}{\alpha + \lambda_i} \quad (2.31)$$

Since α is a global parameter, this method is insensitive to the detector position. However, the conversion of α to r depends on the value of Λ^* , which itself depends on r . To reduce the direct dependence on a calculated value for the generation time, the measured prompt decay constant at critical can be used. At critical, we have

$$0 = \Lambda_c^* \alpha_c + \sum_{i=1}^6 \frac{b_i \alpha_c}{\alpha_c + \lambda_i} \quad (2.32)$$

where the subscript 'c' refers to the critical state. Subtracting (2.32) from (2.31) and rearranging:

$$r = \frac{(\alpha_c - \alpha)}{\alpha_c} f + \epsilon_1 + \epsilon_2 \quad (2.33)$$

with

$$f = \sum_{i=1}^6 \frac{b_i \alpha_c}{\alpha_c + \lambda_i} \quad (2.34)$$

$$\epsilon_1 = \alpha (\Lambda^* - \Lambda_c^*) \quad (2.35)$$

$$\epsilon_2 = \sum_{i=1}^6 \frac{b_i \alpha}{\alpha + \lambda_i} - \sum_{i=1}^6 \frac{b_i \alpha_c}{\alpha_c + \lambda_i} \quad (2.36)$$

Hence, using not only a measured value of the prompt decay in a subcritical state, but also a measured value in the critical state, reduces the dependence upon Λ^* to a dependence upon $\Delta \Lambda^*$, which is expected to be less sensitive to the calculational approach chosen.

2.3.3 Experimental details

The pulsed neutron source itself is a miniature accelerator tube producing pulses of 14 MeV neutrons via the D-T reaction. Its position is indicated in figure 1.4. A pulse unit is used to simultaneously trigger the PNS and the multi-channel scaler. In order to achieve satisfactory statistics, a large number of responses must be superimposed. High-efficient BF_3 detectors were used to measure the responses of the system. These measured responses are processed by the ALPHUBEL code [19,20]. This code applies both the area-ratio and inhour method to determine the reactivity. In this work, only the reactivity from the inhour method is used, thus avoiding the need to calculate the correction factors required by the area-ratio methods. More details about the experimental set-up, the execution of the measurements and the data processing can be found elsewhere [9].

$$D_v = \text{Diven's factor} = \frac{\bar{v}_p(\bar{v}_p - 1)}{\bar{v}^2}$$

where \bar{v}_p = the number of prompt neutrons released per fission and \bar{v} = the average total number of neutrons released per fission. $G(s)$ is the zero-power reactor transfer function which is given by (assuming six delayed neutron groups):

$$G(s) = \frac{1}{\Lambda s + \sum_{i=1}^6 \frac{\beta_i s}{s + \lambda_i} - \rho} = \sum_{p=0}^6 \frac{A_p}{s + s_p} \quad (2.39)$$

where the symbols have their usual meaning. This function has seven roots $-s_p$ ($p=0\dots 6$) and the corresponding residues are equal to

$$A_p = \lim_{s \rightarrow -s_p} (s + s_p) G(s) = \frac{1}{\Lambda + \sum_{i=1}^6 \frac{\beta_i \lambda_i}{(\lambda_i - s_p)^2}} \quad (2.40)$$

The second-order moments can be obtained by integrating $P(t_2 - t_1)$ over the appropriate time intervals. To calculate the moment $\langle n_i(n_i - 1) \rangle$, Yamane and Ito [42] assumed that the dead time d of the detector has a non-paralysable character and therefore, they argued that:

- (1) if the first pulse is detected in the interval $T-d$ to T , the second pulse cannot be detected before time T anymore. Hence, the integral range for t_1 is restricted from 0 to $T-d$
- (2) if the first pulse is detected at time t_1 , the second pulse cannot be detected before time $t_1 + d$. Hence, the integral range for t_2 is restricted from $t_1 + d$ to T .

In formula:

$$\frac{1}{2} \langle n_i(n_i - 1) \rangle = \int_0^{T-d} dt_1 \int_{t_1+d}^T P(t_2 - t_1) dt_2 \quad (2.41)$$

The same arguments can be applied for the calculation of $\langle n_i n_j \rangle$. If $j=i+1$ and the first pulse is detected in the interval $iT-d$ to iT , then the second pulse can only be detected in the interval $t_1 + d$ to $(i+1)T$. Hence,

$$\langle n_i n_{i+1} \rangle = \int_{t_1=(i-1)T}^{iT-d} dt_1 \int_{t_2=iT}^{(i+1)T} P(t_2 - t_1) dt_2 + \int_{t_1=iT-d}^{iT} dt_1 \int_{t_2=t_1+d}^{(i+1)T} P(t_2 - t_1) dt_2 \quad (2.42)$$

Note that if $j > i+1$, the time intervals are not adjacent and the dead time doesn't effect $\langle n_i n_j \rangle$ and thus

$$\langle n_i n_j \rangle = \int_{t_1=(i-1)T}^{iT} dt_1 \int_{t_2=(j-1)T}^{jT} P(t_2 - t_1) dt_2 \quad j > i+1 \quad (2.43)$$

In case two detectors are used, the probability of interest is the probability of detecting the first neutron of a neutron pair in the interval $(t_1, t_1 + dt_1)$ in one detector, and the second neutron in the interval $(t_2, t_2 + dt_2)$ in the other detector. Following the same procedure as Bennet [41], it is straightforward to show that this probability is given by:

$$P_{12}(t_2 - t_1) = R_1 R_2 + F \epsilon_1 \epsilon_2 D_v \sum_{p=0}^6 A_p G(s_p) e^{-s_p(t_2 - t_1)} \quad (2.44)$$

Since the detection of a neutron in one detector does not effect the detection of another neutron in the other detector, the moment $\langle n_{1,i} n_{2,i} \rangle$ can be calculated as

$$\langle n_{1,i} n_{2,i} \rangle = 2 \int_{t_1=0}^T dt_1 \int_{t_2=t_1}^T P_{12}(t_2 - t_1) dt_2 \quad (2.45)$$

The factor 2 in Eq. (2.45) appears as the first neutron can be detected in both detectors. The moment $\langle n_{1,i} n_{2,j} \rangle$ where $j > i$ is given by

$$\langle n_{1,i} n_{2,j} \rangle = \int_{t_1=(i-1)T}^{iT} dt_1 \int_{t_2=(j-1)T}^{jT} P_{12}(t_2 - t_1) dt_2 \quad j > i \quad (2.46)$$

Substituting Eq. (2.38) into Eqs. (2.41), (2.42), (2.43), and Eq. (2.44) into Eq. (2.45) and (2.46), and carrying out the integrations, one obtains:

$$\langle n_i (n_i - 1) \rangle = m^2 \left(1 - \frac{d}{T}\right)^2 + 2\epsilon D_v m \left(1 - \frac{d}{T}\right) \sum_p \frac{A_p G(s_p)}{s_p} e^{-s_p d} F_1(s_p (T - d)) \quad (2.47)$$

$$\langle n_i n_{i+1} \rangle = m^2 \left(1 - \frac{1}{2} \left(\frac{d}{T}\right)^2\right) + 2\epsilon D_v m \sum_p \frac{A_p G(s_p)}{s_p} \left(\frac{1}{2} \frac{d}{T} e^{-s_p d} + \frac{\frac{1}{2} (e^{s_p (T-d)} + e^{-s_p T}) - 1}{s_p T} e^{-s_p T} \right) \quad (2.48)$$

$$\langle n_i n_j \rangle = m^2 + 2\epsilon D_v m \sum_p \frac{A_p G(s_p)}{s_p} \left(\frac{\cosh(s_p T) - 1}{s_p T} e^{-(j-i)s_p T} \right) \quad j > i+1 \quad (2.49)$$

$$\langle n_{1,i} n_{2,i} \rangle = m_1 m_2 + 2 \frac{m_1 m_2}{FT} D_v \sum_p \frac{A_p G(s_p)}{s_p} F_1(s_p T) \quad (2.50)$$

$$\langle n_{1,i} n_{2,j} \rangle = m_1 m_2 + 2 \frac{m_1 m_2}{FT} D_v \sum_p \frac{A_p G(s_p)}{s_p} \left(\frac{\cosh(s_p T) - 1}{s_p T} e^{-(j-i)s_p T} \right) \quad j > i \quad (2.51)$$

where $F_1(x)$ is defined as

$$F_1(x) = 1 - \frac{1 - e^{-x}}{x} \quad (2.52)$$

2.4.3 Feynman- α technique

The experimental quantity that is calculated in the Feynman- α technique is

$$Y = \frac{V}{n} = \frac{\frac{1}{N} \sum_{i=1}^N n_i (n_i - 1) - \left(\frac{1}{N} \sum_{i=1}^N n_i \right)^2}{\frac{1}{N} \sum_{i=1}^N n_i} \quad (2.53)$$

The expectation value of V is:

$$\begin{aligned} \langle V \rangle &= \left\langle \frac{1}{N} \sum_{i=1}^N n_i (n_i - 1) \right\rangle - \left\langle \left(\frac{1}{N} \sum_{i=1}^N n_i \right)^2 \right\rangle \\ &= \langle n_i (n_i - 1) \rangle - \frac{1}{N^2} \left\langle \sum_{i=1}^N n_i^2 + 2 \sum_{i=1}^{N-1} \sum_{k=1}^{N-i} n_i n_{i+k} \right\rangle \\ &= \langle n_i (n_i - 1) \rangle - \frac{1}{N} \left\langle \frac{1}{N} \sum_{i=1}^N n_i (n_i - 1) + \frac{1}{N} \sum_{i=1}^N n_i \right\rangle - \frac{2}{N^2} \left\langle \sum_{i=1}^{N-1} \sum_{k=1}^{N-i} n_i n_{i+k} \right\rangle \\ &= \left(1 - \frac{1}{N} \right) \langle n_i (n_i - 1) \rangle - \frac{1}{N} \langle n_i \rangle - \frac{2}{N} \sum_{k=1}^{N-1} \frac{N-k}{N} \langle n_i n_{i+k} \rangle \end{aligned} \quad (2.54)$$

Substituting Eqs. (2.47), (2.48), and (2.49) into Eq. (2.54), dividing by $\langle n_i \rangle = m$, and some rearranging yields for $\langle Y \rangle$:

$$\begin{aligned} \langle Y(T) \rangle &= 2\varepsilon D_v \sum_p \frac{A_p \zeta(s_p)}{s_p} \left[\frac{N-1}{N} \left(1 - \frac{d}{T} \right) e^{-s_p d} F_1(s_p(T-d)) - \frac{2}{N} \frac{\cosh(s_p T) - 1}{s_p T} \sum_{k=1}^{N-1} \frac{N-k}{N} e^{-s_p k T} + \right. \\ &\quad \left. \frac{N-1}{N^2} \left\{ \frac{e^{s_p T} - e^{s_p(T-d)}}{s_p T} e^{-s_p T} - \frac{d}{T} e^{-s_p d} \right\} \right] \\ &\quad - \frac{1}{N} - 2Rd \frac{N-1}{N} \left(1 - \frac{N+1}{N} \frac{1}{\gamma} \frac{d}{T} \right) \end{aligned} \quad (2.55)$$

In the appendix at the end of this chapter, it is shown that

$$\sum_{k=1}^{N-1} \frac{N-k}{N} e^{-s_p k T} = \frac{e^{-s_p T} (e^{-s_p N T} + N(1 - e^{-s_p T}) - 1)}{N(1 - e^{-s_p T})^2} \quad (2.56)$$

and thus

$$\frac{2}{N} \frac{\cosh(s_p T) - 1}{s_p T} \sum_{k=1}^{N-1} \frac{N-k}{N} e^{-s_p k T} = \frac{1}{N} (F_1(s_p N T) - F_1(s_p T)) \quad (2.57)$$

where $F_1(x)$ is given by Eq. (2.52).

Furthermore, since the dead time d is typically of the order of microseconds and T is of the order of milliseconds, $\exp(-s_p d) \approx 1$ and the ratio d/T can be ignored compared to unity. The approximation of the third term between brackets is proportional to $(d/T)^2$, always resulting in a very small contribution to the total term between brackets, as can be demonstrated by numerical calculations. Therefore, Eq. (2.55) can be simplified to

$$\langle Y(T) \rangle = 2\epsilon D_v \sum_{p=0}^6 \frac{A_p G(s_p)}{s_p} \left\{ F_1(s_p T) - \frac{1}{N} F_1(s_p NT) \right\} - 2Rd \frac{N-1}{N} - \frac{1}{N} \quad (2.58)$$

If the number of intervals (the total measurement time) is infinite, i.e. taking the limit $N \rightarrow \infty$ of Eq. (2.58), the expectation value of $Y(T)$ is seen to become

$$\lim_{N \rightarrow \infty} \langle Y(T) \rangle = 2\epsilon D_v \sum_{p=0}^6 \frac{A_p G(s_p)}{s_p} F_1(s_p T) - 2Rd \quad (2.59)$$

This equation is the generalised form of the equation derived by Yamane and Ito [42], as they did not include the contribution of the delayed neutrons. Except for the term accounting for the dead time effect, it is also the expression normally encountered in the literature (see for example Ref. 30). Because in a critical system the last pole s_6 of the transfer function $G(s)$ is zero, the infinite measurement time model (Eq. 2.59) diverges, independent of the value of the interval width T . However, the finite measurement time model (Eq. 2.58) does not diverge. Using the second order Taylor expansion of $F_1(x)$,

$$\lim_{x \rightarrow 0} F_1(x) \approx \frac{1}{2}x - \frac{1}{6}x^2 \quad (2.60)$$

the term $p=6$, normally causing the divergence, is in Eq. (2.58) seen to become

$$\begin{aligned} \lim_{s_6 \rightarrow 0} \frac{A_6 G(s_6)}{s_6} \left[F_1(s_6 T) - \frac{1}{N} F_1(s_6 NT) \right] = \\ \lim_{s_6 \rightarrow 0} \left\{ \left(\frac{A_6}{s_6} \sum_{j=0}^5 \frac{A_j}{s_j} + \frac{A_6^2}{2s_6^2} \right) \frac{1}{6} (N-1) s_6^2 T^2 \right\} = \frac{1}{12} A_6^2 (N-1) T^2 \end{aligned} \quad (2.61)$$

Equation (2.61) shows that the variance increases linearly with the number of intervals N and thus diverges only if the total measurement time ($=NT$) is infinite. It has to be mentioned that Eq. (2.55) diverges independently of the value of N . The term causing the divergence can be shown to be proportional to the detector dead time d . This is probably due to the approximations involved in the way the detector dead time is taken into account (see also Ref. 43) and is an extra reason for the use of the simplified equation (Eq. 2.58). Recall that the dead time effect in the form of the extra term $-2Rd$ in $\langle Y(T) \rangle$ has been verified by Hashimoto et al. [39].

2.4.4 Bennet's δ -variance technique

In order to avoid the divergence at critical, Bennet [41] suggested to calculate the quantity

$$Y_B = \frac{V_B}{n} = \frac{\frac{1}{2(N-1)} \sum_{i=1}^{N-1} (n_{i+1} - n_i)^2 - \frac{1}{N} \sum_{i=1}^N n_i}{\frac{1}{N} \sum_{i=1}^N n_i} \quad (2.62)$$

The expectation value of V_B is

$$\begin{aligned} \langle V_B \rangle &= \frac{1}{2} \langle (n_{i+1} - n_i)^2 \rangle - \langle n_i \rangle \\ &= \langle n_i^2 \rangle - \langle n_i n_{i+1} \rangle - \langle n_i \rangle \\ &= \langle n_i (n_i - 1) \rangle - \langle n_i n_{i+1} \rangle \end{aligned} \quad (2.63)$$

Substituting Eqs. (2.47) and (2.48) into Eq. (2.63), dividing by $m = \langle n_i \rangle$, rearranging, and simplifying the resulting equation (see section 2.43) yields

$$\langle Y_B(T) \rangle = 2\varepsilon D_v \sum_{p=0}^6 \frac{A_p G(s_p)}{s_p} \left[1 - \frac{\frac{3}{2} + \frac{1}{2} e^{-2s_p T} - 2e^{-s_p T}}{s_p T} \right] - 2Rd \quad (2.64)$$

This result is independent of the number of time intervals and does not diverge at critical as

$$\lim_{s_6 \rightarrow 0} \frac{A_6 G(s_6)}{s_6} \left[1 - \frac{\frac{3}{2} + \frac{1}{2} e^{-2s_6 T} - 2e^{-s_6 T}}{s_6 T} \right] = \frac{1}{6} A_6^2 T^2 \quad (2.65)$$

2.4.5 Covariance technique

In case of a two-detector experiment, one can calculate the covariance instead of the variance, analogous to the more familiar auto- and cross-correlation functions. This idea was originally suggested by Cohn [44]. The quantity of interest is

$$\text{Cov}(T) = \frac{1}{N} \sum_{i=1}^N n_{1,i} n_{2,i} - \left(\frac{1}{N} \sum_{i=1}^N n_{1,i} \right) \left(\frac{1}{N} \sum_{i=1}^N n_{2,i} \right) \quad (2.66)$$

The expectation value of $\text{Cov}(T)$ is

$$\langle \text{Cov}(T) \rangle = \langle n_{1,i} n_{2,i} \rangle - \frac{1}{N} \langle n_{1,i} n_{2,i} \rangle - \frac{2}{N} \sum_{j=1}^{N-1} \frac{N-j}{N} \langle n_{1,i} n_{2,i+j} \rangle \quad (2.67)$$

Substituting Eqs. (2.50) and (2.51) into Eq. (2.67), one obtains after some re-arrangements

$$\langle \text{Cov}(T) \rangle = 2 \frac{m_1 m_2}{FT} D_v \sum_{p=0}^6 \frac{A_p G(s_p)}{s_p} \left[F_1(s_p T) - \frac{1}{N} F_1(s_p NT) \right] \quad (2.68)$$

The terms in the sum in Eq. (2.68) are seen to equal those in the expression for the Feynman- α method and consequently, also Eq. (2.68) does not diverge at critical. Note that the amplitude factor before the sum in Eq. (2.68) reduces to $2\varepsilon_1 D_v$ if $\langle \text{Cov}(T) \rangle$ is divided by m_1 , and vice versa to $2\varepsilon_1 D_v$ if $\langle \text{Cov}(T) \rangle$ is divided by m_2 .

2.4.6 Auto-correlation technique

In the auto-correlation technique, one determines the quantity

$$\Psi(kT) = \frac{\frac{1}{N-k} \sum_{i=1}^{N-k} n_i n_{i+k} - \left(\frac{1}{N} \sum_{i=1}^N n_i \right)^2}{\frac{1}{N} \sum_{i=1}^N n_i} \quad (2.69)$$

The expectation value of the numerator equals for

$$1) \ k=0: \quad \langle n_i^2 \rangle - \frac{1}{N^2} \left\langle \left(\sum_{i=1}^N n_i \right)^2 \right\rangle = \langle n_i (n_i - 1) \rangle - \frac{1}{N^2} \left\langle \left(\sum_{i=1}^N n_i \right)^2 \right\rangle + \langle n_i \rangle \quad (2.70)$$

Accept for the last term $\langle n_i \rangle$, Eq. (2.70) equals Eq. (2.54) and thus

$$\langle \Psi(0) \rangle = \langle Y(T) \rangle + 1 \quad (2.71)$$

$$2) \ k=1: \quad \langle n_i n_{i+1} \rangle - \frac{1}{N^2} \left\langle \left(\sum_{i=1}^N n_i \right)^2 \right\rangle$$

Using Eq. (2.48), the results from section 2.4.3, and then rearranging and simplifying yields

$$\begin{aligned} \langle \Psi(T) \rangle = 2\varepsilon D_v \sum_{p=0}^6 \frac{A_p G(s_p)}{s_p} & \left[\frac{\cosh(s_p T) - 1}{s_p T} e^{-s_p kT} - \frac{1}{N} F_1(s_p NT) \right] + \\ & - \frac{1}{N} + 2Rd \frac{1}{N} \left(1 - \frac{N^2 + 2}{4N} \frac{d}{T} \right) \end{aligned} \quad (2.72)$$

$$3) \ k>1: \quad \langle n_i n_{i+k} \rangle - \frac{1}{N^2} \left\langle \left(\sum_{i=1}^N n_i \right)^2 \right\rangle$$

Using Eq. (2.49), the results from section 2.4.3, and then rearranging and simplifying yields

$$\langle \Psi(kT) \rangle = 2\epsilon D_v \sum_{p=0}^6 \frac{A_p G(s_p)}{s_p} \left[\frac{\cosh(s_p T) - 1}{s_p T} e^{-s_p kT} - \frac{1}{N} F_1(s_p NT) \right] + \left(-\frac{1}{N} + 2Rd \frac{1}{N} \right) \quad (2.73)$$

Equations (2.72) and (2.73) also remain finite in a critical reactor as

$$\lim_{s_6 \rightarrow 0} \frac{A_6 G(s_6)}{s_6} \left[\frac{\cosh(s_6 T) - 1}{s_6 T} e^{-s_6 kT} - \frac{1}{N} F_1(s_6 NT) \right] = \frac{A_6^2}{12} (N - 3k) T^2 \quad (2.74)$$

Again, taking the limit $N \rightarrow \infty$, ignoring the effect of detector dead time and using the approximation

$$\frac{\cosh(s_p T) - 1}{s_p T} = \frac{1}{2} s_p T \quad (2.75)$$

Eqs. (2.72) and (2.73) reduce to the same expression. Also eq. (2.58) reduces to this expression if the dead time is ignored and $F_1(s_p T)$ is approximated by its first-order Taylor expansion. To obtain the auto-correlation function ϕ of the count rate, the expression only has to be divided by T . The result can be written as

$$\langle \phi(kT) \rangle = \frac{\langle \Psi(kT) \rangle}{T} = \delta(kT) + \epsilon D_v \sum_{p=0}^6 A_p G(s_p) e^{-s_p kT} \quad k \geq 0 \quad (2.76)$$

This equation is the pulse counter variant of the expression usually encountered in the literature (see for example Ref. 30), which applies to ionisation chambers. These are most frequently used for correlation measurements, indeed.

2.4.7 Cross-correlation technique

The experimental quantity of the cross-correlation technique is

$$\Psi_{12}(kT) = \frac{1}{N-k} \sum_{i=1}^{N-k} n_{1,i} n_{2,i+k} - \left(\frac{1}{N} \sum_{i=1}^N n_{1,i} \right) \left(\frac{1}{N} \sum_{i=1}^N n_{2,i} \right) \quad (2.77)$$

The expectation value of Eq. (2.77) is

$$\langle \Psi_{12}(kT) \rangle = \langle n_{1,i} n_{2,i+k} \rangle - \frac{1}{N} \langle n_{1,i} n_{2,i} \rangle - \frac{2}{N} \sum_{j=1}^{N-1} \frac{N-j}{N} \langle n_{1,i} n_{2,i+j} \rangle \quad (2.78)$$

where use was made of Eq. (2.54). Substituting Eqs. (2.50) and (2.51), one obtains after some re-arrangements for

$$1) k=0: \quad \langle \Psi_{12}(0) \rangle = 2 \frac{m_1 m_2}{FT} D_v \sum_{p=0}^6 \frac{A_p G(s_p)}{s_p} \left[F_1(s_p T) - \frac{1}{N} F_1(s_p NT) \right] \quad (2.79)$$

$$2) k>0: \quad \langle \Psi_{12}(kT) \rangle = 2 \frac{m_1 m_2}{FT} D_v \sum_{p=0}^6 \frac{A_p G(s_p)}{s_p} \left[\frac{\cosh(s_p T) - 1}{s_p T} e^{-s_p kT} - \frac{1}{N} F_1(s_p NT) \right] \quad (2.80)$$

Equations (2.79) and (2.80) remain finite in a critical system as shown by Eqs. (2.61) and (2.74), respectively. Like in case of the covariance technique, the amplitude factor before the sum in Eqs. (2.79) and (2.80) reduces to $2\varepsilon_2 D_v$ if $\langle \Psi_{12} \rangle$ is divided by m_1 , and vice versa to $2\varepsilon_1 D_v$ if $\langle \Psi_{12} \rangle$ is divided by m_2 .

2.4.8 Effect of the finite measurement time in subcritical systems

Two systems with very different neutronic properties were selected to demonstrate the effect of the finite measurement time. The first system is the Hoger Onderwijs Reactor (HOR) of the Interfaculty Reactor Institute in Delft (The Netherlands), which is a 2 MWth pool-type research reactor. The second system is the HTR-PROTEUS facility at the Paul Scherrer Institute in Villigen (Switzerland), which is a model of a pebble-bed type graphite moderated reactor. Table 2.1 below lists characteristic values of relevant reactor parameters for both systems.

Table 2.1. Relevant reactor parameters

| | HOR | HTR-PROTEUS |
|---|---------------------|---------------------|
| β_{eff} | $7.7 \cdot 10^{-3}$ | $7.2 \cdot 10^{-3}$ |
| Λ (s) | $5.7 \cdot 10^{-5}$ | $2.0 \cdot 10^{-3}$ |
| $\beta_{\text{eff}}/\Lambda$ (s ⁻¹) | 135 | 3.6 |

Note that since the generation time in HTR-PROTEUS is very long, the prompt decay will be of the same order of magnitude as the decay of the fastest group of delayed neutrons. Both systems are assigned the following parameters:

- * JEF-1 delayed neutron data for ^{235}U
- * $D_v = 0.795$, Diven's factor for ^{235}U [45]
- * $\varepsilon = 5 \cdot 10^{-4}$ counts per fission
- * $d = 2 \mu\text{s}$
- * $R = 10^4$ counts per second

We thought it to be illustrative to simulate a Feynman- α measurement, for reasons mentioned in section 2.4.1. It is assumed that for the measurement a multi-channel scaler (MCS) is used to accumulate the counts from the neutron detector. As the number of channels is limited, in practice the measurement is repeated many times to improve the statistical accuracy. In order to avoid repeating measurement with different time intervals, a very short basic time interval Δt (the channel width) is used and successive samples are added to form longer time intervals that are multiples of the basic time interval, hence $T = k\Delta t$, $k=1,2,3,\dots$. The disadvantage of this procedure is that it reduces the number of data points available for longer time intervals, namely $N_k = N/k$.

Before proceeding with the simulation and analysis of the Feynman- α experiment, it is worthwhile to have a look at figures 2.6 and 2.7 which show the effect of the finite measurement time on the variance to mean ratio in the HOR and in HTR-PROTEUS, respectively. Note the difference in the time scale. These figures illustrate that the effect of the finite measurement time correction increases as the number of time intervals decreases, which is in accordance with expectation. The effect itself is an increase in the curvature of $\langle Y(T) \rangle$; the derivative $d\langle Y(T) \rangle/dT$ can even become negative. This effect is seen to be important not only in slightly subcritical systems, but also in deep subcritical systems. Furthermore, the effect is significant in both water and graphite moderated systems.

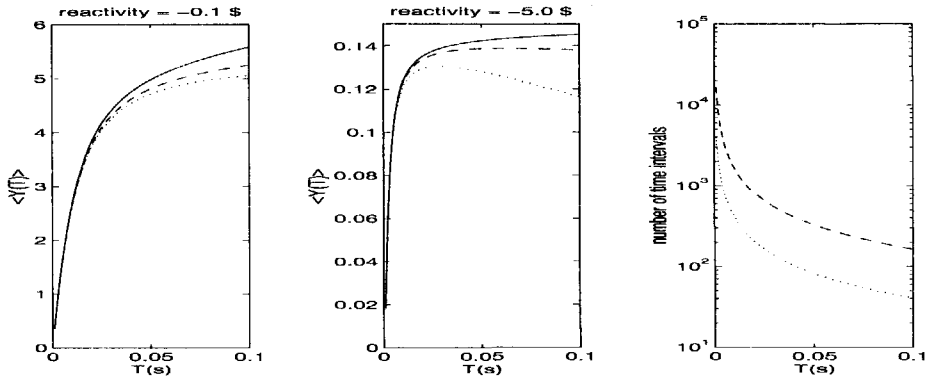


Figure 2.6. Calculated effect of the finite measurement time on $\langle Y \rangle$ in the HOR. A channel width of 1 ms was chosen. The solid line indicates $\langle Y \rangle$ that results for an infinite measurement time ($N_1 \rightarrow \infty$), the dashed line corresponds to $N_1=16384$, and the dotted line to $N_1=4096$. The plot on the right shows the number of time intervals as a function of the length of the time interval.

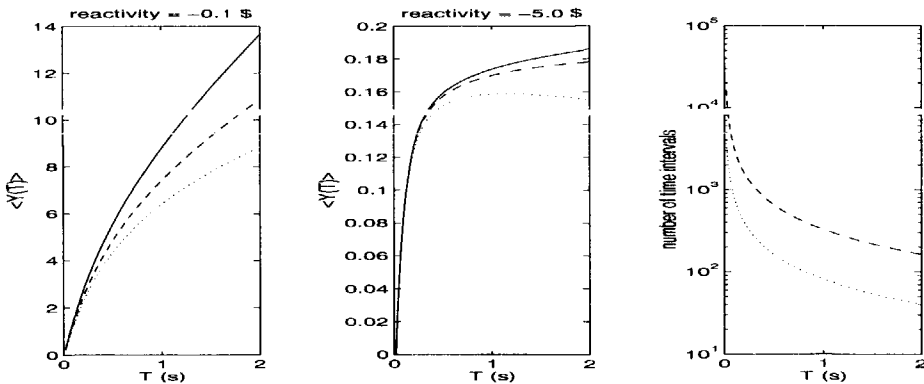


Figure 2.7. Calculated effect of the finite measurement time on $\langle Y \rangle$ in HTR-PROTEUS. A channel width of 20 ms was chosen. The solid line indicates $\langle Y \rangle$ that results for an infinite measurement time ($N_1 \rightarrow \infty$), the dashed line corresponds to $N_1=16384$, and the dotted line to $N_1=4096$. The plot on the right shows the number of time intervals as a function of the length of the time interval.

Having illustrated the effect at two different subcritical states, let us now return to the simulation of the Feynman- α experiment. First, $Y(T)$ is calculated with Eq. (2.58), the model including the finite measurement time effect. For this simulation, the input value of the reactivity was chosen to be -1.0β . As normally a measurement is performed with more than one detector, the number of channels available per detector was supposed to be limited to 4096. The selected channel widths for the HOR and HTR-PROTEUS were 0.5 and 20 ms, respectively. For both systems, the values of $Y(k\Delta t)$ were calculated for values of k in the range from 1 to 100. For the remaining parameters, the previously mentioned values were used. Then, Gaussian white noise of unit variance is generated, multiplied by the estimated standard deviation of $Y(T)$ [28]

$$\sigma_Y = Y \sqrt{\frac{1}{N} \left[\left(4 + \frac{3}{m} \right) \frac{1}{Y} + \left(2 + \frac{3}{m} \right) + \frac{Y}{m} \right]} \quad (2.81)$$

which is then divided by the square root of the number of measurements (assumed to be equal to 100) and finally added to $Y(k\Delta t)$, yielding $Y_{\text{sim}}(k\Delta t)$.

The analysis of this simulated experiment comprises a least squares fit of both Eq. (2.58), and Eq. (2.59) to $Y_{\text{sim}}(k\Delta t)$, using the estimated variance of $Y(k\Delta t)$ as weight. Two parameters were fitted: the reactivity and the detector efficiency. The reactivity does not directly appear in Eqs. (2.58) and (2.59), but with the delayed neutron parameters and the generation time fixed, the reactivity is the only parameter determining the values of the roots of the inhour equation, i.e. the poles of the zero-power reactor transfer function (Eq. 2.39). These in turn, determine the values of the residues (Eq. 2.40).

Figure 2.8 shows Y_{sim} and two examples of fits. Obviously, also with Eq. (2.59), the infinite measurement time model, a good fit to Y_{sim} can be made. This can be explained as follows: The curvature of $\langle Y \rangle$ is increased by the finite measurement time. However, the curvature also increases with subcriticality. Consequently, to a certain extent the increased curvature due to the finite measurement time can be taken into account by overestimating the subcriticality. The reduced amplitude of $\langle Y \rangle$ is then compensated by a larger detector efficiency.

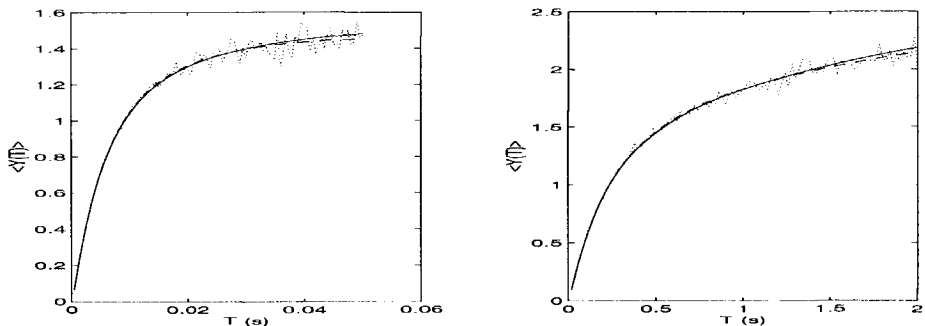


Figure 2.8. The simulated (dotted lines) and fitted variance to mean ratios in the HOR (left) and in HTR-PROTEUS (right). The solid line indicates the fit of Eq. (2.59), the infinite measurement time model, and the dashed line the fit of Eq. (2.58), the finite measurement time model.

As can be seen in figures 2.6 and 2.7, the finite measurement time effect becomes more pronounced as the count time T increases. For this reason, it was expected that the overestimation of the subcriticality and detector efficiency would increase with the length of the fit interval, which was therefore varied. The ratio of the inferred values to the input values of the fit parameters as a function of the length of the fit interval can be found in figures 2.9 and 2.10. The quality of the fits can be assessed by the value of the reduced chi-squared which is shown in figure 2.11, also as a function of the length of the fit interval.

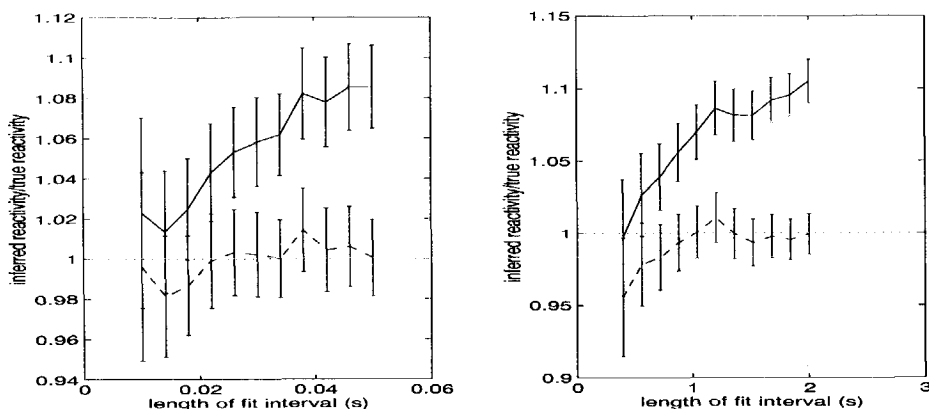


Figure 2.9. The ratio of the inferred value to the input value of the reactivity in the HOR (left) and in HTR-PROTEUS (right). The solid line indicates the result obtained by fitting Eq. (2.59), and the dashed line by fitting Eq. (2.58). The indicated errors are the $\pm 1\sigma$'s returned by the fit program.

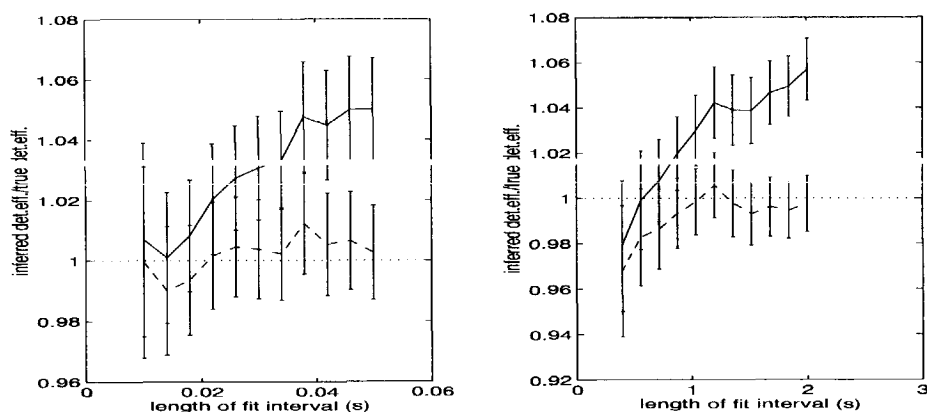


Figure 2.10. The ratio of the inferred value to the input value of the detector efficiency in the HOR (left) and in HTR-PROTEUS (right). The solid line indicates the result obtained by fitting Eq. (2.59), and the dashed line by fitting Eq. (2.58). The indicated errors are the $\pm 1\sigma$'s returned by the fit program.

Figure 2.9 shows that the overestimation of subcriticality and detector efficiency indeed increase with increasing length of the fit interval. For the longest fit intervals applied, the bias in the inferred reactivity value is significant and amounts up to 9% ($\sim 4\sigma$) and 11% ($\sim 7\sigma$) in the HOR and in HTR-PROTEUS, respectively. Nevertheless, the values of the reduced χ^2 (for an excellent fit it is expected to be unity) shown in figure 2.11, do not obviously indicate that the infinite measurement time model does not yield the correct results. Also, note that as the length of the fit interval increases, the statistical accuracy of the fitted parameters increases which is due to the use of more data. The finite measurement time model yields within the statistical uncertainty correct results, which of course only confirms the consistent programming of the applied codes.

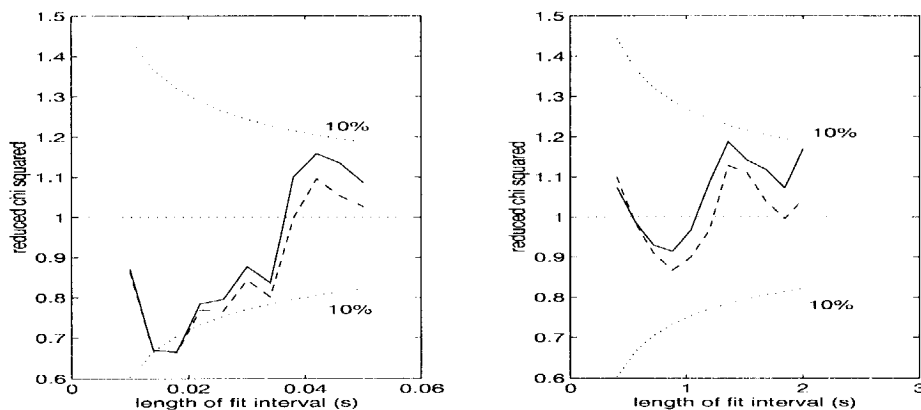


Figure 2.11. The reduced chi-squared of the fits of Eq. (2.59), the solid line, and Eq. (2.58), the dashed line, in the HOR (left) and in HTR-PROTEUS (right). Also shown are the lines corresponding to a probability of 10% of finding a smaller or larger value of the reduced χ^2 .

2.4.9 Experimental details

In the introduction of this chapter, it was mentioned that noise analysis techniques can be applied in a subcritical state directly without reference to a critical state. After the subcritical state has been established, one has to wait ~ 15 minutes to allow the delayed neutron population to stabilise. Very sensitive Russian ^3He neutron counters (type SNM18) were used for the measurements. The counts from the detectors were accumulated in the multi-channel scaler also used for the PNS measurements. Except for the pulse unit and the PNS source, the experimental set-up is therefore identical to that of the PNS measurements.

Very sensitive detectors (i.e. detectors with a high detector efficiency in terms of counts per fission, typically one count per 10^3 fissions) are required since the information concerning the kinetic behaviour of the system originates from the detection of neutrons that belong to the same fission chain. Because of the limited time resolution of these detectors, the count rate has to be kept within an acceptable range which limits the power level at which the measurements can be performed. This can be illustrated by a numerical example. The detector dead time was measured to be 1.3 μs . Limiting the acceptable count-loss effect to 2%, the count rate is limited to about 15000 counts per second. Assuming a detector efficiency of $5 \cdot 10^{-4}$ counts per fission in the system, the maximum acceptable fission rate is $3 \cdot 10^7$ fissions per second, corresponding to about 1 mW. The power range for the application of noise

analysis using pulse detectors is thus limited. However, the advantage of noise analysis is that the same measured data can be analysed with various techniques.

It is difficult to accurately determine the critical rod positions at power levels of 1 mW and lower, because the auto-rod cannot be used at such low power levels (auto-rod servo system was not designed for such low power levels). One would have to determine the insertion depths of the control rods at which the neutron flux remains constant. This is a very time consuming process and not easy because the neutron flux becomes noisier as the power level decreases and furthermore, the effects of external neutron sources, like the start-up source and the spontaneous fissions in ^{238}U , become significant. For this reason noise measurements at critical were performed at power levels of about 1 W. At such power levels the auto-rod can be used to accurately determine the critical state and temperature effects on the reactivity can still be ignored. The disadvantage is that the very sensitive ^3He counters cannot be used because of the detector dead-time. Therefore, for noise measurements at critical use was made of the sensitive ionisation chambers, which were also used for the inverse kinetics measurements. Consequently, counting techniques like the Feynman- α technique cannot be used, and the choice of the analysis methods is limited to the correlation functions and power-spectral-densities.

2.4.10 Conclusions

New formulas for the Feynman- α , covariance, auto- and cross-correlation functions were derived which were shown not to diverge at critical. This was achieved by calculating the expectation values of the experimental quantities, thereby automatically taking into account the finite measurement time. If the measurement time is infinite, the new formulas are seen to reduce to the conventional equations. Furthermore, the new formulas include - in an approximate way - the effect of the detector dead time. Bennet's δ -variance does not suffer from divergence at critical and was seen not to be affected by the finite measurement time.

The finite measurement time also significantly affects the experimental results in subcritical states. By simulating a Feynman- α experiment in a chosen subcritical state, the failure of the conventional expression could be illustrated: the inferred values of the fit parameters (the reactivity and detector efficiency) change when the length of the fit interval is changed. For realistic fit interval lengths, the use of the conventional expression to analyse the experiment was seen to lead to a significant bias in the inferred reactivity value.

REFERENCES

- [1] Sastre C.A., "The Measurement of Reactivity", *Nucl. Sci. & Eng.* **8** 443-447 (1960)
- [2] Scherer W. et al., "Adaptation of the Inverse Kinetic Method to Reactivity Measurements in the Thorium High-Temperature Reactor-300", *Nucl. Sci. & Eng.* **97** 96-103 (1987)
- [3] Hoogenboom J.E. and van der Sluijs A.R., "Neutron Source Strength Determination for on-line Reactivity Measurements", *Ann. Nucl. Energy* **15** 553-559 (1988)
- [4] Difilippo F.C., "LEU-HTR PROTEUS: Theory and Simulations of Reactivity Measurements with the Inverse Kinetics Method", PSI technical memorandum TM-41-91-38, Paul Scherrer Institute, Villigen, Switzerland (1992)
- [5] Difilippo F.C. et al., "Analysis of Kinetics Experiments in LEU-HTR Configurations

- of the PROTEUS Facility", *Trans. Am. Nucl. Soc.* **65** 457-459 (1992)
- [6] Williams T., "Planning and Interpretation of Inverse Kinetics Experiments in LEU-HTR Configurations of the PROTEUS Facility", PSI Annual Report Annexe IV (1992)
- [7] Williams T., "IVK - A FORTRAN Code for use in the Analysis of "Inverse-Kinetics" Measurements (version 1.00)", PSI technical memorandum TM-41-92-10, Paul Scherrer Institute, Villigen, Switzerland (1992)
- [8] Trkov A. et al., "Application of the rod-insertion method for control rod worth measurements in research reactors", *Kerntechnik* **60** 255-261 (1995)
- [9] Williams, T., "Current Status of Methods for Subcriticality Measurements on the PROTEUS Facility", PSI technical memorandum TM-41-95-08, Paul Scherrer Institute, Villigen, Switzerland (1995)
- [10] Báez J.S. et al., "Reactor Reactivity Determination by Inverse Kinetic Approximation", *5th International Conference on Nuclear Engineering (ICONE 5)*, May 26-30, Nice, France (1997)
- [11] Sjöstrand N.G., "Measurements on a Subcritical Reactor using a Pulsed Neutron Source", *Arkiv for Fysik* **11** 233 (1956)
- [12] Gozani T., "A Modified Procedure for the evaluation of Pulsed Source Experiments in Subcritical Reactors", *Nukleonik* **4** 348 (1962)
- [13] Garelis E. and Russell Jr. J.L., "Theory of Pulsed Neutron Source Measurements", *Nucl. Sci. & Eng.* **16** 263 (1963)
- [14] Simmons B.E. and King J.S., "A Pulsed-Neutron Technique for Reactivity Determination", *Nucl. Sci. & Eng.* **3** 595 (1958)
- [15] Preskitt C.A. et al., "Interpretation of Pulsed-Source Experiments in the Peach Bottom HTGR", *Nucl. Sci. & Eng.* **29** 283-295 (1967)
- [16] Pfeiffer W. et al., "Analysis and Results of Pulsed-Neutron Experiments Performed on the Fort St. Vrain High-Temperature Gas-Cooled Reactor", *Nucl. Technology* **27** 352-375 (1975)
- [17] Williams, T., "Preliminary Investigation of Pulsed-Neutron Measurements on HTR PROTEUS", PSI technical memorandum TM-41-90-28, Paul Scherrer Institute, Villigen, Switzerland (1990)
- [18] Difilippo F.C., "LEU-HTR PROTEUS: Neutron Kinetics and Procedures to Analyze Pulsed Neutron Experiments", PSI technical memorandum TM-41-91-27, Paul Scherrer Institute, Villigen, Switzerland (1991)
- [19] Williams, T., "ALPHUBEL - A FORTRAN Code for use in the Analysis of Pulsed-Neutron Source Measurements (version 1.00)", PSI technical memorandum TM-41-91-31, Paul Scherrer Institute, Villigen, Switzerland (1991)
- [20] Williams, T., "Further Validation of the ALPHUBEL Suite (Version 2.00) Using Results from Simulated Experiments", PSI technical memorandum TM-41-91-39, Paul Scherrer Institute, Villigen, Switzerland (1991)
- [21] Difilippo F.C. et al., "Simulation of Pulsed Neutron Source Reactivity Measurements", *Joint Int. Conf. on Mathematical Methods and Supercomputing in Nuclear Applications*, Karlsruhe, Germany (1993)
- [22] Williams T. and Chawla R., "Intercomparison of Rod Worth Measurement Techniques in a LEU HTR Assembly", *Int. Conf. on Reactor Physics and Reactor Computations*, Jan 23-26, Tel Aviv, Israel (1994)
- [23] Rosselet M., "Reactivity Measurement on HTR-PROTEUS Core 5 with the PNS Technique and Preliminary Investigations for the Use of an Epithermal Neutron Detector", PSI technical memorandum TM-41-94-23, Paul Scherrer Institute,

$$\frac{dP(x)}{dx} = \frac{(N-1)x^N - Nx^{N-1} + 1}{(x-1)^2} \quad (\text{A9})$$

and substituting this along with Eq. (A6) into Eq. (A8), we obtain after some re-arrangements

$$\sum_{k=1}^{N-1} \frac{N-k}{N} x^k = \frac{x}{N} \frac{(x^N + N(1-x) - 1)}{(1-x)^2} \quad (\text{A10})$$

Now, simply substituting Eq. (A2) into Eq. (A10) is seen to yield equality (A1).

Chapter 3

The kinetic parameter $\beta_{\text{eff}}/\Lambda$

3.1 Introduction

In chapter 1 it was mentioned that in particular the effects of accidental water ingress on the system criticality and on the reactivity worth of control rods were of importance in the HTR-PROTEUS programme. These reactivity effects were measured with techniques described in chapter 2, which themselves depend on the ratio of the effective fraction of delayed neutrons β_{eff} to the generation time Λ . Since the margin to prompt criticality and the neutron generation time are also important factors in reactor transient analysis, the measurement of the ratio $\beta_{\text{eff}}/\Lambda$ and the validation of the applied procedure to calculate β_{eff} and Λ , are not only important for the analysis of the kinetic experiments in HTR-PROTEUS, but are also useful in a broader context.

This chapter first presents a review of the derivation of the point kinetics equations, with particular emphasis on the definition of the parameters appearing therein. Recommendations are given for the method of calculation of the kinetic parameters to be used in the various reactivity measurement techniques. In the last section, the calculated kinetic parameters for the four selected configurations in a critical state are compared to measured values.

3.2 Theory

Reactor kinetics is represented by a neutron balance equation associated to a set of equations expressing the balance of the delayed neutron precursors. In the operator formulation [1], these equations can be written as:

$$\frac{1}{v} \frac{\partial \Phi}{\partial t} = -M\Phi + (1 - \beta) \chi_p F\Phi + \sum_{i=1}^m \lambda_i \chi_i C_i \quad (3.1)$$

$$\frac{\partial C_i}{\partial t} = \beta_i F\Phi - \lambda_i C_i \quad i = 1 \dots m \quad (3.2)$$

The operator M describes the migration and loss of neutrons. In the diffusion approximation, M is given by:

$$M\Phi = -\nabla \cdot D(r, E, t) \nabla \phi(r, E, t) + \Sigma_t(r, E, t) \phi(r, E, t) - \int_{E'} \Sigma_s(r, E' \rightarrow E, t) \phi(r, E', t) dE' \quad (3.3)$$

The operator F describes the neutron production by fissions

$$F\Phi = \int_{E'} \nu(E') \Sigma_f(r, E', t) \phi(r, E', t) dE' \quad (3.4)$$

The following new symbols were used in the foregoing equations:

- D = the diffusion constant
- Σ_t = the total macroscopic cross section
- Σ_s = the scattering cross section
- Σ_f = the fission cross sections
- ν = the average number of neutrons produced per fission
- χ_p = the fission spectrum of prompt neutrons
- χ_i = the fission spectrum of delayed neutrons of group i

The solution of Eqs. (3.1) and (3.2) is quite involved and in many cases the full solution is not needed. For example in reactor design calculations, the time-independent flux distribution at critical is of particular interest. Therefore it is usual to make simplifying assumptions. A well-known procedure to make the equations independent of time, is the introduction of an eigenvalue. The most common is the 'k-eigenvalue' with which the neutron production term is modified to force criticality. Such calculations provide multiplication factors and flux distributions for static systems. Another method is to assume that the time dependence is exponential which leads to time-independent equations with the ' α -eigenvalue'. Such calculations provide flux decay constants and kinetic flux distributions, which are often required for the interpretation of kinetic experiments. In the two subsequent sub-sections, the background of these two approaches is outlined, followed by the derivation of the point-kinetics equations.

3.2.1 The k-eigenvalue

In the k-eigenvalue approach, the neutron flux and the delayed neutron precursor concentrations are made time-independent, i.e. forced to critical, by dividing the neutron production term $F\Phi$ by a factor k . Setting the left-hand sides of Eqs. (3.1) and (3.2) to zero, and combining the equations yields

$$M\Phi_s = \frac{1}{k} \left[(1 - \beta) \chi_p + \sum_i \beta_i \chi_i \right] F\Phi_s = \frac{1}{k} \chi_{stat} F\Phi_s \quad (3.5)$$

in which Φ_s is the static flux distribution and the term between square brackets the static fission spectrum. Eq. (3.5) is the most common form of the neutron balance equation solved by conventional codes. Because we are here only interested in fundamental mode solutions, k

is the largest eigenvalue of Eq. (3.5) with an associated eigenfunction which is positive everywhere. It can be seen that the eigenvalue k equals the ratio of the neutron production and neutron loss. Hence, the reactivity (see its definition in chapter 1) can subsequently be calculated as

$$\rho = \frac{k-1}{k} \quad (3.6)$$

3.2.2 The α -eigenvalue

In the α -eigenvalue approach, solutions of the form

$$\phi(r, E, t) = \phi_k(r, E)e^{\omega t} \quad (3.7)$$

$$C_i(r, t) = C_{k,i}(r)e^{\omega t} \quad (3.8)$$

are considered. Substituting Eqs. (3.7) and (3.8) into Eqs. (3.1) and (3.2) and combining the results leads to

$$\left(M + \frac{\alpha}{v} \right) \phi_k = \left[(1-\beta)\chi_p + \sum_i \frac{\lambda_i \beta_i \chi_i}{\alpha + \lambda_i} \right] F \phi_k = \chi_{kin} F \phi_k \quad (3.9)$$

Eq. (3.9) has $m+1$ eigenvalues. The largest absolute value of α represents the decay constant of the prompt neutrons and has associated with it the prompt kinetic eigenfunction. This kinetic flux distribution is observed in a system during prompt neutron decay, e.g. shortly after a brief pulse of neutrons is introduced to a subcritical system (PNS measurements) or shortly after a rapid insertion of a control rod into a critical reactor (rod-drop experiments). The delayed kinetic eigenfunctions, associated with the m other eigenvalues, are shown to be very similar to their static counterparts [2], whereas the prompt kinetic eigenfunction was seen to deviate significantly, especially in deeply subcritical systems.

As can be seen from Eq. (3.9) the α -eigenvalue appears as an additional absorption term, and conventional codes make use of this aspect to calculate α by adding enough $1/v$ absorber to bring a system to critical. The term between square brackets is known as the kinetic fission spectrum. Only in prompt critical systems, where $\alpha=0$, the kinetic and static fission spectra are identical.

3.2.3 The derivation of the point-kinetics equations

It was mentioned in chapter 2 that the flux $\phi(r, E, t)$ can be factorized into an amplitude function $n(t)$ and a shape function $\Psi(r, E, t)$. The amplitude function is defined as

$$n(t) = \iint W(r, E) \frac{1}{v(E)} \phi(r, E, t) dV dE \quad (3.10)$$

where for the time being W is an arbitrary weighting function. Note that $n(t)$ is the weighted total number of neutrons present in the system at time t . The factorisation is made unique by the following constraint:

$$\iint W(r, E) \frac{1}{v(E)} \Psi(r, E, t) dV dE = K_0 \quad (3.11)$$

where K_0 is a constant. Multiplying Eq. (3.1) by $W(r, E)$, Eq. (3.2) by $\chi_i(E)W(r, E)/K_0$ and integrating subsequently over space and energy one arrives at the well-known point-kinetics equations:

$$\frac{dn(t)}{dt} = \frac{\rho(t) - \beta_{\text{eff}}(t)}{\Lambda(t)} n(t) + \sum_{i=1}^m \lambda_i c_i(t) \quad (3.12)$$

$$\frac{dc_i(t)}{dt} = \frac{\beta_{\text{eff},i}(t)}{\Lambda(t)} n(t) - \lambda_i c_i(t) \quad i = 1 \dots m \quad (3.13)$$

in which the parameters are defined as follows:

$$\rho(t) = \frac{1}{F(t)} \iint W(r, E) \left\{ \begin{aligned} &\nabla \cdot D(r, E, t) \nabla \Psi(r, E, t) - \Sigma_t(r, E, t) \Psi(r, E, t) \\ &+ \int \Sigma_s(r, E' \rightarrow E, t) \Psi(r, E', t) dE' \\ &+ \chi_{\text{stat}}(E) \int v(E') \Sigma_f(r, E', t) \Psi(r, E', t) dE' \end{aligned} \right\} dV dE \quad (3.14)$$

$$\Lambda(t) = \frac{1}{F(t)} \iint W(r, E) \frac{1}{v(E)} \Psi(r, E, t) dV dE \quad (3.15)$$

$$\beta_{\text{eff},i}(t) = \frac{1}{F(t)} \iint W(r, E) \beta_i \chi_i(E) \int v(E') \Sigma_f(r, E', t) \Psi(r, E', t) dE' dV dE \quad (3.16)$$

$$\beta_{\text{eff}}(t) = \sum_{i=1}^m \beta_{\text{eff},i}(t) \quad (3.17)$$

$$F(t) = \iint W(r, E) \chi_{\text{stat}}(E) \int v(E') \Sigma_f(r, E', t) \Psi(r, E', t) dE' dV dE \quad (3.18)$$

and

$$c_i(t) = \frac{1}{\Lambda(t) F(t)} \iint W(r, E) \chi_i(E) C_i(r, t) dV dE \quad (3.19)$$

It is seen that F represents the weighted, total fission neutron production in the system. As it appears in the denominator of the parameters ρ , β_{eff} , and Λ , the coefficients $(\rho - \beta_{\text{eff}})/\Lambda$ and $\beta_{\text{eff},i}/\Lambda$ in the point-kinetics equations are both independent of the value of F . However, the values of ρ , β_{eff} , and Λ will be affected by the choices of the weighting function and the shape function. The choices of these functions will be addressed in the next section.

3.3 The calculation of the kinetic parameters

Calculated reactivity values are validated by comparing them to measured reactivity values. The conventional codes calculate the multiplication constant k and then the reactivity is obtained as $(k-1)/k$. In an experiment, a characteristic decay constant is measured which is substituted into the inhour equation (Eq. 2.5) to obtain the reactivity. In the inhour equation,

use is made of calculated kinetic parameters. These parameters must be defined in such a way that the resulting reactivity from the inhour equation approximates the static reactivity $(k-1)/k$. In the following sub-section, the choice of the weighting and shape functions in the calculation of the parameters is discussed. In section 3.3.2 an overview is given of the calculational methods used in this work to compute the kinetic parameters.

3.3.1 The choices of the weighting and shape functions

In practice, approximate shape functions are used, e.g. the unperturbed static neutron flux (usually the flux in the critical system). Since the solution of the point kinetics equation is particularly sensitive to an error in the reactivity, a weight function should be chosen that reduces the effect of the shape function inaccuracies on the reactivity. The (unperturbed) adjoint function fulfils this objective [1]. Still, one has to decide to use either the static or the kinetic flux and adjoint function for the calculation of the kinetic parameters. Williams [2] performed a numerical study with the aim to determine the best choices for the weighting and shape functions, which resulted in the following recommendations:

1. Analysis of reactivity measurements depending upon the determination of the prompt decay constant (like the inhour analysis of the PNS measurements) should utilise kinetics parameters calculated using a perturbed, kinetic shape function and a perturbed, static adjoint weighting function.
2. Since the flux distribution during stable period measurements will approximate very closely to a static one, kinetic parameters calculated using an unperturbed, static shape function and an unperturbed, static adjoint weighting function should be utilised in the analysis of these measurements.
3. If the inverse kinetics technique is used to estimate the reactivity, and the reactivity change is small, the recommendation for the stable period technique is applicable. On the other hand, if the reactivity change is large and fast, the recommendation made for the PNS technique is applicable.

Williams did not consider noise measurements. Recall from chapter 2 that these measurements are made in a system in which the flux distribution has stabilised. This suggests the use of the static flux distribution and the static adjoint function in the system of interest as shape and weighting function, respectively. On the other hand, also the noise techniques depend upon the value of the prompt decay constant, e.g. the reactivity determined via the analysis of the power-spectral density mainly depends upon fitting to the high frequency part of the spectrum. This suggests that the same recommendations as made for the PNS technique are applicable. The best choice might be somewhere in between. More research is required to be able to give a more solid recommendation. Without this knowledge available, it was decided - rather arbitrarily - to use the static flux and the static adjoint function.

3.3.2 Calculational methods

Figure 3.1 gives an overview of the data and codes used to calculate the kinetic parameters. The broad-group cross sections generation procedure is described in chapter 4. Although the cross section data is based on the JEF-2.2 data library, the delayed neutron data used in the perturbation theory code PERT-V [3] stems from JEF-1. The reason is that the delayed neutron data in JEF-2.2 has been shown to be inconsistent [4].

The diffusion theory code BOLD VENTURE [5] is used to calculate the neutron flux distribution and the adjoint function (by default a k-eigenvalue calculation is performed which yields the static flux distribution and static adjoint function). Unfortunately, the two-dimensional transport theory code DORT [6] can not be used in conjunction with PERT-V as it does not produce the atomic densities file required by PERT-V.

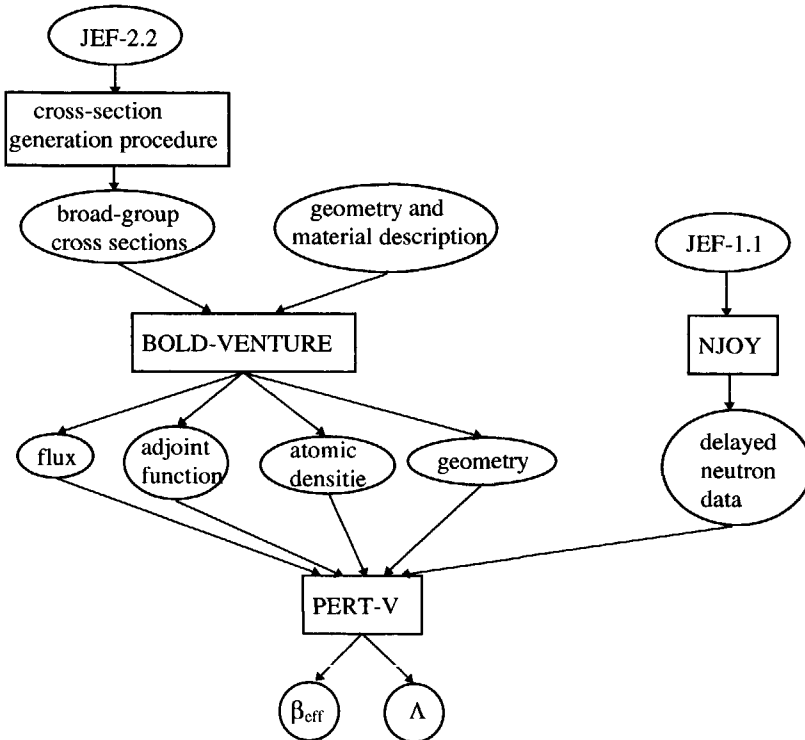


Figure 3.1 Overview of data and codes used for the calculation of the kinetic parameters

If the kinetic flux distribution is required as shape function in the calculation of the kinetic parameters, BOLD-VENTURE is used with the so-called α -search option. In this mode, BOLD-VENTURE does not solve Eq. (3.9), but

$$\left(M + \frac{\alpha}{v}\right) \phi_k = \frac{1}{k} \chi_{stat} F \phi_k \quad (3.20)$$

The only difference with Eq. (3.9) is the use of the static fission spectrum instead of the kinetic one. In order to obtain a correct value for the prompt decay, an extra factor k is introduced which value has to be specified by the user. A starting guess for k is obtained by requiring that Eq. (3.20) approaches Eq. (3.9) as accurate as possible, i.e. the static fission spectrum divided by k should approach the kinetic fission spectrum. If for the starting guess the simplifying assumption is made that the prompt and delayed fission spectra are equal, one obtains for k

$$k = \frac{\chi_{stat}}{\chi_{kin}} \approx \frac{1}{1 - \beta + \sum_i \frac{\lambda_i \beta_i}{\alpha + \lambda_i}} \quad (3.21)$$

In particular in deeply subcritical systems, the amplitude of α is larger than λ_i and thus Eq. (3.21) can be further simplified to

$$k \approx \frac{1}{1 - \left(1 - \frac{\bar{\lambda}}{\alpha}\right)\beta} \approx \frac{1}{1 - \beta} \quad (3.22)$$

where $\bar{\lambda}\beta = \sum_i \lambda_i \beta_i$. Hence, the estimated starting value of k corresponds to a prompt-critical system, which is consistent with the observation made in section 3.2.2 that in a prompt critical system the static and kinetic fission spectrum are identical. A more accurate value for k is subsequently obtained with the following procedure:

1. The eigenvalue k (see Eq. 3.5) and the static adjoint function are calculated with BOLD-VENTURE for the system of interest
2. The static reactivity is calculated: $\rho_{stat} = (k-1)/k$
3. A target value for the factor k in Eq. (3.20) is chosen, with which subsequently the eigenvalue α and the kinetic flux distribution are calculated by BOLD-VENTURE.
4. The parameters β_{eff} and Λ are calculated with PERT-V using the kinetic shape function and the static adjoint weighting function
5. The eigenvalue α and the calculated kinetic parameters are substituted into the inhour equation which yields the reactivity ρ_{inh}
6. If the reactivities ρ_{stat} and ρ_{inh} do not match within a few percent (relatively), the value of the factor k in the α -search is adjusted and step 3, 4, and 5 are repeated.

A value for k of 1.0078 turned out to yield a satisfying agreement between ρ_{stat} and ρ_{inh} for the deeper subcritical systems (systems with one or more shutdown rods inserted).

In PERT-V the parameter β_{eff} is calculated in the following manner:

$$\beta_{eff} = \sum_{k=1}^6 \beta_{eff}^k = \sum_{k=1}^6 \frac{\sum_{l=1}^{NIBC} \int dV \left\{ \sum_j (\chi_{d,l,j}^k \phi_j^*) \nu_{d,l} \sum_i (\Sigma_{l,i}^{(f)} \phi_i) \right\}}{\int dV \left\{ \sum_j (\chi_{f,j}^*) \sum_i (\nu \Sigma_i^{(f)} \phi_i) \right\}} \quad (3.23)$$

where

$NIBC$ = the number of fissionable isotopes (in practice only ^{235}U and ^{238}U are taken into account),

$\chi_{d,l,j}^k$ = the delayed fission source (spectrum fraction) for precursor decay group k for isotope

l in energy group j ,

$\nu_{d,l}$ = the absolute delayed neutron yield (per fission) for isotope l ,

$\Sigma_{l,i}^{(f)}$ = the macroscopic fission cross section for isotope l in energy group i ,
 χ_j = the static fission source (spectrum fraction) in group j ,
 $\nu\Sigma_i^{(f)}$ = the macroscopic fission neutron production cross section for group i ,

and the other symbols have their usual meaning. The generation time is calculated as

$$\Lambda = \frac{\int dV \left\{ \sum_i \frac{\phi_i \phi_i^*}{v_i} \right\}}{\int dV \left\{ \sum_j (\chi_j \phi_j^*) \sum_i (\nu \Sigma_i^{(f)} \phi_i) \right\}} \quad (3.24)$$

3.4 The kinetic parameter $\beta_{\text{eff}}/\Lambda$ at critical

3.4.1 Calculation of $\beta_{\text{eff}}/\Lambda$

The BOLD VENTURE diffusion theory code was used in R-Z geometry to compute the static neutron flux and the static adjoint function. Details of the treatment of the diffusion coefficients in the pebble-bed and in the cavity above the core region can be found in chapter 4. To obtain a critical system, the partially inserted control rods were represented by a grey curtain in which the ^{10}B nuclide density of the radial reflector was increased. The resulting reduction in k_{eff} corresponds to the specified worth in the critical balances [7]. The ^{10}B nuclide density in the radial reflector was then increased to represent the presence of the nuclear instrumentation, start-up source, etc. At this point, the calculations should yield $k_{\text{eff}}=1$ but in practice they don't because of inaccuracies in the data applied and the approximations in the calculational model. There are several ways to make the system critical of which two were chosen. The first way is to adjust the core height (without changing the densities) which is based on the idea that the effectiveness of neutron production in the core is not correct due to inaccuracies in the data applied. The second way is to change the radius of the core region (and simultaneously adjust the atom densities to maintain the correct total masses) which is based on the idea that the neutron streaming between core and radial reflector is not correct due to inaccuracies in the modelling of the core-reflector boundary. The changes in the core radius of core height necessary to make the system critical are modest as can be seen in table 3.1. The system is considered critical if the calculated value of k_{eff} is within 0.1 % of 1.

Table 3.1 Adjustments in core radius or core height to obtain criticality

| | core 5 | core 7 | core 9 | core 10 |
|-----------------------|--------|--------|--------|---------|
| change in radius (cm) | 0.73 | -0.69 | 1.255 | -1.15 |
| change in height (cm) | -2.71 | 0.6 | -1.6 | 0.95 |

The associated (static) flux and adjoint function have been used as shape and weighting function in the calculation of the kinetic parameters β_{eff} and Λ , as described in the previous section.

3.4.2 Measurement of β_{eff}/Λ

The value of β_{eff}/Λ can be obtained by making a fit of the theoretical APSD and CPSD (auto- and cross-power-spectral-density, respectively) to the measured spectra of the neutron detector signals. The advantage of this technique is, that it can be conducted in a critical system and thus avoids the need of an extrapolation to the critical state of subcritical PNS or noise measurements, a procedure which has been shown to yield accurate results only if proper account is taken of the kinetic behaviour of the system around critical [8]. It is a well-known technique that was already applied by Cohn [9] in 1959, and for example more recently by Ragan et al. [10]. However, the difference is that due to the long generation time of HTR-PROTEUS (1.5 - 2 ms), the prompt decay constant is of the same order of magnitude as the decay of the fastest delayed neutrons, and hence, no plateau in the APSD and CPSD can be recognised anymore. Consequently, the frequency range of interest is very low and for this reason, also the effect of the finite measurement time was considered.

Theory

Bennet [11] derived the following expression for the APSD of the fluctuating component of the current of an ionisation chamber:

$$W(\omega) = \frac{2\bar{i}^2}{\bar{C}} B(\omega) \left[Q + 2\epsilon D_v \sum_{p=1}^7 \frac{A_p s_p G(s_p)}{\omega^2 + s_p^2} \right] \quad (3.25)$$

where \bar{C} is the average count rate of the detector, \bar{i} the average current = $\bar{q} \cdot \bar{C}$, q the charge produced by one absorbed neutron, $B(\omega)$ the normalised frequency response of the detector (which can be taken unity for the experiments), $Q = \bar{q}^2 / \bar{q}^2$ a statistical factor of the ionisation chamber, ϵ the detector efficiency = \bar{C} / \bar{F} , \bar{F} the mean fission rate and $D_v = \bar{v}(\bar{v} - 1) / \bar{v}^2 = 0.795 \pm 0.007$, the Diven factor for ^{235}U [12]. A_p and $-s_p$ are the residues and poles of the reactor transfer function $G(s)$, which is given by

$$G(s) = \frac{1}{\Lambda s + \sum_{i=1}^6 \frac{s b_i}{s + \lambda_i} - \rho} = \frac{1}{\beta_{eff}} \frac{1}{\Lambda^* s + \sum_{i=1}^6 \frac{s b_i}{s + \lambda_i} - \rho_s} \quad (3.26)$$

where $\Lambda^* = \Lambda / \beta_{eff}$ is the reduced generation time, b_i is the relative fraction of delayed neutron precursors ($\sum b_i = 1$), ρ_s is the reactivity in dollar unit, and as usual, 6 delayed neutron precursor groups are used.

Equation (3.25) is the expectation value of the measured APSD if the measurement time is infinite. Of course, the detector signal is sampled during a finite time. This can be thought of as applying a Boxcar data window to the infinite time series data. Hence, the measured APSD corresponds to the Fourier transform of the auto-correlation function that is Bartlett (triangular) windowed [13], i.e.

$$W_m(\omega) = 4 \int_0^{T_0} \left(1 - \frac{t}{T_0}\right) R(t) \cos(\omega t) dt \quad (3.27)$$

where $R(t)$ is the auto-correlation function, obtained by applying the inverse Fourier transform to equation (3.25), and T_0 is the measurement time. Recall that $R(t)$ is an even function and $R(t > T_0) = 0$. Carrying out these calculations, one obtains:

$$W_m(\omega) = \frac{2\bar{i}^2}{C} \left[Q + 2\epsilon D_v \sum_p \frac{A_p s_p G(s_p)}{\omega^2 + s_p^2} \left\{ 1 + \frac{\omega^2 - s_p^2}{\omega^2 + s_p^2} \frac{1 - e^{-s_p T_0}}{s_p T_0} \right\} \right] \quad (3.28)$$

The first term in the right-hand side of Eq. (3.28), $2\bar{i}^2 Q / C$, is the noise spectrum of the detection process, which is white. The second term is the spectrum of the correlated counts, i.e. the counts due to neutrons belonging to the same neutron chain. The second term between brackets is the finite measurement time correction which is seen to become significant at low frequencies (for a typical HTR-PROTEUS configuration at frequencies < 0.1 Hz).

If two detectors are used, one can also compute the CPSD [14]. Since the detection processes in both detectors are uncorrelated, the white noise component disappears, leaving for the expectation value of the CPSD:

$$W_m^{12}(\omega) = \frac{4\bar{i}_1 \cdot \bar{i}_2}{F} D_v \sum_p \frac{A_p s_p G(s_p)}{\omega^2 + s_p^2} \left\{ 1 + \frac{\omega^2 - s_p^2}{\omega^2 + s_p^2} \frac{1 - e^{-s_p T_0}}{s_p T_0} \right\} \quad (3.29)$$

Although the CPSD normally is a complex quantity, note that in a point reactor it is a real quantity. This implies that in a point model there is no phase difference between the detector signals, irrespective of the detector positions.

The measured spectra were fit to Eqs. (3.28) and (3.29), with $2\bar{i}^2 Q / C$, $\epsilon / (Q\beta_{eff}^2)$ and $4\bar{i}_1 \cdot \bar{i}_2 / (F\beta_{eff}^2)$ as linear parameters and the reduced generation time Λ^* as the only non-linear parameter. For given b_i and λ_i , Λ^* is the only parameter at critical which determines the values of the roots $-s_p$ of the inhour equation (the denominator of Eq. 3.26), which for a critical system can be reduced to

$$\Lambda^* = \sum_{i=1}^6 \frac{b_i}{s_p + \lambda_i} \quad p = 0 \dots 5 \quad (3.30)$$

Obviously, the last root s_6 in a critical system is zero and thus independent of Λ^* . The roots in turn determine the values of the residues A_p and the values of $G(s_p)$, which are both inversely proportional to β_{eff} . Thus, by including β_{eff} to the linear fit parameters, its value is not required. The actual fitting is carried out by the non-linear least-squares routine VARPRO [15], which is an implementation of a modified Levenberg-Marquardt algorithm. The advantage of VARPRO is that no initial values for the linear fit parameters have to be supplied.

Experiment

The experiments were conducted in a critical reactor (with the autorod position frozen) at a power level of about 1 W. The neutron flux was measured with two uncompensated ionisation chambers, one placed in the side reflector, the other on top of the pebble bed in the radial centre. With a zero-suppression filter (cut-off frequency at 0.01 Hz), the DC-component was removed from the detector signals. After the remaining fluctuating components were amplified, they were sampled with a PC-based signal analysis system which calculated on-line the APSDs, the CPSD, and the coherence between the signals via FFT (fast Fourier transform) processing. A sampling frequency of 16 Hz was used, which along with a 256 points record, yields a record length T_0 of 16 s. As the analysis system also calculates the correlation functions via inverse FFT of the power-spectral-densities, 256 zeros are added to the record before the FFT in order to achieve an unbiased estimate for the correlation functions [16]. A side effect of this procedure which is relevant for the experiments, is that the frequency resolution of the spectra is doubled.

Per measurement, about 300 records were measured, corresponding to a total measurement time of about 80 minutes. The measurements were then stopped, because the flux was always seen to drift away slowly from the level at the beginning of the experiment. This can be expected since the reactor is critical and the autorod position frozen and hence, there is no force driving the neutron flux back to the original flux level. After a measurement was stopped, the flux level was brought back to its original value, the autorod was frozen again, and a new measurement was started. Eventually, the results of several measurements were averaged. These averaged spectra of the detector signals and the phase difference between them were corrected for the frequency response of the instrumentation channels:

$$\text{APSD : } W_{corr}(\omega) = \frac{W_{meas}(\omega)}{|H(j\omega)|^2} \quad (3.31)$$

$$|\text{CPSD}| : |W_{corr}^{12}(\omega)| = \frac{|W_{meas}^{12}(\omega)|}{|H_1(j\omega)| \cdot |H_2(j\omega)|} \quad (3.32)$$

$$\text{phase : } \phi_{corr}^{12}(\omega) = \phi_{meas}^{12}(\omega) + \phi_{H_1}(\omega) - \phi_{H_2}(\omega) \quad (3.33)$$

where $|H_i(j\omega)|$ is the magnitude and $\phi_{H_i}(\omega)$ the phase change of the frequency response of instrumentation channel i . The frequency responses of the instrumentation channels were measured as follows. The detector - which produces the input signal for the instrumentation channel - was replaced by a battery (to yield a proper DC level) and a noise source (producing white noise in the frequency range of interest) in parallel. According to systems theory, the frequency response of the instrumentation channel can be obtained directly by measuring the CPSD of its input and output, and dividing it by the APSD of the input signal. The coherence between input and output was about 0.96, and practically independent of frequency.

3.4.3 Results

The results of the calculations are summarised in table 3.2. The generation time is seen to vary between about 1.5 and 2 ms. The two chosen ways to make the system critical yield

Table 3.2 The calculated kinetic parameter $\beta_{\text{eff}}/\Lambda$ in a system made critical by adjusting the core radius. Between parentheses the values are given for a system made critical by adjusting the core height.

| | core 5 | core 7 | core 9 | core 10 |
|---|--|--|--|--|
| β_{eff} | $7.1986 \cdot 10^{-3}$ ($7.2003 \cdot 10^{-3}$) | $7.2848 \cdot 10^{-3}$ ($7.2849 \cdot 10^{-3}$) | $7.1806 \cdot 10^{-3}$ ($7.1815 \cdot 10^{-3}$) | $7.2201 \cdot 10^{-3}$ ($7.2196 \cdot 10^{-3}$) |
| Λ (ms) | 1.9639 (1.9580) | 1.5220 (1.5194) | 2.1349 (2.1311) | 1.8721 (1.8732) |
| $\beta_{\text{eff}}/\Lambda$ (s ⁻¹) | 3.665 (3.677) | 4.786 (4.795) | 3.363 (3.370) | 3.857 (3.854) |

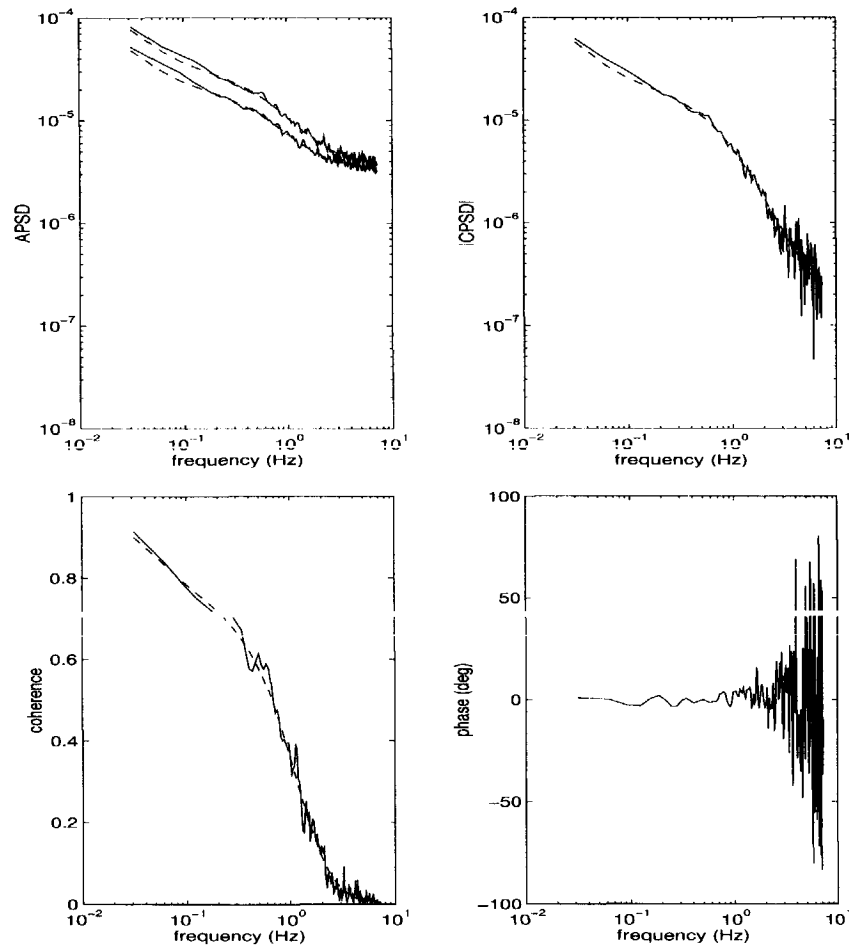


Figure 3.2 The upper plots show the measured (solid lines) and fitted (dashed lines) auto- and cross-power-spectral-densities in core 10. The lower plots show the corresponding coherence and phase difference between the signals

practically the same values for the kinetic parameter, with a maximum difference of only 0.3%. In table 3.3, the results of the measurements can be found. An example of the corrected APSDs and CPSD, together with the results of the least-squares fitting, can be seen in figure 3.2, which also shows the phase difference and the coherence between the detector signals.

Table 3.2 The calculated kinetic parameter $\beta_{\text{eff}}/\Lambda$ in a system made critical by adjusting the core radius. Between parentheses the values are given for a system made critical by adjusting the core height.

| | core 5 | core 7 | core 9 | core 10 |
|--|--|--|--|--|
| β_{eff} | $7.1986 \cdot 10^{-3}$ ($7.2003 \cdot 10^{-3}$) | $7.2848 \cdot 10^{-3}$ ($7.2849 \cdot 10^{-3}$) | $7.1806 \cdot 10^{-3}$ ($7.1815 \cdot 10^{-3}$) | $7.2201 \cdot 10^{-3}$ ($7.2196 \cdot 10^{-3}$) |
| Λ (ms) | 1.9639 (1.9580) | 1.5220 (1.5194) | 2.1349 (2.1311) | 1.8721 (1.8732) |
| $\beta_{\text{eff}}/\Lambda$ (s^{-1}) | 3.665 (3.677) | 4.786 (4.795) | 3.363 (3.370) | 3.857 (3.854) |

Table 3.3 The kinetic parameter $\beta_{\text{eff}}/\Lambda$ as obtained by fitting theoretical to measured spectra. The unit of the indicated uncertainties is one standard deviation.

| | core 5 | core 7 | core 9 | core 10 |
|-------------------------|-----------------|-----------------|-----------------|-----------------|
| # records | 368 | 500 | 1631 | 800 |
| APSD det.1 ¹ | 3.66 ± 0.19 | 5.29 ± 0.20 | 3.10 ± 0.29 | 4.05 ± 0.10 |
| APSD det.2 ² | 3.89 ± 0.17 | 5.24 ± 0.19 | 3.11 ± 0.12 | 3.87 ± 0.12 |
| CPSD | 3.69 ± 0.16 | 5.26 ± 0.11 | 3.01 ± 0.11 | 3.90 ± 0.10 |

¹ located in side reflector; ² located on top of pebble bed

Since the generation time is long, the prompt decay is quite close to the decay of the fastest delayed neutrons and as a result, no intermediate plateau can be recognised anymore. The figure also illustrates the elimination of the detection noise by the CPSD. The zero phase difference between the detector signals indicate that the point reactor model can be used indeed to describe the kinetic behaviour of HTR-PROTEUS in a frequency range up to at least 2 Hz.

3.4.4 Discussion and conclusions

The value of the kinetic parameter $\beta_{\text{eff}}/\Lambda$ is very small, even smaller than the values reported for the Japanese VHTR [17]. This is due to the small core dimension and the packing geometry which lead to a large fraction of core neutrons escaping to the reflector region. Here, the neutrons reside for a relatively long time before returning to the core. Hence, the generation time is sensitive to the absorption properties of the reflector. This means for example, that the insertion of an absorber rod in the reflector will not only change the reactivity, but also the kinetic parameter. The leakage from the core and thus the kinetic parameter is also influenced by the moderation in the core: as mainly fast neutrons escape from the core, an increase in moderation decreases the leakage. Thus, the neutron population in the reflector decreases relatively to the population in the core, as a result of which the generation time decreases. Since the change in the generation time is much more important than the change in β_{eff} , the value of the kinetic parameter increases, as is confirmed by table 3.4. The fact that the value of $\beta_{\text{eff}}/\Lambda$ in core 9 is lower than in core 5 can be explained by the increased core height.

Chapter 4

Critical balances of core configurations

The nominal reactivity of the critical state is by definition zero. This would be the target value for the calculations if the calculational model of the critical system would include all relevant details. However, to simplify the modelling of the system, some components are not taken into account, for instance the partially inserted fine control rods, the autorod, the nuclear instrumentation, and the start-up sources. Hence, the target value for the calculations has to be corrected for the reactivity effects of these components. Where possible these effects have been measured directly in the various configurations, but in many cases the values had to be calculated, estimated or scaled from other configurations. These results can be found elsewhere, along with a detailed description of the core configurations [1]. By adding the individual reactivity effects, the value of the excess reactivity of each “clean” configuration is obtained and can be found in table 4.1 below. These values are the target values for the calculations presented in this chapter.

Table 4.1 The excess reactivities of the four “clean” configurations

| core | 5 | 7 | 9 | 10 |
|---------------------------------|-----------------------|-----------------------|-----------------------|-----------------------|
| $\rho_{\text{excess}} (\phi)^1$ | 119.3 ± 2.0 | 72 ± 2.8 | 124.1 ± 2.5 | 74.5 ± 2.1 |
| k_{eff}^2 | 1.00866 ± 0.00015 | 1.00526 ± 0.00021 | 1.00902 ± 0.00018 | 1.00539 ± 0.00015 |

¹ ϕ is a dollarcent (0.01 β_{eff}). In core 7, $\beta_{\text{eff}}=7.27 \cdot 10^{-3}$, in the other cores, $\beta_{\text{eff}}=7.20 \cdot 10^{-3}$

² $k_{\text{eff}}=1/(1-\rho)$, see section 3.2.1. This is the quantity normally calculated by the codes.

4.1 Computational methods

First an overview is given of the INAS code system which is used for the calculation of the excess reactivity of the core configurations. The INAS code system is a collection of reactor physics codes in use at IRI. Some of these codes take into account the spatial heterogeneity by means of the Dancoff factor. The calculation of this factor is the subject of section 4.1.2. The procedure that is developed for the generation of a cross section library for HTR-PROTEUS configurations is described in detail in section 4.1.3.

4.1.1 INAS - the IRI reactor physics code system

The INAS code system (IRI-NJOY-AMPX-SCALE) shown in figure 4.1, comprises codes for the processing of data in the basic nuclear data files up to codes that perform three dimensional neutronic whole-core calculations. The description of the code system will be limited to those codes that were used for the analysis of the HTR-PROTEUS experiments.

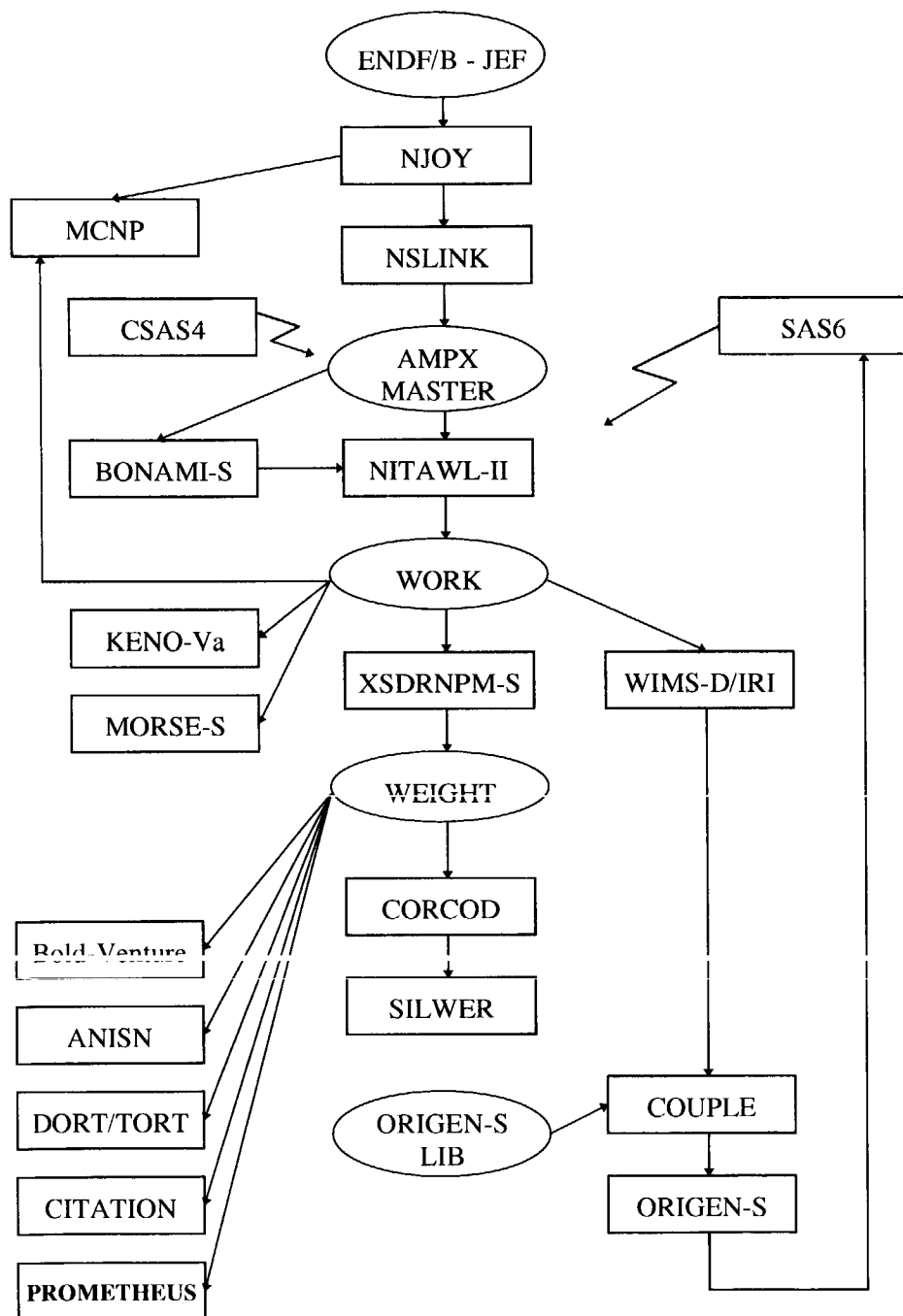


Figure 4.1 The INAS code system

The data in the JEF-2.2 basic nuclear data files have been processed with the codes NJOY [2] and NSLINK [3] resulting in an AMPX master library with the XMAS 172 energy group structure, resonance parameters for the resolved and unresolved energy ranges, a maximum Legendre order of three for the angular scattering distribution and data for eight temperatures. The data in this master library is further processed by the CSAS4 sequence of the SCALE-4 code package [4], specifically the modules BONAMI, NITAWL and XSDRNPM. BONAMI performs resonance shielding by the application of the Bondarenko shielding method [18] in the unresolved resonance range. It is normally used in combination with NITAWL, which applies the Nordheim integral technique [19] to process neutron cross sections in the resolved resonance energy range. Another function of NITAWL is the conversion of cross section libraries from a problem independent form to a problem dependent working library. In both the Bondarenko and the Nordheim method, use is made of a so-called Dancoff factor for the treatment of spatial heterogeneity. The definition and calculation of this factor is discussed in section 4.1.2. XSDRNPM is a one-dimensional discrete ordinates transport code used for the preparation of cell-averaged cross sections, as well as for one-dimensional criticality calculations.

For the whole-core calculations, use was made of the multigroup Monte Carlo code KENO-Va, which is also a part of the SCALE-4 code system, the two-dimensional, discrete ordinates, transport theory code DORT [5], and the diffusion theory code BOLD-VENTURE [6]. The advantage of KENO-Va over the two deterministic codes, is the possibility to model explicitly many details of the actual core geometry, for instance the fuel and moderator pebbles. Furthermore, KENO-Va is used along with a 172 energy group working library, whereas the two other codes were used with a cross-section library with 13 broad energy groups. For these reasons, KENO-Va also served as a reference for the transport and diffusion theory calculations.

4.1.2 Calculation of the Dancoff factor

In both the Bondarenko and the Nordheim method, heterogeneity of the system is taken into account by the Dancoff factor. The Dancoff factor is defined as the probability that a neutron emitted isotropically from the surface of the fuel region of the fuel element under consideration will have its next collision in the fuel region of any other surrounding fuel element [20]. Applying this definition to a pebble bed, Valko et al. [7] came with the suggestion to calculate the pebble-bed Dancoff factor (C) as the sum of the single-pebble Dancoff factor (C_{sp}) and the probability that a neutron leaves the first pebble (P_l), reaches another pebble (P_p) and is absorbed by fuel in that pebble (P_f):

$$C = C_{sp} + P_l P_p P_f \quad (4.1)$$

The single-pebble Dancoff factor C_{sp} is the probability that a neutron leaving one fuel particle reaches another fuel particle without collision and is calculated with DANCOFF-MC [8], a program based on the Monte Carlo method. In this program, all fuel elements in a sufficiently large neighbourhood of a selected fuel element are explicitly considered. C_{sp} is first determined as a function of radial position in the pebble, then it is averaged over the pebble. In this way a value of 0.268 was obtained for the fuel pebbles used in HTR-PROTEUS.

The probability P_l that a neutron leaves the fuel region of a pebble without scattering is given by

$$P_l = 1 - F_f - F_m \quad (4.2)$$

where F_f is the fraction of neutrons colliding with fuel and F_m is the fraction of neutrons colliding with moderator. The fraction F_f is equal to the single-pebble Dancoff factor C_{sp} . It is assumed that the ratio of neutrons colliding with fuel and with moderator is the same in the finite grain lattice (containing 9403 particles in a single pebble) as in an infinite grain lattice. Hence

$$\left(\frac{F_f}{F_m} \right)_{finite} = \left(\frac{F_f}{F_m} \right)_{infinite} \quad (4.3)$$

It can be determined analytically that in an infinite grain lattice the fraction F_f equals 0.4. This was confirmed by Monte Carlo calculations at ECN [9]. Using (4.3), the fraction F_m in the finite grain lattice is found to be $0.268/(0.4/0.6)=0.402$. Applying (4.2) yields a value for the probability P_l of $1-0.268-0.402 = 0.33$

The pebble Dancoff factor P_p is the probability that a neutron which left the fuel region of one pebble will arrive at the surface of another. It is calculated separately with DANCOFF-MC and is found to be 0.178 in core 5 and 0.112 in core 9.

The probability P_f is the probability that the neutron entering the fuel region of a pebble will be absorbed by fuel in that pebble. This definition resembles the Dancoff factor of a grain at the surface of the fuel region, but then the neutron may leave the grain also into a direction backwards into the pebble. Therefore, P_f can be approximated by two times the value of the radially dependent Dancoff factor at the surface of the fuel region of the pebble, which was calculated to be 0.2. Hence, $P_f = 2 \times 0.2 = 0.4$.

As a result, the overall Dancoff factors for cores 5 and 9 were found to be $0.268 + 0.33 \times 0.178 \times 0.4 = 0.292$ and $0.268 + 0.33 \times 0.112 \times 0.4 = 0.283$, respectively. These values were also used in cores 7 and 10 respectively, because the polyethylene rods occupy only 8.8% and 4.0% of the void volume between the pebbles, and secondly, the second term in the overall Dancoff factor contributes only about 9% and 5% respectively, to the total value.

4.1.3 The cross-section generation procedure

In order to calculate the broad group cross sections for the core region the double heterogeneity has to be taken into account. This double heterogeneity arises because of:

1. the fuel grains inside the fuel region of a fuel pebble
2. the pebble lattice containing fuel and moderator pebbles.

The following scheme was adopted that considers these two levels separately:

1. First only the fuel grains inside the fuel region of a fuel pebble are considered. An infinite close-packed hexagonal grain lattice is calculated by BONAMI, NITAWL and XSDRNPM. XSDRNPM is run in spherical geometry for a white boundary elementary cell of the grain lattice. The various layers of the coated particles are all included explicitly. A

cell-averaged weighted library, XSDWT(1), is produced which takes the self-shielding of the fuel grains into account.

2. An infinite pebble lattice is treated by BONAMI and NITAWL to obtain working library WRK(1). The pebble lattice unit cell has three regions. The innermost region is a homogenised fuel region of 4.7 cm diameter. This region is surrounded by a graphite shell of 0.65 cm thickness. The third region contains a homogenised mixture of graphite from a half (cores 5/7) or one (cores 9/10) moderator pebble and air. In case of cores 7 and 10, this third region also contains polyethylene. The equivalent diameter of the third region is 8.1225 cm and 8.94 cm for cores 5/7 and 9/10, respectively. This step is required because it provides the unweighted data for the materials outside the fuel region.
3. The library WRK(1) cannot be used for the pebble lattice cell calculation as it would not take into account the self-shielding in the fuel grains. Therefore the XSDWT(1) and WRK(1) libraries are merged. All fuel region materials are taken from the weighted library XSDWT(1), the other materials from WRK(1). The resulting library is called WRK(2).
4. XSDRNPM is run with working library WRK(2) for the unit cell of the infinite pebble lattice. If no axial dimensions are used, this run yields the k_{∞} of the lattice. Normally, XSDRNPM is run with a buckling search option to get a critical system (by the addition of a leakage term in the form of $DB^2\phi$). The weighted library XSDWT(2) with cell-averaged cross sections is produced.

The effect of self-shielding in the fuel grains can be quantified by comparing the multiplication factor k_{∞} of the infinite pebble lattice as calculated by XSDRNPM using WRK(1) and WRK(2). Since the effect will depend on the moderation in the core region, the best and worst moderated cores were chosen for the illustration. Table 4.2 lists the calculated values of k_{∞} .

Table 4.2 k_{∞} of the pebble lattice with (using WRK(2)) and without (using WRK(1)) considering the self-shielding effect of the fuel grains

| input library | core 5 | core 7 |
|---------------------|--------|--------|
| WRK(2) | 1.673 | 1.579 |
| WRK(1) | 1.594 | 1.560 |
| Δk_{∞} | 0.079 | 0.019 |

The most important effect of self-shielding in the fuel grains is the reduction of the resonance absorptions in ^{238}U which explains the increase in k_{∞} . As these resonances are located in the epithermal energy range, the self-shielding effect decreases with increasing moderation in the core. Nevertheless, even in core 7 the effect amounts to almost 2% which demonstrate the necessity of the extra steps in the cross-section generation procedure.

As the spectrum in the reflector region is considerably different from the spectrum in the core region, separate cross sections for the reflector region were calculated:

5. Cross sections for both core and reflector region are calculated by BONAMI and NITAWL. Use is made of a one-dimensional model that consists of an infinite cylinder with a core region of radius 59.854 cm surrounded by a reflector region of radius 163.10 cm. Control rod materials are added to the reflector region with a very low density. Working library WRK(3) is produced. Furthermore, an input file for XSDRNPM is produced by the CSAS4 run which will be used in step 7.

6. For the core region the weighted data calculated in step 4 must be used. Hence, the XSDWT(2) and WRK(3) libraries are merged. The core region materials are taken from XSDWT(2) and the materials in the reflector from WRK(3). The resulting library is called WRK(4).
7. XSDRNPM is run with WRK(4) for the one-dimensional model (see step 5) with a buckling search option. This run produces the libraries with the required number of broad groups in both AMPX and CCCC format by zone weighting, i.e. separately for core and reflector.

KENO-Va is used along with the 172 group cross section library WRK(4). DORT and BOLD-VENTURE both make use of a 13 group weighted cross-section library produced in step 7. The energy boundaries of the 13 groups can be found in table 4.3.

Table 4.3 The energy boundaries of the 13 broad energy groups

| group | E_{high} (eV) | group | E_{high} (eV) | group | E_{high} (eV) |
|-------|------------------------|-------|------------------------|-------|------------------------|
| 1 | $1.96403 \cdot 10^7$ | 5 | $7.48518 \cdot 10^2$ | 9 | 2.360 |
| 2 | $3.67879 \cdot 10^6$ | 6 | $1.36742 \cdot 10^2$ | 10 | 0.625 |
| 3 | $4.97871 \cdot 10^5$ | 7 | $3.05113 \cdot 10^1$ | 11 | 0.189 |
| 4 | $3.35463 \cdot 10^3$ | 8 | 8.3153 | 12 | 0.077 |
| | | | | 13 | 0.020 |

4.2 Modelling HTR-PROTEUS

The models described in this section were derived from a detailed description of the HTR-PROTEUS facility and its components [10]. More details of the applied models can be found elsewhere [11].

4.2.1 Two-dimensional model in deterministic codes

The DORT and BOLD-VENTURE calculations were performed using an R-Z geometry. A sketch of the various material zones is shown in figure 4.2. The core region was fully homogenised, where the possible partially fuelled top layer was explicitly taken into account. As the pebble density near the reflector boundary is lower than in the regular pebble lattice, the core was divided into an inner and outer core region. The inner core region contains 327 pebbles per layer and 654 vertical inter-pebble channels which each contain a CH_2 rod in cores 7 and 10. This region has an effective radius of 56.97 cm. The outer core region contains 34 pebbles and does not contain CH_2 rods in cores 7 and 10. In order to improve the treatment of the radial leakage, Mathews [12] suggested to choose a radius of the (cylindrical) outer core zone that conserves the radial surface area of the actual 12-sided polygonal surface of the core. Therefore, the radius of the outer core zone was chosen to be 60.55 cm instead of 59.85 cm, the radius that would conserve the core volume.

Graphite filler pieces were inserted to change the 22-sided polygonal shape of the radial reflector into a 12-sided polygon. Also the inner radius of the radial reflector was chosen as to conserve the actual radial surface area (62.93 cm instead of 62.71 cm). The correct total mass of the graphite filler pieces was maintained by adjustment of the atom densities. The radial reflector is assumed to extend to the same height as the upper axial reflector, i.e. 14.9 cm

higher than the actual height. The R-Z models comprise two rings in the radial reflector with a reduced density to account for the presence of the 8 shutdown rod channels and 4 control rod channels, respectively.

A simple model for the upper axial reflector was assumed. The graphite region (78 cm in height and with a radius of 62.93 cm) including 34 open channels is represented by a homogenised mixture of 94 vol% graphite and 6 vol% air. All the material (81.90 kg Peraluman-300, an aluminium alloy) of the upper reflector tank, the structure inside this tank to support the graphite, and the safety ring, is homogenised with air in a layer of 14.3 cm thickness below the graphite region. This region contains 17.5 vol% Peraluman-300 and 82.5 vol% air. The Peraluman-300 is represented by aluminium to which some ^{10}B is added to maintain the specified absorption cross section.

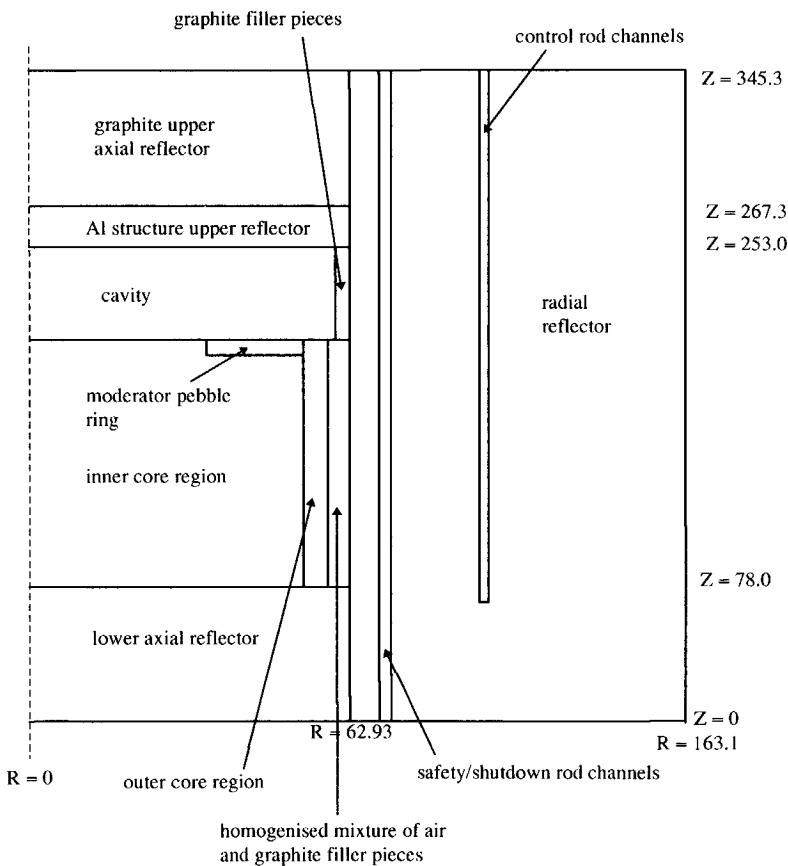


Figure 4.2 Representation of the R-Z model of core 5 (dimensions in cm)

4.2.2 Three-dimensional model in KENO-Va

In order to validate the energy group condensation procedure, the R-Z model of the deterministic codes was transferred into a KENO-Va model, including the homogenised core model. The only difference was that the channels of the safety/shutdown rods and of the fine control are modelled explicitly instead of being represented by a ring in the radial reflector of reduced atom density.

The second KENO-Va model is based on the first KENO-Va model, but instead of homogenising the core region, all the fuel and moderator pebbles, and in case of cores 7 and 10 the polyethylene rods as well, have been modelled explicitly. Only the 4.7 cm diameter fuel region of a fuel pebble was homogenised. The fuel region heterogeneity is taken into account in the cross section generation procedure, see section 4.1.3. Unfortunately, it turned out to be impossible to model the actual 12-sided core-reflector interface. For this reason, it was approximated by the smallest cylinder enclosing all pebbles. As in the R-Z model, the 22-sided inner boundary of the radial reflector was approximated by a cylinder with a radius of 62.93 cm. The density of the graphite filler pieces was increased to maintain the correct total mass.

4.3 Results

In the KENO-Va calculations each generation comprised 10000 neutron histories in order to obtain an unbiased estimate of k_{eff} [21]. To obtain good statistics, at least 130 generations were simulated, yielding a total of at least 1.3 million histories. These calculations require considerable computing power. Even on a fast DEC-alpha workstation, a typical KENO-Va run with the model in which all pebbles are explicitly represented, requires ~12 hours cpu time. A run with the much simpler homogenised core model still requires ~6 hours cpu time.

The DORT transport theory calculations make use of a P_3 Legendre expansion, S_{16} angular quadrature and 86×74 fine spatial meshes (mesh size about 2 cm). A DORT run requires ~2 hours cpu time. A spatial mesh size of 3 cm was found to be adequate in the BOLD-VENTURE diffusion theory calculations. In these calculations, the cavity was treated as recommended by Gerwin and Scherer [13]. However, as BOLD-VENTURE does not offer the possibility of a directionally dependent diffusion coefficient, the diffusion coefficient in the cavity was limited to the Gerwin and Scherer value in the axial direction in order to model the neutron streaming between core and upper axial reflector properly. This is considered to be more important than the correct modelling of the radial dependence of the neutron flux in the cavity. A normal BOLD-VENTURE run requires about 2 minutes cpu time.

4.3.1 Homogenised core region

The results obtained with the deterministic codes DORT and BOLD-VENTURE are shown in table 4.4 together with the result from the KENO calculations using a homogenised core. It is seen that all codes overestimate k_{eff} by 2.0 to 3.4 % ! Since KENO is used along with a 172 group library and DORT and BOLD-VENTURE both along with a 13 group library, it can be concluded that this overestimation is not due to the energy group collapsing procedure.

Table 4.4 The multiplication constants for the clean configurations calculated with codes employing a homogenised core model.

| | core 5 | core 7 | core 9 | core 10 |
|---|----------------------------------|----------------------------------|----------------------------------|----------------------------------|
| experimental | 1.00866±0.00015 | 1.00526±0.00021 | 1.00902±0.00018 | 1.00539±0.00015 |
| KENO (Δk in %) | 1.03125±0.00072 (2.259±0.074) | 1.03881±0.00062 (3.355±0.066) | 1.02933±0.00053 (2.031±0.056) | 1.03222±0.00053 (2.683±0.055) |
| DORT (Δk in %) | 1.03126 (2.26) | 1.03962 (3.44) | 1.03017 (2.12) | 1.03395 (2.86) |
| B.V. ¹ (Δk in %) | 1.03147 (2.28) | 1.03600 (3.07) | 1.03018 (2.12) | 1.03138 (2.60) |

¹ BOLD-VENTURE

4.3.2 Explicit modelling of pebbles

With the specified densities for the reflector graphite and JEF-2.2 data, the 2200 m/s absorption cross section was found to be 4.05 mb instead of the specified 4.09 mb. Boron densities have been adjusted to obtain the specified 4.09 mb absorption cross section. Calculations for cores 5 and 7 have been made using both the specified and the adjusted densities for the reflector graphite. The resulting values for k_{eff} are listed in table 4.5.

Table 4.5 The experimental and calculated (KENO) multiplication constants for the clean configurations

| | core 5 | core 7 | core 9 | core 10 |
|--|----------------------------------|----------------------------------|----------------------------------|-----------------------------------|
| experimental | 1.00866±0.00015 | 1.00526±0.00021 | 1.00902±0.00018 | 1.00539±0.00015 |
| $\sigma_a = 4.05$ mb (Δk in %) | 1.01610±0.00057 (0.744±0.059) | 1.00572±0.00051 (0.046±0.055) | - | - |
| $\sigma_a = 4.09$ mb (Δk in %) | 1.01507±0.00059 (0.641±0.061) | 1.00562±0.00048 (0.036±0.052) | 1.01106±0.00055 (0.204±0.058) | 1.00434±0.00059 (-0.105±0.061) |

As core 5 is much worse moderated than core 7, more fast neutrons leak from the core to the reflector, making the reflector more important for core 5 than for core 7. This explains why the same change in the reflector absorption cross section results in a larger reactivity effect in core 5 than in core 7. In contrast to the models with homogenised core regions, these detailed KENO models in which all pebbles are explicitly modelled yield values for k_{eff} which are in excellent agreement with the experimental values.

4.4 Streaming correction in diffusion theory

The usual homogenisation of a region conserves reaction rates, but if this region contains voids comparable in size to the neutron mean free path in that region, then the neutron diffusion properties are not conserved. In order to conserve the neutron diffusion properties in deterministic codes, streaming corrections must be applied. For transport theory, it is not straightforward how corrections should be applied. In diffusion theory, streaming corrections can be applied by modifying the diffusion coefficient of the homogenised region. Lieberoth and Stojadinovic [14] derived analytical expressions to calculate the correction factor for the diffusion coefficient in a homogenised region. However, they considered hexagonal close

packed and randomly packed lattices but not the columnar hexagonal packed lattices of the cores studied in this work.

To illustrate that their expressions are not valid for columnar hexagonal packed lattices, the diffusion coefficients in the core region were modified according to their expressions (yielding correction factors of 1.1463 and 1.1441 for core 5 and 7, respectively) and this was seen to decrease k_{eff} of core 5 by 0.94 % and of core 7 by 1.45 %. However, the KENO calculations with and without homogenised core show that the decreases in k_{eff} should have been 1.52% and 3.31%, respectively. Also note that the correction factor by Lieberoth and Stojadinovic is direction independent. In a columnar hexagonal packed lattice, the channels in the radial direction are much larger than in the axial direction. As a consequence, the neutron streaming in the radial direction is more important than in the axial direction. This effect can only be taken into account properly by separate correction factors for the axial and radial directions [15].

Unfortunately, the only possibility offered by BOLD-VENTURE to modify the diffusion coefficient in a region, consists of a single multiplier - hereafter called the diffusion coefficient modifier DCM - which is applied to the diffusion coefficients of all energy groups. Hence, this correction is not only energy independent but also isotropic. The DCM was varied until a value was found that yielded the same reduction in k_{eff} as resulted from the KENO calculations with and without homogenised core region. Table 4.6 summarises the required reduction in k_{eff} and the corresponding values of the DCM in each of the four investigated configurations. Table 4.7 shows the resulting values of k_{eff} along with the measured values.

Table 4.6 The required reduction in k_{eff} according to KENO and the corresponding diffusion coefficient modifier in each of the four investigated configurations.

| | Core 5 | core 7 | core 9 | core 10 |
|-----------------|-------------------|--------------------|-------------------|-------------------|
| Δk in % | 1.515 \pm 0.092 | 3.309 \pm 0.0803 | 1.827 \pm 0.076 | 2.788 \pm 0.079 |
| DCM | 1.2850 | 1.3769 | 1.2988 | 1.3621 |

Table 4.7 k_{eff} calculated with Bold-Venture, in which the DCMs of table 4.6 were applied.

| | Core 5 | core 7 | core 9 | core 10 |
|--------------------|-----------------------|-----------------------|-----------------------|-----------------------|
| measurement | 1.00866 \pm 0.00015 | 1.00526 \pm 0.00021 | 1.00902 \pm 0.00018 | 1.00539 \pm 0.00015 |
| calculation | 1.01510 | 1.00348 | 1.01100 | 1.00352 |
| (Δk in %) | (0.644) | (-0.178) | (0.288) | (-0.187) |

4.5 Discussion and conclusions

Table 4.5 shows that if KENO-Va is used to calculate k_{eff} and all pebbles are modelled explicitly, an excellent agreement with the measurements is achieved. However, calculations with MCNP4A by Joneja and Xu [16] indicate that the approximation of the 12-sided polygonal core-reflector interface by a cylinder reduces k_{eff} in core 5 by 0.345% whereas it does not significantly change k_{eff} in core 7. If this effect is taken into account, k_{eff} of core 5 would be even 0.99% too high, which is in agreement with the results of Monte Carlo calculations by ECN [17]. At ECN it is believed that the specified absorption cross section of the reflector graphite is too low. Analysing core 5, they achieved better results for both k_{eff} and the axial traverse of the normalised fission rate in ^{235}U by assuming that the reflector

absorption cross section was 9.5% higher than the specified value. However, they neither investigated the effect on the kinetic parameter $\beta_{\text{eff}}/\Lambda$, nor the effect on k_{eff} of the other loaded core configurations. Following the procedure described in chapter 3, the kinetic parameter for core 5 was re-calculated with a 9.5% increased reflector absorption cross section. Although the agreement with the experimental result is worsened (the percentage difference increased from $(-0.5 \pm 4.3) \%$ to $(4.2 \pm 4.5) \%$), it still is within the experimental uncertainty. Furthermore, a KENO-Va calculation for core 7 was performed using the increased reflector absorption cross section, which resulted in an underestimation of k_{eff} of 0.58% [17].

Hence, there are both arguments in favour and against the adjustment of the reflector absorption cross section. It is worthy to note that the agreement between the measured and calculated excess reactivity worsens as the amount of moderation in the core decreases. This might indicate shortcomings in the treatment of the resonances, for these resonances are located in the epithermal energy range, which importance increases with decreasing moderation.

Comparing the KENO-Va results in tables 4.5 and 4.6, it is seen that the homogenisation of the core region has a dramatic effect on the calculated value of k_{eff} . All models with a homogenised core region overestimate k_{eff} by 2.0% to 3.4%, depending on the core configuration. As mentioned before, this is the result of the underestimation of the neutron leakage from the core. It was expected that the overestimation would reduce with the leakage from the core, i.e. with core moderation. However, the overestimation is seen to increase with core moderation, which is believed to be the result of the overestimation of the probability that fast neutrons get thermalised inside the core region without leaking to the reflector. The overestimation of this probability increases with the size of the inter-pebble channels and the amount of moderating material in the core, both resulting for the homogenised core in a larger moderating material density at places where originally there was void.

It has been shown that the expression derived by Lieberoth and Stojadinovic cannot be used for the columnar hexagonal packed lattices. The applied procedure to determine the value of the correction factor for the diffusion coefficient of the homogenised region, requires results from Monte Carlo calculations with and without homogenised core region. Therefore, it only makes sense to determine the value of the DCM if besides the reactivity also other (integral) reactor parameters, like the kinetic parameter $\beta_{\text{eff}}/\Lambda$, have to be calculated which are not returned by the Monte Carlo program or cannot be derived from its output.

REFERENCES

- [1] Williams T.: *LEU-HTR PROTEUS: Configuration Descriptions and Critical Balances for Cores 1-7*, PSI technical memorandum TM-41-95-18, 1995
- [2] MacFarlane R.E., Miller D.W.: *The NJOY Nuclear Data Processing System Version 91*, Los Alamos National Laboratory, LA-12740-M, 1994
- [3] Leege P.F.A. de: *NSLINK: NJOY-SCALE-LINK User's Manual*, report IRI-131-091-003, Delft University of Technology, Delft, The Netherlands, 1991
- [4] *SCALE-4, A Modular Code System for Performing Standardized Computer Analyses for Licensing Evaluation*, NUREG/CR-0200 Rev.4. (ORNL/NUREG/CSD-2/r4), RSIC/CCC-545.

- [5] Rhoades W.A., Childs R.L., Emmett M.B.: *TORT-DORT, Two- and Three-Dimensional Discrete Ordinates Transport, Version 2.12.14*, Oak Ridge National Laboratory, CCC-543
- [6] Vondy D.R., Fowler T.B., Cunningham G.W.: *BOLD-VENTURE IV, A Reactor Analysis Code System, Version IV*, Oak Ridge National Laboratory, NEA CCC-459
- [7] Valko J., Tsvetkov P.V., Hoogenboom J.E.: "Calculation of the Dancoff factor for pebble bed reactors", paper submitted for publication to *Nucl. Sci. Eng.*
- [8] Feher S., Hoogenboom J.E., Leege P.F.A. de, Valko J.: "Monte Carlo calculation of Dancoff factors in irregular geometries", *Nucl. Sci. Eng.*, **117** (1994) 227-238
- [9] Stadt R. van der (ECN), personal communication, January 1996
- [10] Mathews D., Williams T.: *LEU-HTR PROTEUS System Component Description*, PSI technical memorandum TM-41-93-43, 1995
- [11] Wallerbos E.J.M., Hoogenboom J.E., Dam H. van: *IRI Results for LEU-HTR-PROTEUS Cores 5, 7, 9 and 10*, report IRI-131-97-005, Delft University of Technology, Delft, The Netherlands, 1997
- [12] Mathews D. (PSI), personal communication, August 1996
- [13] Gerwin H., Scherer W.: "Treatment of the Upper Cavity in a Pebble-Bed High-Temperature Gas-Cooled Reactor by Diffusion Theory", *Nucl. Sci. Eng.*, **97** (1987), 9-19
- [14] Lieberoth J., Stojadinovic A.: "Neutron Streaming in Pebble Beds", *Nucl. Sci. Eng.*, **76** (1980), 336-344
- [15] Mathews D., Thibulski V., Chawla R.: "Anisotropic Diffusion Effects in Deterministic Pebble Bed Lattices", *Trans. Am. Nucl. Soc.*, **68(A)**, 438, 1993
- [16] Joneja O.P., Xu Y.: *Monte Carlo Simulations of HTR-PROTEUS and Comparison with Measurements*, PSI technical memorandum TM-41-96-23, 1996
- [17] Wallerbos E.J.M., Hogenbirk A., Hoogenboom J.E.: "Calculations of Reactivity Effects of Water Ingress and Neutron Streaming in HTR-PROTEUS, a Small Low-Enriched Uranium Fuelled Pebble-Bed System", *Joint Int. Conf. on Mathematical Methods and Supercomputing for nuclear applications*, Saratoga, Oct 6-10, 1997
- [18] Bondarenko I.I. (ed.), *Group Constants for Nuclear Reactor Calculations*, Consultants Bureau, New York (1964)
- [19] Nordheim L.W., "The Theory of Resonance Absorption", *Proc. of Symp. in Applied Mathematics*, Vol. XI, p.58, G. Birkhoff and E.P. Wigner, Eds., Am. Math. Soc. (1961)
- [20] Bell G.I. and Glasstone S., *Nuclear Reactor Theory*, section 2.8, Van Nostrand Reinhold Company, New York (1970)
- [21] Gelbard E.M. and Gu A.G., "Biases in Monte Carlo Eigenvalue Calculations", *Nucl. Sci. & Eng.*, **117**, 1-9 (1994)

Chapter 5

The spatially dependent reactivity effect of various small samples

Knowledge of the reactivity effects of control elements and of abnormal events like water ingress in the core of an HTR, are of importance for the safe operation of the reactor under all possible conditions. To investigate the spatial dependence of the reactivity effects of materials that are either used in control elements or that play an important role in abnormal conditions, small samples of such materials were inserted into one of the six vertical inter-pebble channels in the radial centre of the columnar-hexagonal core configurations. Channels in the lower and upper axial reflector allow traverses to be made over the total system height. Since the reactivity effects to be measured are small (a few dollarcent at most), the inverse kinetics technique is in fact the only technique that can be used. The details of the experimental set-up are discussed in section 5.1, followed by an evaluation of the use of different experimental procedures in section 5.2. The calculation of the reactivity effect is the topic of section 5.3. The calculated reactivity effects depend on the product of the flux and the adjoint function, whereas on the other hand, reaction rates depend only on the flux. In order to get more insight into the results, in section 5.4 not only the calculated reactivity effects are compared to the measurements, but also calculated fission rates in ^{235}U (a good indication of the thermal flux) and in ^{238}U (a good indication of the fast flux). This chapter ends with a discussion of the results and some conclusions in section 5.5.

5.1 Experimental set-up

In the subsequent sections, an overview will be given of the samples oscillated, the instrumentation used for the experiments, and the processing of the experimental data.

5.1.1 The samples oscillated

The samples oscillated can be divided into two classes:

1. samples of absorbing material
2. samples of moderating material

Boron and gadolinium were the two selected absorbing materials, as these materials are frequently used in control rods or as burnable poison. The actual samples consisted of a small aluminium cylindrical container filled with Al_2O_3 powder through which a few milligrams of boron or Gd_2O_3 were mixed. The effect of a copper sample was also investigated as copper was used in core 6 to compensate the positive reactivity effect of CH_4 , with the aim to achieve a configuration having the same dimensions as core 5, but

Since the reactivity is measured while the sample is moving, this technique is referred to as the dynamic measurement technique. The alternative would be so called static measurements. In these measurements, the reactor is first made critical with the sample removed from the system, and then the sample is moved to one selected position. The resulting reactivity change is measured with the inverse kinetics or the stable period technique. To obtain an axial traverse, this measurement has to be repeated for all sample positions of interest.

The advantage of the dynamic measurement technique is that it requires less reactor time than the static measurements. The disadvantage is that the processing of the data is more involved (see section 5.1.3) and the possible presence of higher harmonics (dynamic effects). As the available reactor time was more important, the dynamic technique was selected as the standard technique. Nevertheless, in core 5 a series of static measurements was scheduled to investigate the possible presence of dynamic effects. An overview of all conducted measurements is given in table 5.2 below.

Table 5.2 Overview of conducted measurements

| core | current amplifier | measurement technique | number of detectors | movement signal measured | samples oscillated |
|------|-------------------|-----------------------|---------------------|--------------------------|--------------------|
| 5 | LCE ¹ | dynamic | 2 | no | all |
| | BBCA ² | static+dynamic | 1 | yes | 1,5 |
| | LCE/BBCA | dynamic | 1 | yes | 1 |
| 7 | LCE | dynamic | 2 | no | all |
| | BBCA | dynamic | 2 | no | 1 |
| 9 | BBCA | dynamic | 1 | yes | all |
| 10 | BBCA | dynamic | 2 | yes | all |

¹ LCE = linear channel electronics including the low-pass filter

² BBCA = broad-band current amplifier

5.1.3 Data processing

The processing of the accumulated data is briefly described here. More details can be found elsewhere [1]. In total, the data processing route comprises seven steps:

1. The measured signals are corrected for the offset of the A/D converters.
2. The reactivity is calculated according to Eq. (2.10), where the derivative is normally estimated by fitting a fourth-order polynomial to five consecutive data points and calculating the derivative of this polynomial in the midpoint. By taking the difference between the average reactivity before and after the insertion of the sample, the data processing for the static measurement technique is completed. The route for the dynamic measurement technique proceeds with step 3.
3. During a typical experiment, a sample is oscillated 10-20 times. To increase the accuracy of the measured reactivity, the results of these oscillations are averaged. To this end, each oscillation is shifted back in time until a match with the first oscillation is found. The required shift-in-time for each oscillation is given by the position of the maximum in the auto-correlation function of either the reactivity or the movement signal.
4. As the mean reactivity is still a function of time, the next step is to determine the sample position as a function of time. Since it is assumed that the reactivity effect of

upward and downward movements are expected to coincide if the reactivity is plotted against the sample position. Although the times that the sample starts or stops to move are measured in the majority of the experiments, the exact values are determined by minimising the difference between the reactivities of the upward and downward movements; see also section 5.2.1. The sample position as a function of time is then determined by a simple linear interpolation between the departure and arrival times.

5. The measured reactivities during the upward movement and during the downward movement are averaged. In general, the calculated positions at the sampling instants of the upward and downward movements are not equal, and a linear interpolation between two adjacent positions is used to compute the reactivity worth at the positions of the other movement.
6. Recall that two measurement series were required to cover the complete system height: one starting with the sample located at the top of the upper axial reflector and one starting with the sample located at the bottom of the lower axial reflector. The traverses of these two measurement series are combined. In the range where they overlap each other, this process is similar to the averaging of the upward and downward movements.
7. Since the perturbation is very small, it was not considered necessary to compute spatial correction factors. In case two or more detectors were used to measure the flux, it is expected that each detector yields the same result within experimental uncertainty, i.e. the validity of the point-kinetic theory is assumed. As a last step, the results of the detectors are averaged.

5.2 Evaluation of the use of different experimental procedures

The dynamic measurement technique, which is described in the previous section, is selected as the standard experimental procedure. This selection was made because dynamic effects are assumed not to be significant. This implies that the static and dynamic measurements should yield the same axial dependence of the reactivity effects. Furthermore, the measured reactivity effect should be independent of the detector position. Unfortunately, the broad-band current amplifier was not available for the first experiments, and therefore use was made of the linear channel electronics with the low-pass filter. The effect of this low-pass filter and the validity of the previously mentioned assumptions are investigated in subsequent sub-sections.

5.2.1 Dynamic effects

The possible presence of dynamic effects can be investigated by comparing the results of static and dynamic measurements. In core 5, both static and dynamic measurements were carried out using the boron and the CH_2 sample. It turned out that the measured movement signal needs two sample intervals (0.5 s) to change level when a sample starts or stops to move. Hence, the exact times of departure and arrival must be somewhere inside these intervals but are still unknown. These exact times were determined by minimising the difference between the upward and downward movements with the Nelder and Mead implementation of the simplex search-procedure [2]. They were all seen to fall within the measured intervals. It is observed that the sample moves down faster than it moves up: the velocity in downward direction is 26.06 cm/s whereas the velocity in the opposite direction is 24.02 cm/s. Along with a pause interval of ~ 20 s, this results in an oscillation

One detector was placed in the radial reflector, the other detector on top of the pebble bed at a radius of about 30 cm. Figure 5.4 shows the difference between the results achieved with these detectors for the boron and CH₂ samples.

5.2.4 Conclusions

Figure 5.2 shows that the static and dynamic techniques do not yield significantly different results. For this reason, it may be assumed that the dynamic effects are not significant. In the dynamic measurement technique, the exact departure and arrival times are determined by minimising the difference between the upward and downward movements. In section 5.2.2, it was observed that this procedure results in a wrong spatial dependence of the reactivity if use is made of the standard linear channel electronics to amplify the detector current. However, by using the values of the duration of the upward and downward movements, and of the pause interval determined in the broad-band current amplifier experiment, and only varying the first departure time to minimise the difference between the upward and downward movements, the resulting spatial dependence is in good agreement with that of the broad-band current amplifier. Therefore, the analysis of the measurements in core 5 and core 7 should start with experiments in which the broad-band current amplifier is used. Measurements with detectors placed at different positions in the system show a maximal difference at the axial position where also the magnitude of the reactivity effect is maximal. Although the differences are small (see figure 5.4), in case of the boron sample they are significant in the lower half of the core region. This could indicate the presence of a weak dynamic effect (weak because the effect was never seen to be significant when averaging the upward and downward movements). Therefore, it was not considered necessary to calculate spatial correction factors.

5.3 Calculations

The IRI-version of the first-order perturbation theory code PERT-V [4], which is based on the PSI-version of this code [5], computes not only the parameters β_{eff} and Λ , but also the reactivity worth per kg for all specified isotopes and specified reaction rates, both at all spatial mesh points. The flux and adjoint distributions were obtained with the BOLD-VENTURE diffusion theory code. These distributions were calculated with and without applying the streaming correction as described in chapter 4.

Since the streaming correction is maximal in core 7, a reference calculation for the axial flux distribution with the Monte Carlo code KENO-Va in this core was considered desirable. In order to simulate the experimental conditions, one of the six central CH₂ rods was removed in the core model and by removing graphite rods of 8.3 mm diameter in the lower and upper axial reflector, the free channel was extended to the full system height. The axial traverses of the flux and adjoint function were obtained by dividing the free channel into cylindrical 'detector' volumes of 6 cm height and 8.3 mm diameter. The thus obtained 172 group flux and adjoint function were condensed to 13 groups. Subsequently, the fission rates in ²³⁵U (F5) and ²³⁸U (F8) were computed by multiplication of the condensed flux with the microscopic fission cross-sections of ²³⁵U and ²³⁸U, followed by summation over all 13 groups. In a similar way, the spatial dependence of the reactivity effect of the absorbing samples could be calculated (see also section 5.3.2).

5.3.1 Flux distributions

To explain qualitatively the axial traverses of the fission rates and of the sample reactivity worths, it is useful to condense the 13 energy groups to just two groups, a thermal and fast group. The boundary between these two groups was chosen at 0.625 eV. The two-group flux and adjoint calculated by KENO-Va and by BOLD-VENTURE without applying a streaming correction, were normalised such that the fast flux and adjoint are unity at 51 cm above the bottom of the core. As the fluxes with and without applying a streaming correction are calculated for the same power level, the normalisation constant for the flux calculated without streaming correction is also used for the flux calculated with streaming correction. The normalised fluxes are shown in figure 5.5. According to first-order perturbation theory [8], the reactivity effect is proportional to the product of flux and adjoint function, which can be found in figure 5.6. The flux and adjoint function calculated with KENO-Va are shown in figure 5.7.

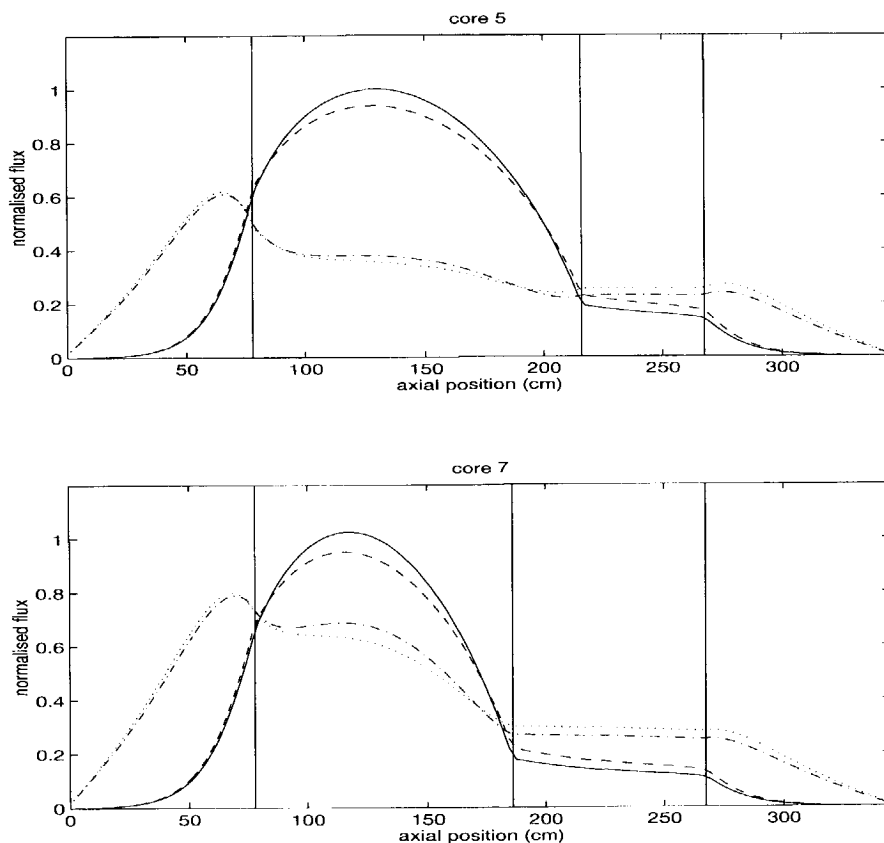


Figure 5.5 The normalised two-group flux in core 5 (upper plot) and in core 7 (lower plot). The solid line indicates the fast group without streaming correction, the dashed line the fast group with streaming correction, the dash-dotted line the thermal group without streaming correction, and the dotted line the thermal group with streaming correction.

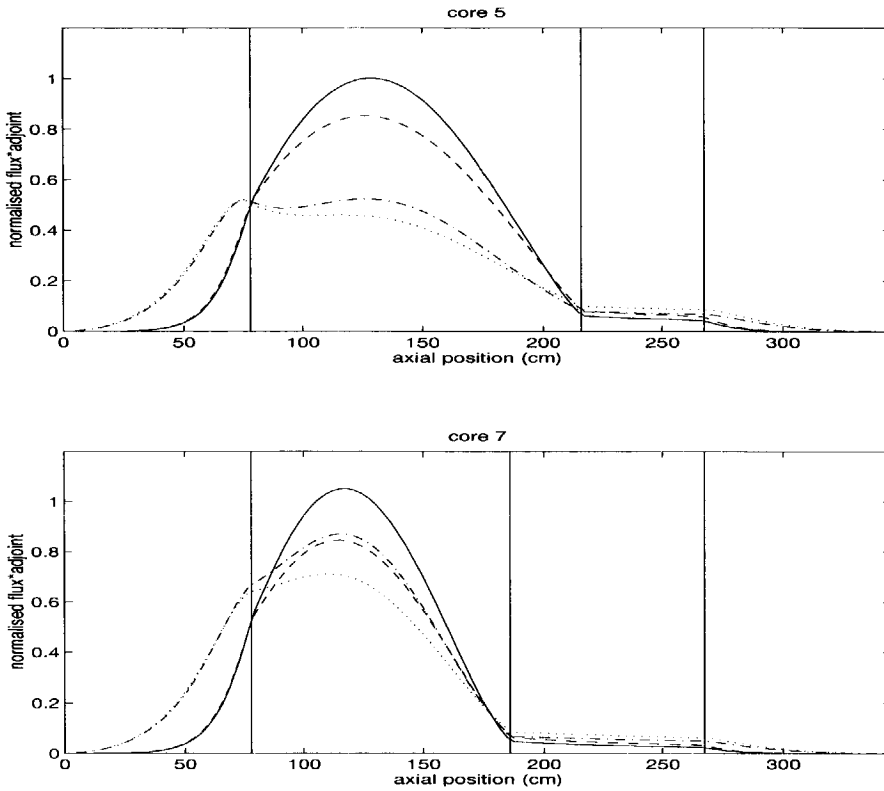


Figure 5.6 The normalised product of flux and adjoint function in core 5 (upper plot) and in core 7 (lower plot). The meaning of the lines is explained in the caption of figure 5.5.

The effect of the polyethylene rods becomes clear when comparing the upper and lower plots of figures 5.5 and 5.6. In core 7, the thermal flux (compared to the fast flux) is much higher than in core 5, which is due to the much better moderation in the core. The better moderation in the core also leads to a decrease of the peak in the thermal flux in the lower axial reflector relative to the thermal flux level in the core. Another effect is the reduction of the average energy of the fast neutrons, which increases the probability that they will finally induce a fission and thus increases the fast adjoint relative to the thermal adjoint.

Due to the applied streaming correction, the leakage from the core region increases which leads to a flatter flux shape in the core and a higher flux level in the cavity. As the probability of a neutron to escape from the core increases, the adjoint decreases relative to the adjoint calculated without streaming correction. Figure 5.7 shows that outside the core region, the flux calculated with streaming correction agrees well with the flux calculated with KENO-Va, but inside the core region, the flux without streaming correction is in better agreement. If the flux calculated with streaming correction is normalised to unity at 51 cm above the bottom of the core, then inside the core region the agreement with the flux from KENO-Va is excellent, but the flux level in the cavity and in the upper axial reflector is too high.

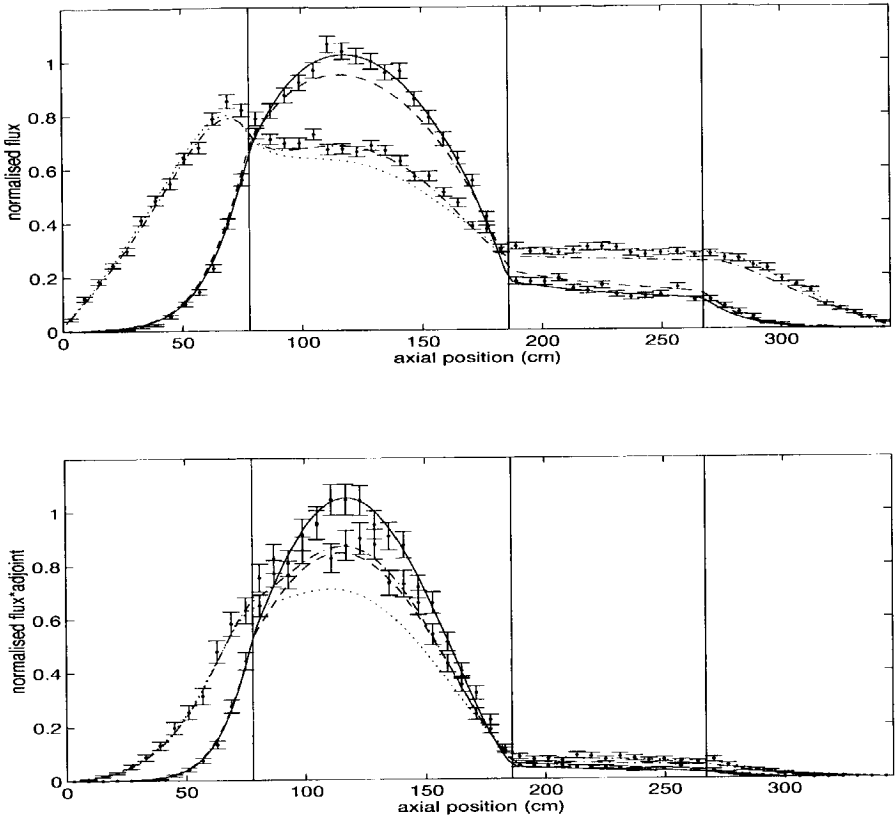


Figure 5.7 The normalised flux and the product of flux and adjoint in core 7 as calculated with BOLD-VENTURE and with KENO-Va. The KENO-Va results are indicated by error bars ($\pm 1\sigma$). The meaning of the lines is explained in the caption of figure 5.5.

5.3.2 The reactivity effect of a sample

The reactivity effect as calculated with first-order perturbation theory can be written as the sum of four components [5]

$$\Delta\rho = \frac{\Delta k_{eff}}{k_{eff}} = \frac{F + A + L + S}{D} \quad (5.1)$$

where the so-called perturbation denominator is

$$D = \frac{1}{k_{eff}} \int \left\{ \sum_j (\chi_j \phi_j') \sum_i (v \Sigma_i^{(f)} \phi_i) \right\} dV, \quad (5.2)$$

the fission neutron production component of the reactivity perturbation is

$$F = \frac{1}{k_{eff}} \int \left\{ \sum_j (\chi_j \phi_j^*) \sum_i (\delta [v \Sigma_i^{(f)}] \phi_i) \right\} dV, \quad (5.3)$$

the absorption component of the reactivity perturbation is

$$A = - \int \left\{ \sum_i (\delta [\Sigma_i^{(a)}] \phi_i \phi_i^*) \right\} dV, \quad (5.4)$$

the leakage component of the reactivity perturbation is

$$L = \int \left\{ \sum_i (\bar{\nabla} \phi_i \cdot \bar{\nabla} \phi_i^*) \frac{\delta [\Sigma_i^{(tr)}]}{3(\Sigma_i^{(tr)})^2} \right\} dV, \quad (5.5)$$

and the scattering (energy transfer) component of the reactivity perturbation is

$$S = \int \left\{ \sum_i \left(\sum_{j \neq i} \delta [\Sigma_{i \rightarrow j}^{(s)}] \phi_j (\phi_j^* - \phi_i^*) \right) \right\} dV. \quad (5.6)$$

In these equations the energy group indices i and j run from 1 to the number of energy groups, the integral is taken over the entire reactor volume, and

- ϕ_i = neutron flux in group i
- ϕ_i^* = adjoint function in group i
- χ_i = fission source (fission spectrum fraction) in group i
- $\Sigma_i^{(a)}$ = macroscopic absorption cross section for group i
- $\Sigma_i^{(tr)}$ = macroscopic transport cross section for group i
- $v \Sigma_i^{(f)}$ = macroscopic fission neutron production cross section for group i
- $\Sigma_{i \rightarrow j}^{(s)}$ = macroscopic scattering cross section from group i to group j

The diffusion theory approximation for the leakage component of the calculated reactivity effect does not work correctly in a low density region such as the cavity above the core [5]. For this reason, the leakage component of the reactivity was left out in the cavity. This, of course, introduces an error, but for the absorbing isotopes this error is seen to be very small. However, for a nuclide like hydrogen the error may be important. Hence, for all samples but the absorbing ones, the calculated reactivity effect in the cavity is considered to be unreliable.

The reactivity effect of a sample is calculated by multiplying the calculated reactivity effects of the isotopes (per kg) with the isotope masses given in the last column of table 5.1, and by adding these results. This total reactivity effect is in absolute units. Hence, by dividing this reactivity effect of the sample by the calculated value of β_{eff} , the reactivity effect of the sample in dollar units is obtained. The values for β_{eff} were taken from Ref. 6, which are in good agreement with the values calculated in chapter 3.

However, the thus calculated effect assumes that all the sample material is concentrated in one fine space interval. To get the effect of the real sample, the calculated effect is averaged over the length of the sample:

$$\bar{r}(z) = \frac{1}{L} \int_{z-\frac{L}{2}}^{z+\frac{L}{2}} r(x) dx \quad (5.7)$$

with:

- L : the length of the sample
- r : the calculated reactivity effect in dollar units
- z, x : the axial position
- \bar{r} : the averaged reactivity effect of the sample

Because of this averaging, the calculated reactivity effect as a function of the axial position becomes somewhat smoother, but it was seen to be only a small effect.

5.4 Results

5.4.1 The fission rates

Köberl [7] measured the reaction rates F5 and F8 by inserting miniature fission chambers in a vertical inter-pebble channel, and used activation foils to further reduce systematic uncertainties. These fission rates were normalised to unity at 51 cm above the bottom of the core and can be found in figures 5.8 and 5.9, along with the fission rates based on the BOLD-VENTURE fluxes. As BOLD-VENTURE calculated the fluxes with and without streaming correction for the same power level, the same normalisation is applied to both calculated fission rate traverses. Both in core 5 and in core 7, it is observed that the spatial dependence in the core region is best estimated without applying the streaming correction in BOLD-VENTURE, but that outside the core region, in particular in the cavity, the applied streaming correction yields a very good agreement with the experimental results, especially in the thermal energy region (i.e. F5).

Figure 5.10 shows the fission rates based on the flux calculated with KENO-Va. A good agreement with the experimental results is obtained, although the peak in F5 in the lower axial reflector is slightly overestimated.

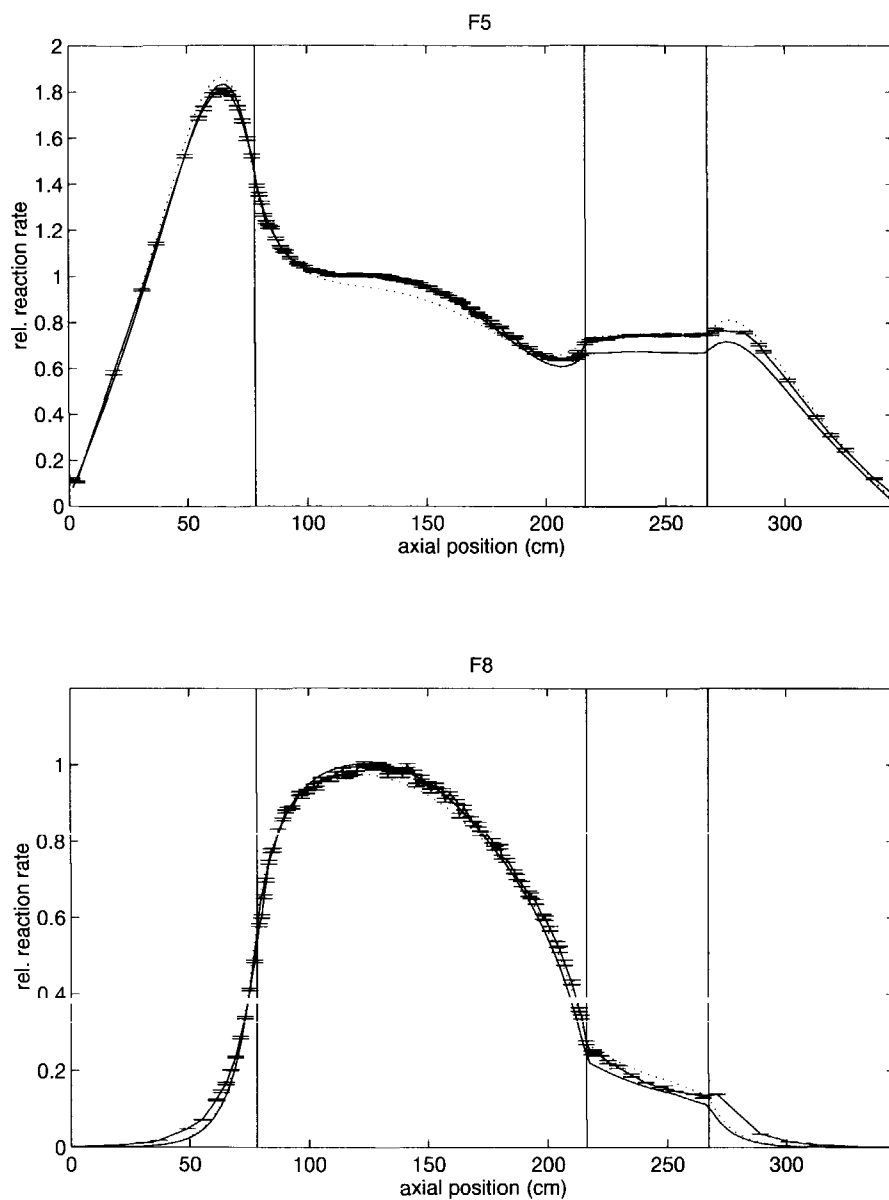


Figure 5.8 The axial traverses of the fission rates in ^{235}U (upper plot) and ^{238}U (lower plot) in core 5. The error bars indicate the experimental results ($\pm 1\sigma$), the solid line the fission rates calculated without streaming correction, and the dotted lines the calculations with streaming correction.

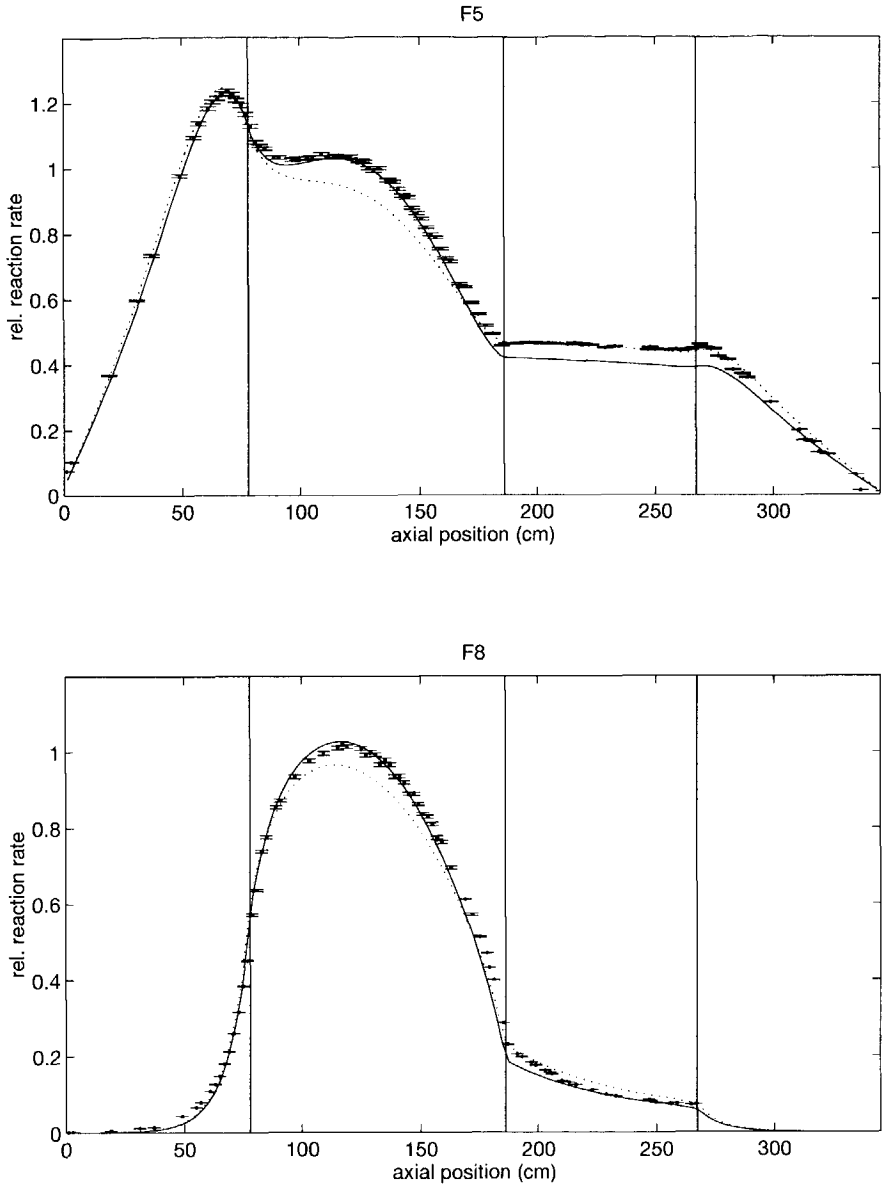


Figure 5.9 The axial traverses of the fission rates in ^{235}U (upper plot) and ^{238}U (lower plot) in core 7. The error bars indicate the experimental results ($\pm 1\sigma$), the solid line the fission rates calculated without streaming correction, and the dotted lines the calculations with streaming correction.

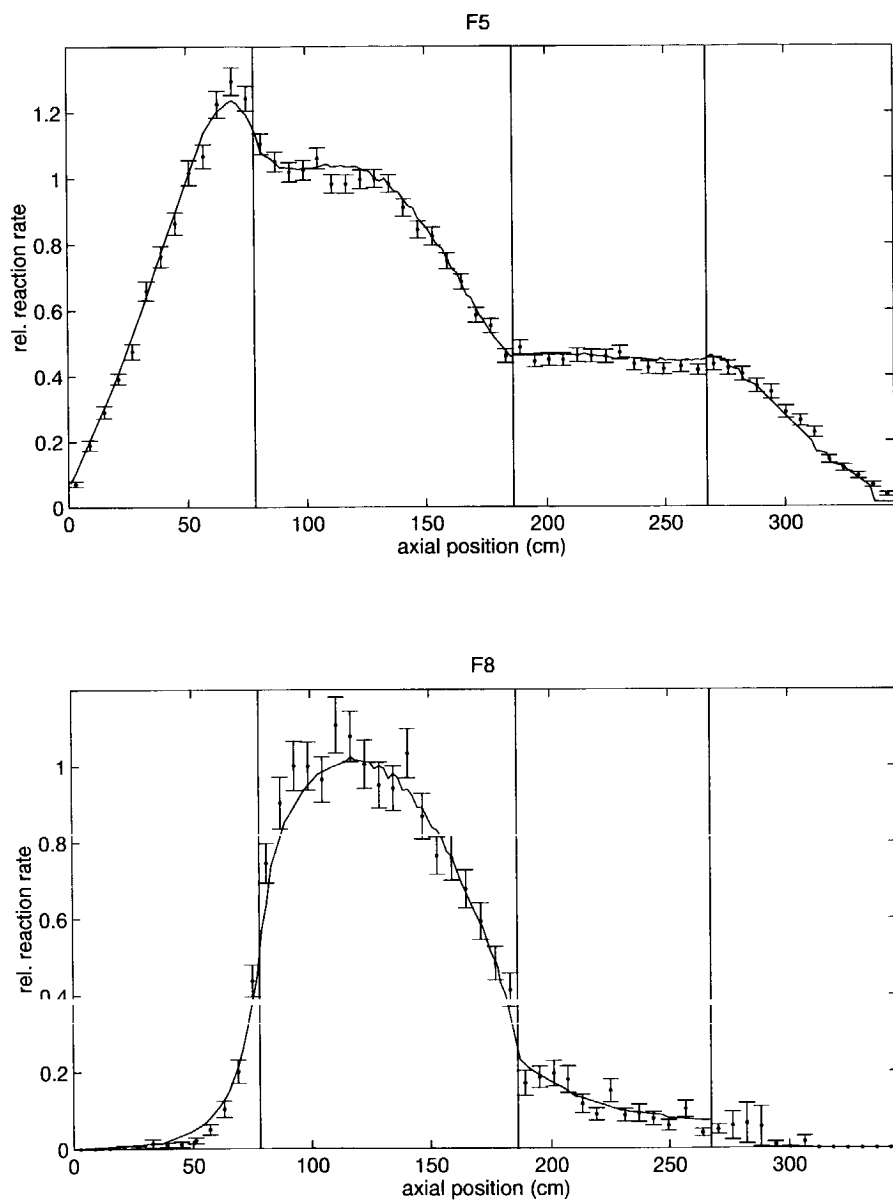


Figure 5.10 The axial traverses of the fission rates in ^{235}U (upper plot) and ^{238}U (lower plot) in core 7. The error bars indicate the KENO-Va calculations ($\pm 1\sigma$), the solid lines the experimental results.

5.4.2 The reactivity effects of the samples

The absorbing samples

Figures 5.11, 5.12, and 5.13 show the calculated and measured reactivity effects of the boron, the gadolinium, and the copper sample, respectively. These samples absorb mainly thermal neutrons and therefore, the shape of the reactivity effect is similar to that of the product of the thermal flux and the adjoint function shown in figure 5.6. Furthermore, the magnitude of the reactivity effect of the samples increases with the amount of moderation in the core. Comparing the magnitude of the reactivity effect in the core to the peak in the lower axial reflector in core 5 for all absorbing samples, it can be concluded that gadolinium is the most sensitive to thermal neutrons. This can be ascribed to the ratio of the thermal and epithermal absorption cross sections, which is the largest for gadolinium.

In order to compare the calculated spatial dependence of the reactivity effects of the boron sample to the measured spatial dependencies, the maximum reactivity effects were normalised to unity. As for the reaction rates, the same normalisation constant was used for the BOLD-VENTURE calculations with and without streaming correction. The resulting traverses can be found in figure 5.14. This figure shows that the agreement between the (normalised) experimental results and the calculations without streaming correction is excellent inside the core region (note that in core 5 the maximum is located in the lower axial reflector; if the results are normalised to unity 51 cm above the bottom of the core, a very good agreement is obtained), whereas outside the core region, the agreement with the calculations with streaming correction is very good.

The reactivity effects of materials like boron and copper are determined by the absorption component. Therefore, the spatial dependence of the reactivity effects of the boron and copper samples in core 7 could also be obtained by calculating the integral in Eq. (5.4), using the axial distributions of the flux and adjoint function calculated by KENO-Va. The resulting normalised traverses are shown in figure 5.15. This figure shows that with the flux and adjoint function from KENO one can well estimate the spatial dependence of the reactivity effects, without the use of corrections.

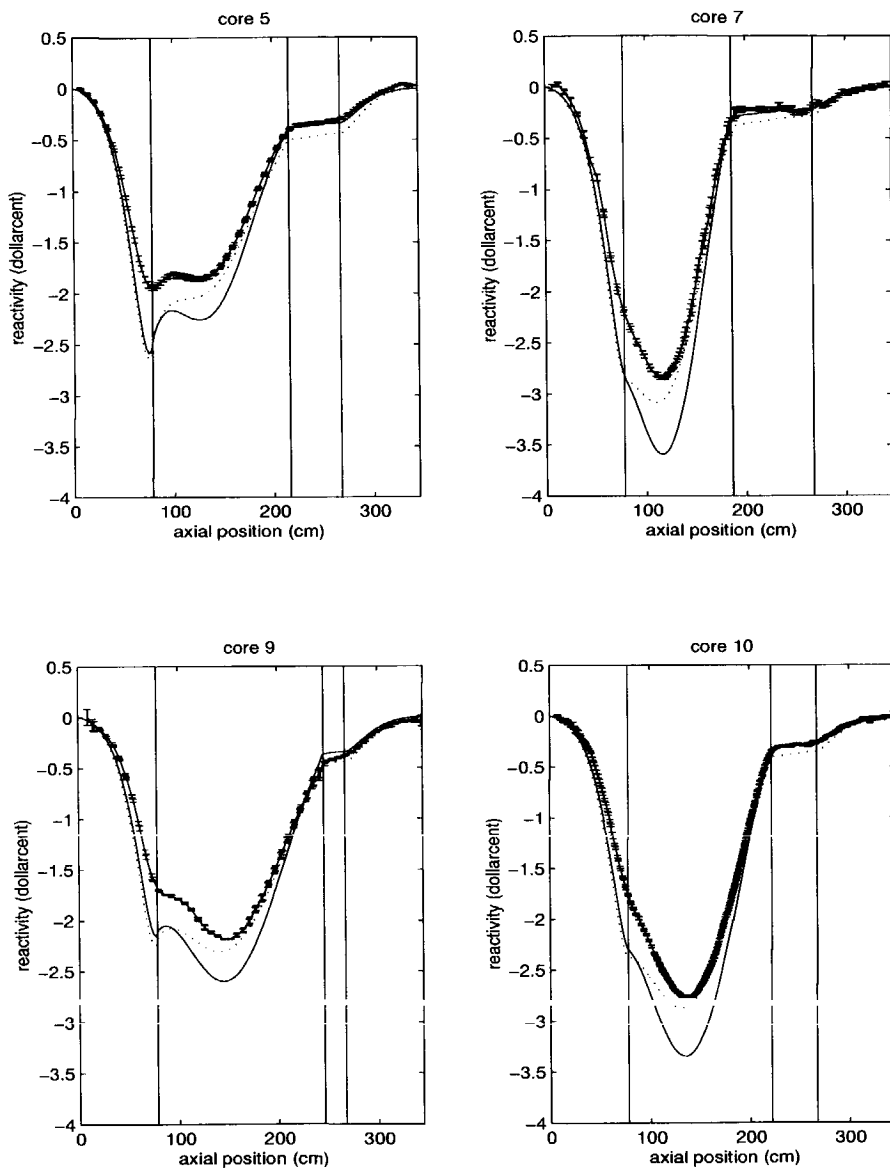


Figure 5.11 The reactivity effect of the boron sample. The error bars indicate the experimental result ($\pm 1\sigma$), the solid line the calculation without streaming correction, and the dotted line the calculation with streaming correction.

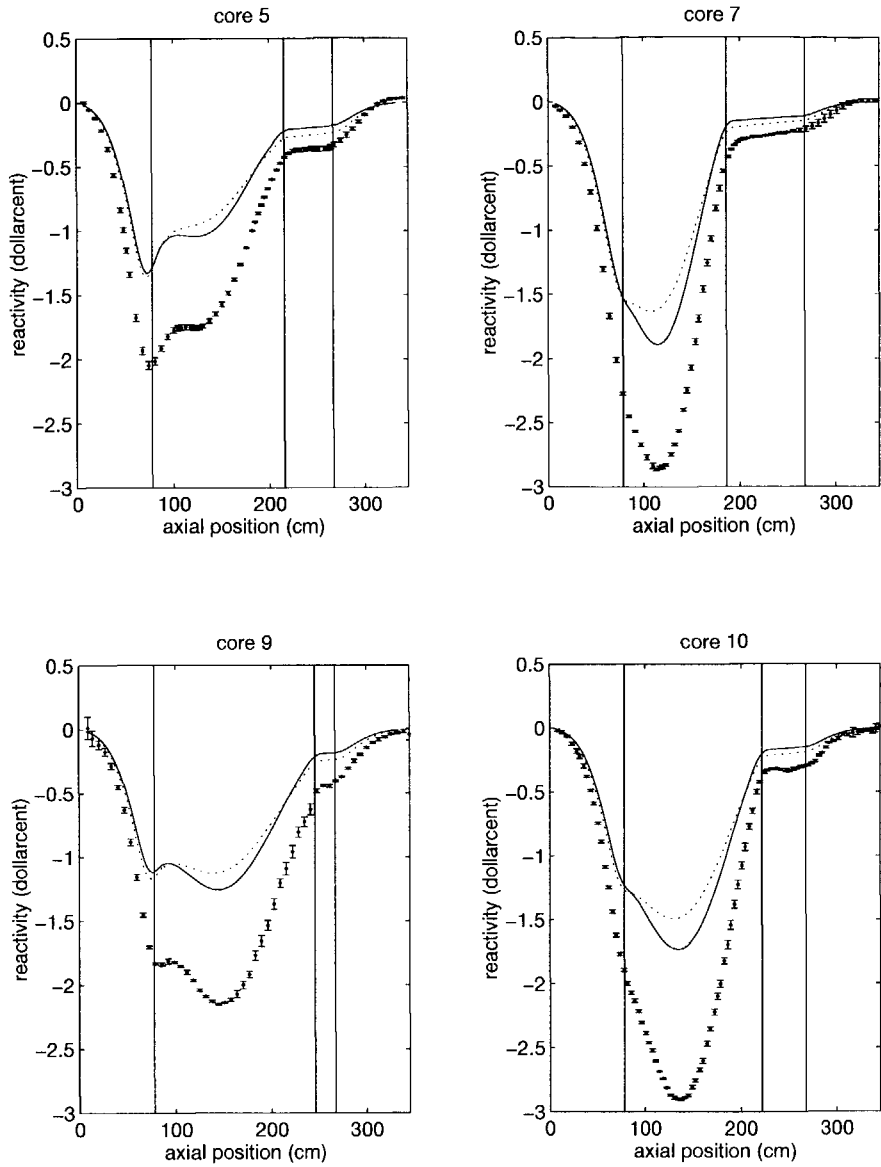


Figure 5.12 The reactivity effect of the gadolinium sample. The error bars indicate the experimental result ($\pm 1\sigma$), the solid line the calculation without streaming correction, and the dotted line the calculation with streaming correction.

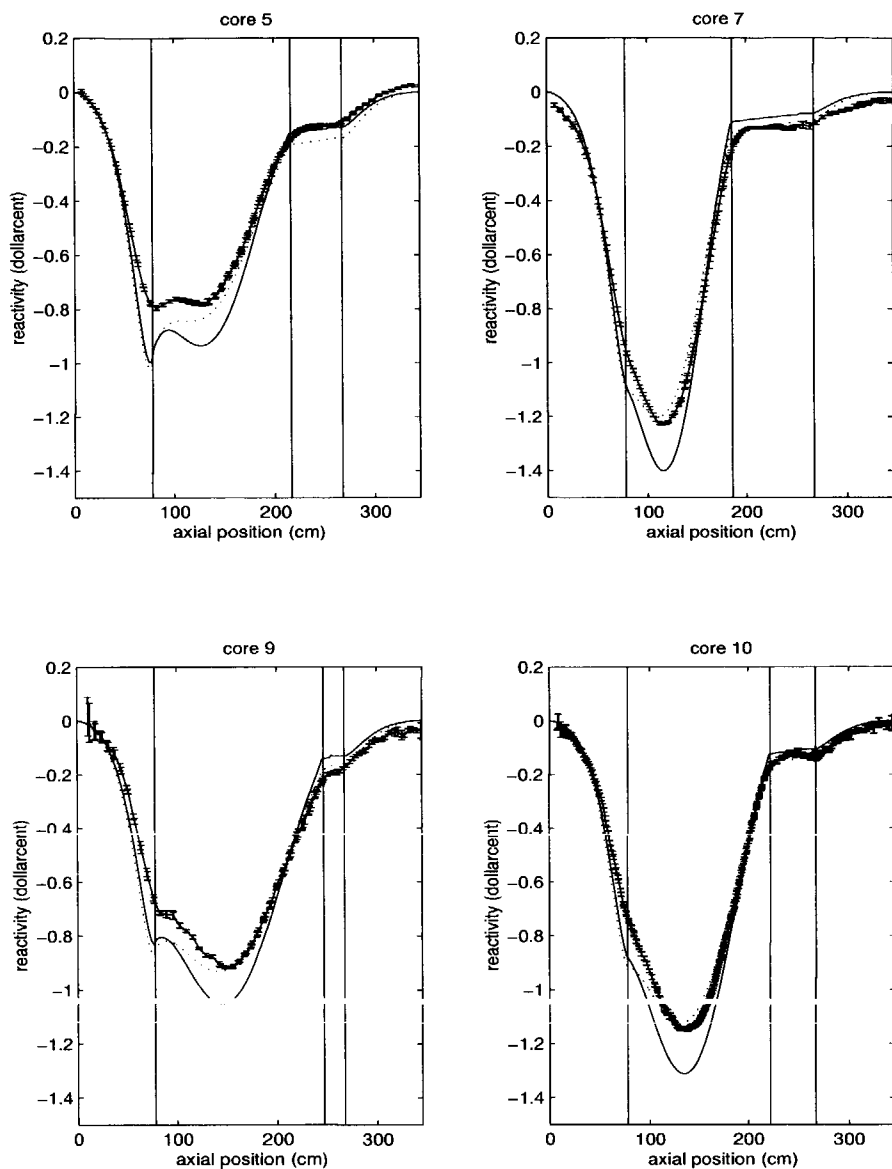


Figure 5.13 The reactivity effect of the copper sample. The error bars indicate the experimental result ($\pm 1\sigma$), the solid line the calculation without streaming correction, and the dotted line the calculation with streaming correction.

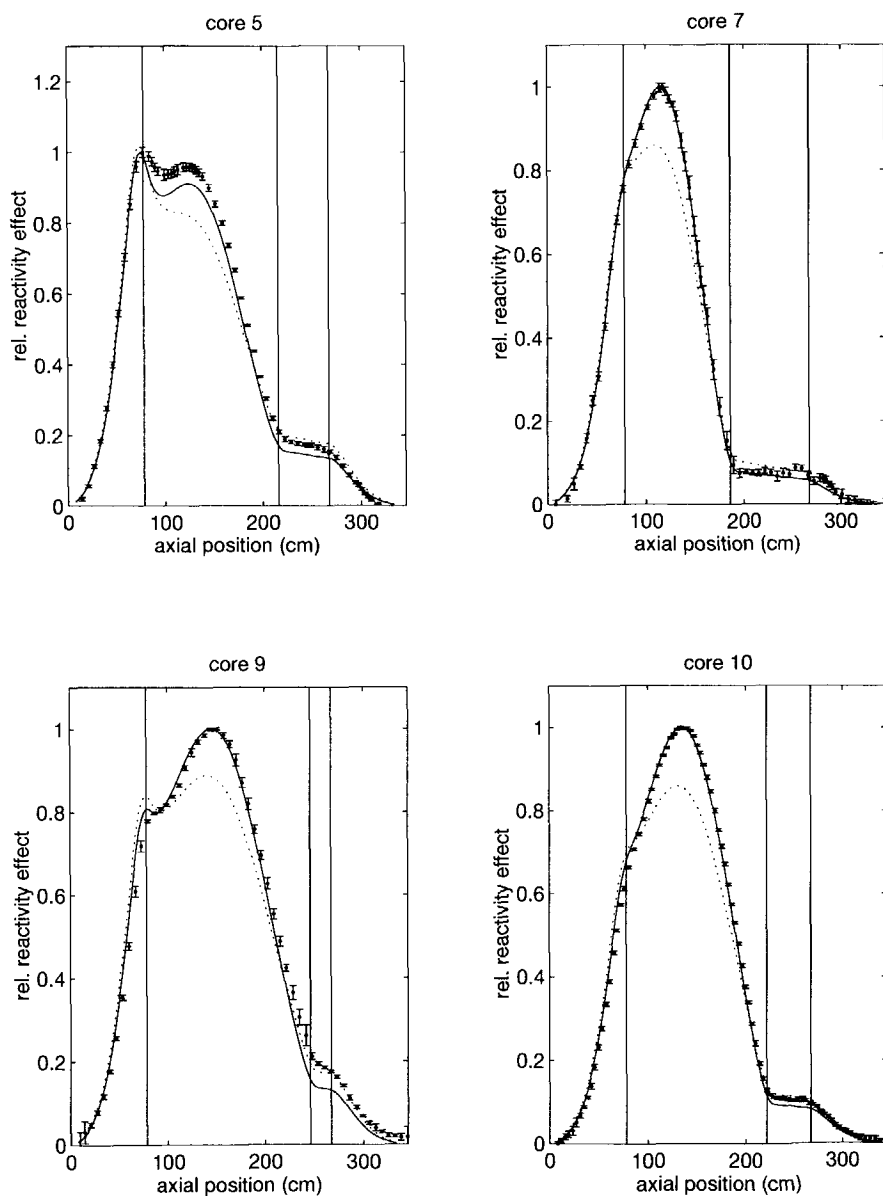


Figure 5.14 The relative reactivity effect of the boron sample. The maximum reactivity effect is normalised to unity.

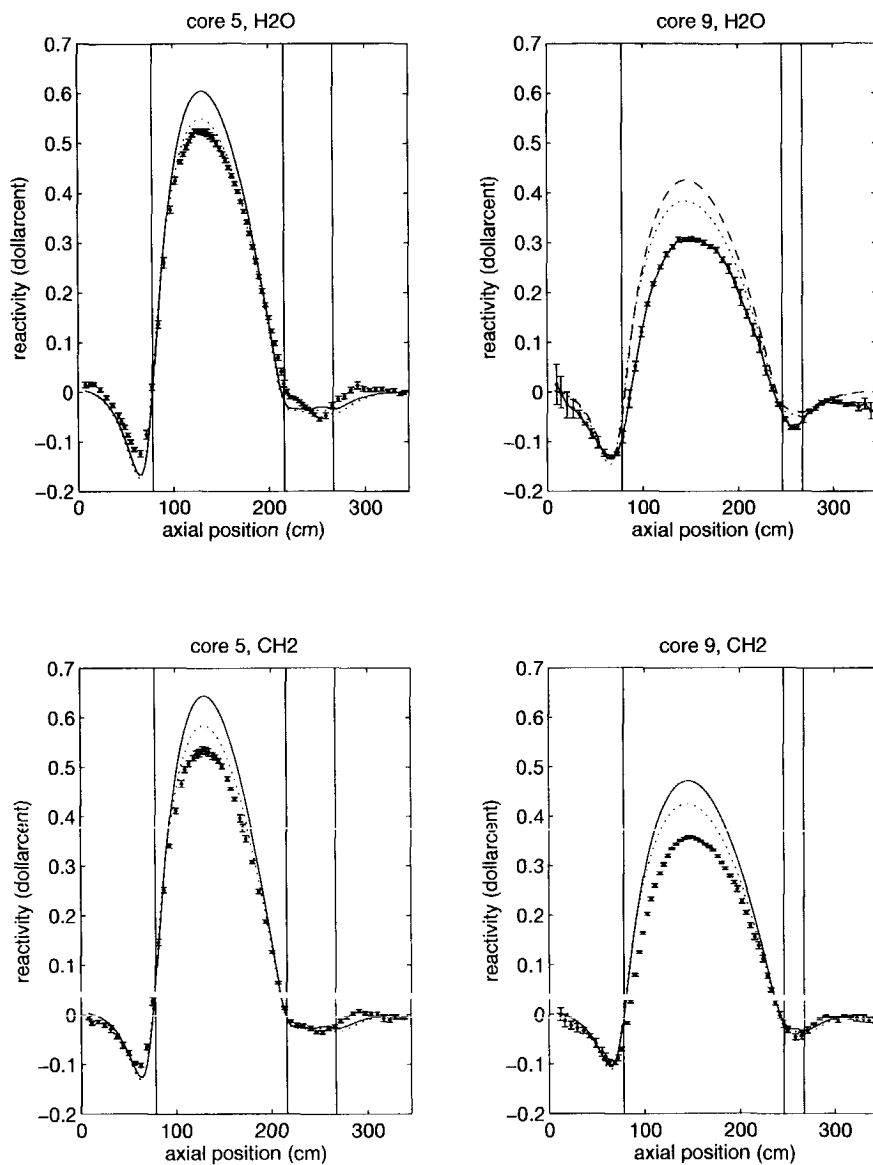


Figure 5.16 The reactivity effect of the water and CH₂ samples in cores 5 and 9. The error bars indicate the experimental result ($\pm 1\sigma$), the solid line the calculation without streaming correction, and the dotted line the calculation with streaming correction.

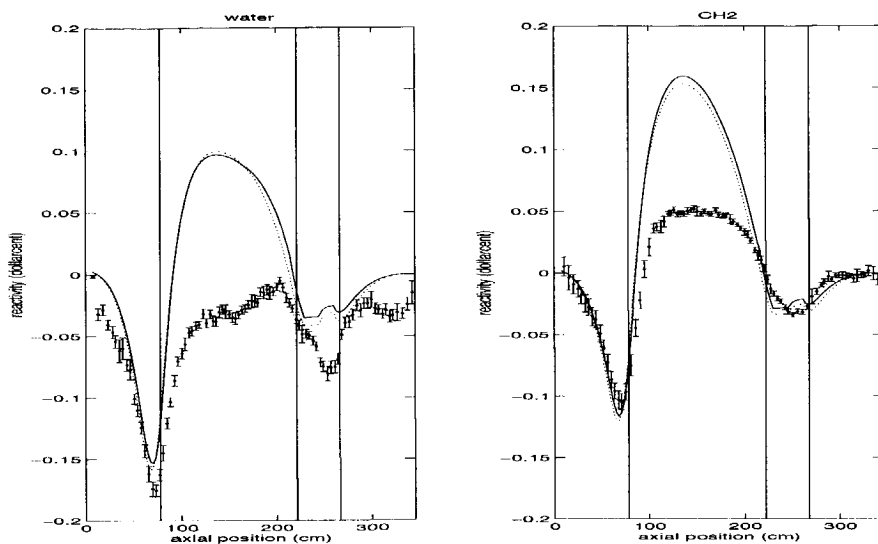


Figure 5.17 The reactivity effects of the water and CH_2 samples in core 10. The error bars indicate the experimental result ($\pm 1\sigma$), the solid line the calculation without streaming correction, and the dotted line the calculation with streaming correction.

Since in the PROTEUS configurations, the presence of water is simulated by CH_2 , it is of importance to compare their reactivity effects per mole. To this end, in core 9 also some CH_2 was put in an aluminium container and its effect was measured. By subtracting the effect of the bare CH_2 sample, the effect of the aluminium was determined and subsequently used to correct the measured effect of the water sample. Unfortunately, this experiment was not conducted in core 5. For this reason, the measured effect of the water sample was corrected with the calculated effect of aluminium (without streaming correction). The calculated effect was multiplied by 0.83 to take into account the overestimation of the calculation, see the results of the boron and copper sample.

Figure 5.18 shows the thus obtained reactivity effects per mole for CH_2 and H_2O along with the calculated effect. The measurements in core 9 show that polyethylene and water have the same reactivity effect per mole. The small difference (4-5% in the core region) observed in core 5 may be (partly) due to the calculational correction for the aluminium container. These results justify the use of polyethylene to simulate the presence of water. It is worthy to note that for equal reactivity effects per mole, the reactivity effect of polyethylene per unit mass is 28.4% higher than that of water, and per unit volume 20.7%. This is due to the differences in density and atomic mass.

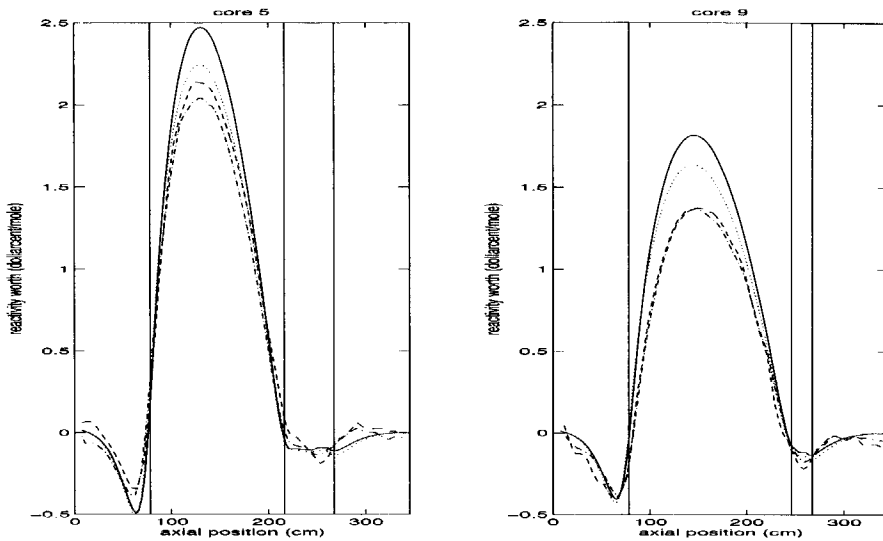


Figure 5.18 The reactivity effects of H_2O and CH_2 . The solid line indicates the calculated effect without streaming correction (the same for H_2O and CH_2), the dotted line the calculation with streaming correction (the same for H_2O and CH_2), the dashed line the measured effect of H_2O , and the dash-dotted line the measured effect of CH_2 .

5.5 Discussion and conclusions

Although the results can be explained qualitatively, the magnitudes of the reactivity effects of all samples but the gadolinium oxide one are overestimated. This could indicate an error in the gadolinium cross sections, but an error in the specification of the gadolinium sample composition is believed to be more likely. The overestimation of the boron and copper sample is about 17% in all core configurations (calculations without streaming correction). On the other hand, the overestimation of the moderating samples is seen to increase significantly with the amount of moderation in the core. It varies from about 21% in core 5, 32% in core 9 to even 208% in core 10. This looks dramatically, but note that the absolute difference between calculation and measurement at the position in the core where the reactivity effect is maximal, is about equal in all configurations. The reactivity effect in core 10 is much smaller than in cores 5 and 9 because of these three cores, core 10 is the only configuration with CH_2 rods inserted between the pebbles. In contrast to the reactivity effect of the absorbing samples, the effect of the moderating samples is mainly determined by the fast flux (and adjoint), which is in turn more affected by neutron streaming than the thermal flux. It is believed that the relatively large error in core 10 could be the result of an error in the treatment of the neutron streaming and/or in the moderation of fast neutrons, which also plaid a role in the overestimation of the effective multiplication constants by the homogenised core models in chapter 4. There, we have seen that the overestimation also increased with the amount of moderation in the core.

For the boron sample, the effect of self-shielding was investigated. As the calculated (thermal) macroscopic absorption cross-section of the boron sample amounts 0.2544 cm^{-1} , the self-shielding may be significant in the axial direction (recall that the sample length is 15.4 cm). Shielded cross-sections for the boron sample were generated with a three-zone slab geometry. The width of the first zone was equal to half the sample length, the dimensions of the two other zones were the radii of the core and radial reflector. With these shielded cross-sections, which will overestimate the self-shielding, the magnitude was reduced by 4.44%. It can therefore be concluded that self-shielding alone does not explain the overestimation.

The systematic overestimation could also be the result of the application of first-order perturbation theory. This theory assumes that higher-order terms (in general, these can be considered the combined effect of a (local) change in cross section and resulting perturbation in flux) can be ignored. From the preceding paragraph it can be concluded that the length of the boron sample equals about four main free paths for absorption, and therefore in the axial direction this sample is not that small in a neutronic sense. For this reason, the presence of the sample could lead to a significant perturbation in the axial flux distribution. It is therefore recommended to investigate the use of k-eigenvalue calculations for the configurations with and without the sample inserted. From the difference in eigenvalues the reactivity worth of the sample can subsequently be derived. In order to obtain the axial traverse, calculations with the sample at different axial positions have to be performed. Due to the absorptions in the sample, the use of transport instead of diffusion theory is preferred. Note that these two aspects will increase the required CPU time considerably.

It is seen that the magnitude of the reactivity effects calculated with streaming correction is in better agreement with the experimental results than the calculations without streaming correction. However, the spatial dependence in the core region is not correct. The analysis of the fission rate traverses yields the same result. The relative fission rates and the relative reactivity effect of the boron sample show that inside the core region, the agreement of the experimental results and the calculations without streaming correction is excellent, whereas outside the core region, the agreement with the calculations with streaming correction is very good.

Hence, it appears that the applied streaming correction can be used to calculate integral reactor parameters like the reactivity and generation time, but not differential parameters, like the flux distribution, in the region where the streaming correction is applied to. This is an unsatisfactory situation and more research is needed to find a method to treat the neutron streaming in deterministic codes such that correct values are simultaneously obtained for both integral and differential parameters. Such a method might also solve the problem of the overestimation of the reactivity effects. It is noteworthy that both the system reactivity and the spatial dependence of reaction rates and of reactivity effects of (absorbing) samples can be calculated correctly with KENO-Va, without the need to resort to corrections.

REFERENCES

- [1] Wallerbos E.J.M.: 'The Spatially Dependent Reactivity Effect of Various Small Samples in HTR-PROTEUS Cores 5 and 7', report IRI-131-96-007, *Interfaculty Reactor Institute*, Delft, The Netherlands (1996)
- [2] Dennis J.E. Jr. and Woods D.J., 'New Computing Environments: Microcomputers in Large-Scale Computing', edited by A. Wouk, SIAM, pp. 116-122 (1987)
- [3] Wallerbos E.J.M. and Mathews D.: 'Reactivity Effects of Small Samples in a Graphite-Moderated, Low-enriched Uranium Fueled, Critical Configuration', *Proc. Jahrestagung Kerntechnik '96*, May 21-23, Mannheim, Germany (1996)
- [4] Hardie R.W. and Little W.W. Jr. *Battelle Northwest Laboratory* report BNWL-1162 (1969)
- [5a] Mathews D.: 'The PSI Version of the PERT-V code', report TM-41-91-29, Paul Scherrer Institut, Villigen, Switzerland (1991)
- [5b] Mathews D.: 'Version "8 November 1993" of the PERT-V Code', PSI internal memorandum MD41-931108 (1993)
- [5c] Mathews D.: 'Version "31 March 1994" of the PERT-V Code', PSI internal memorandum MD41-940406 (1994)
- [6] Williams T., 'LEU-HTR PROTEUS: Configuration Descriptions and Critical Balances for the HTR-PROTEUS Cores', report TM-41-95-18, *Paul Scherrer Institut*, Villigen, Switzerland (1995)
- [7] Williams T., Köberl O., Mathews D., and Seiler R.: 'New Experimental Insights to the Neutrons Physics of Small, Low-enriched, High Temperature Reactor Systems', *Annual report 1995, Annexe IV*, *Paul Scherrer Institut*, Villigen, Switzerland (1996)
- [8] Ott K.O. and Neuhold R.J., "Introductory Nuclear Reactor Dynamics", *American Nuclear Society*, La Grange Park, Illinois, USA (1985)

Chapter 6

The reactivity worth of reflector-based absorber rods

HTR-PROTEUS was operated exclusively with reflector-based absorber rods. An overview of all rods is given in section 6.1. In section 6.2, an intercomparison of three different measurement techniques can be found. The reactivity worth of the auto-rod is discussed in section 6.3, followed by a study of the worth of the fine control rods in section 6.4. Section 6.5 deals with the reactivity worth of the shutdown rods. The chapter ends with conclusions in section 6.6.

6.1 An overview of absorber rods

There are three types of absorber rods:

1. the automatic control rod (auto-rod)
2. the fine control rods
3. the shutdown rods

The auto-rod is used to automatically maintain the critical reactor at a nominal required power. It uses a servo-mechanism to minimise the deviations from a specified value for the signal of a single ionisation chamber (the deviation channel). The rod itself comprises a wedge shaped copper plate supported within an aluminium tube. The copper plate is 3 mm thick, 230 cm long and is 39 mm at its wide end. Along the length of the plate, the width reduces every metre by 17 mm. In the fully inserted position, the tip of the copper plate is flush with the base of the system and the corresponding indication on the instrumentation panel is 0 mm. In fact, the panel shows the withdrawal of the auto-rod in mm. The maximum withdrawal amounts to 1000 mm. The auto-rod is situated at a radius of 89 cm and located azimuthally 80° from the x-direction in a clockwise direction, see figure 6.1.

Reactor control is achieved via four fine control rods which comprise an inner and outer tube, both of stainless steel. The composition of the tubes is given elsewhere [1]. If a rod is fully inserted, the stainless steel ranges from $z=75.5$ cm (2.5 cm below the core cavity) up to $z=295.5$ cm. If the rod is completely withdrawn, the lowest end of the rod is at $z=324.9$ cm, i.e. the maximum withdrawal is 2494 mm. When the rod is fully inserted, the indication on instrumentation panel is 2500 mm, when the rod is fully withdrawn the indication is 6 mm. The four rods are located symmetrically at a radius of 90.6 cm, see figure 6.1.

Reactor shutdown is ensured by means of four safety and four shutdown rods situated at a radius of 68.4 cm. The azimuthal positions of these eight rods are indicated in figure 6.1. Note that these eight rods are identical; either rods 1-4 or rods 5-8 are selected as shutdown rods. The remaining four rods are then referred to as the safety rods. The rods themselves consist of ~220 cm long stainless steel tubes, the lowest 210 cm of which are filled with six cylindrical borated steel pieces. The safety and shutdown rods are either fully withdrawn or fully inserted. In the last case, the borated steel ranges from $z=41$ cm up to $z=251$ cm. More details about the composition of rod materials, the azimuthal rod positions, and axial positions of the rod in fully inserted and withdrawn states can be found elsewhere [2].

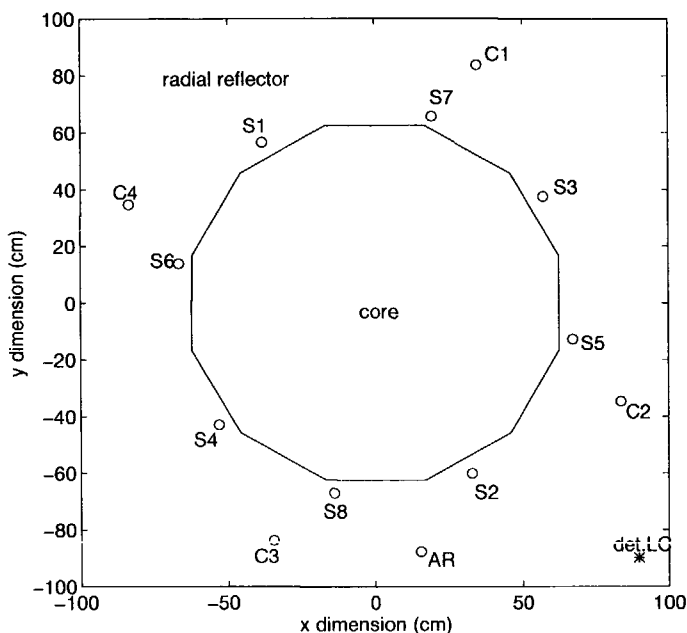


Figure 6.1 A schematic horizontal cross-section of HTR-PROTEUS. S_i indicates safety/shutdown rod number i , C_i fine control rod i , and AR the auto rod. Also indicated is the azimuthal position of the detector of the linear channel (LC) of the nuclear instrumentation.

HTR-PROTEUS could be operated exclusively with reflector-based absorber rods due to the small core dimensions, which result in a high neutron leakage from the core region to the surrounding reflector. Since the leakage depends on the amount of moderation in the core, so will the reactivity worth of the absorber rods. Furthermore, due to the steep thermal flux gradient in the (radial) reflector, the rod worth is very sensitive to the position of the rods. This is illustrated in figure 6.2, which shows the radial traverses of the ^{10}B absorption rate at half core height in the worst and best moderated core configurations. This distribution is based on the flux distribution calculated with the BOLD-VENTURE diffusion theory code (without applying a streaming correction to the core region).

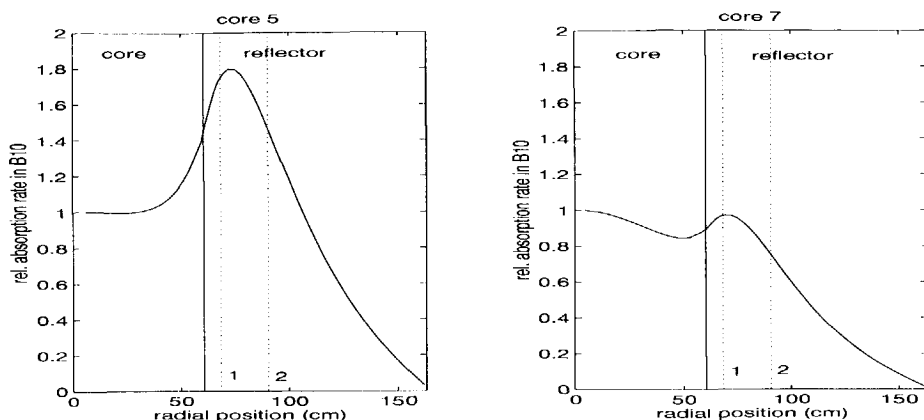


Figure 6.2. The ^{10}B absorption rate distribution at half core height in core 5 (left) and in core 7 (right). The dotted lines indicate the radii of the locations of the safety/shutdown rods ('1') and of the fine control rods ('2').

6.2 An intercomparison of three different rod-worth measurement techniques

6.2.1 Introduction

At four levels of subcriticality, three reactivity measurement techniques have been applied in order to study their applicability. These techniques are the inverse kinetics method (IK), the pulsed-neutron source (PNS) method and noise analysis techniques. Both the theory and experimental details of these methods can be found in chapter 2. In total four experiments have been performed in core 5, making the system subcritical by:

1. driving in the four fine control rods
2. dropping shutdown rod 7
3. dropping shutdown rods 5 and 6
4. dropping shutdown rods 5, 6, 7 and 8

In the first experiment, the IK method was not applied. Yet, to obtain an estimate for the reactivity, use was made of the measured calibration curve of the fine controls, which is discussed in section 6.4.3. In the second experiment, two detectors were used for the IK method, one located at the radial centre in the upper axial reflector, and the other one being the detector of the standard linear channel of the nuclear instrumentation. Also the PNS and noise analysis techniques each used two detectors. In experiments 3 and 4 however, for each method only one detector was placed in the system. Although during the first three experiments the spontaneous fissions in ^{238}U alone formed a neutron source that enables a sufficiently high count rate during the noise experiments, in the last experiment the start-up source had to be inserted.

6.2.2 The calculation of kinetics parameters and correction factors

The reduced generation time for use in the IK method was taken from table 3.2 in chapter 3 ($\Lambda^*_{\text{crit}}=0.273$ s). The calculation of the spatial correction factor is dealt with in section 6.5.3 and is not discussed here further. Table 6.1 shows the correction factors for the experiments which were taken from table 6.13.

Table 6.1 Spatial correction factor for analysis of IK measurements

| detector | experiment 2 | experiment 3 | experiment 4 |
|------------------|--------------|--------------|--------------|
| LC1 ¹ | 1.0033 | 1.0805 | 1.1129 |
| UAR ² | 1.0025 | - | - |

¹ detector of linear channel of nuclear instrumentation (for azimuthal position see fig. 6.1)

² detector at radial centre in upper axial reflector

The most accurate measurement of the prompt decay constant at critical yielded $\alpha_{\text{crit}}=4.51\pm0.02$ s⁻¹ [3]. The calculated value of the reduced generation time at critical was already mentioned in the preceding paragraph. The method to calculate the reduced generation time for use in the analysis of PNS-measurements has been discussed in chapter 3. Table 6.2 lists the calculated values of the reduced generation time for the four experiments.

Table 6.2 The reduced generation time for analysis of PNS measurements

| | exp. 1 | exp. 2 | exp. 3 | exp. 4 |
|----------------------------------|--------|--------|--------|--------|
| Λ (ms) | 1.9478 | 1.9558 | 1.9382 | 1.9074 |
| $\beta_{\text{eff}} \times 10^3$ | 7.2032 | 7.2087 | 7.2198 | 7.2421 |
| Λ^* (s) | 0.2704 | 0.2713 | 0.2685 | 0.2634 |

The introduction of an absorber to the reflector tends to decrease the generation time as the neutrons spend relatively less time in the reflector as opposed to the increase observed when an absorber is added to the core region. Somewhere around the core-reflector interface, the effects will cancel. This explains why the insertion of a shutdown rod (experiment 2) reduces the generation time less than the insertion of four fine control rods (experiment 1), despite the fact that the shutdown rod is a much stronger absorber. Furthermore, table 6.2 shows that β_{eff} slightly increases with subcriticality. This can be ascribed to the fact that relatively more prompt than delayed neutrons leak from the core to the reflector as a result of the higher average energy of the prompt neutrons.

Table 6.3 shows the calculated kinetic parameters for use in the noise analysis techniques. As mentioned in chapter 3, the static neutron flux distribution was chosen as shape function instead of the kinetic one. This is seen to result in lower values for the generation time (compare values in table 6.3 to those in table 6.2).

Table 6.3 The reduced generation time for noise analysis techniques

| | exp. 1 | exp. 2 | exp. 3 | exp. 4 |
|----------------------------------|--------|--------|--------|--------|
| Λ (ms) | 1.9303 | 1.9152 | 1.8483 | 1.8036 |
| $\beta_{\text{eff}} \times 10^3$ | 7.2036 | 7.2097 | 7.2258 | 7.2372 |
| Λ^* (s) | 0.2680 | 0.2656 | 0.2558 | 0.2492 |

Recall from chapter 3 that in the calculation of the kinetic flux the absorption cross section is increased by an amount of α/v . Since α is negative, this means that from both the core and reflector region the same amount of $1/v$ absorber is removed. Because the absorption in the reflector is lower than in the core, this removal has a larger effect in the reflector. Consequently, the flux in the reflector increases more than in the core, which explains the larger generation time values in table 6.2.

Note that the calculation of the reduced generation time and the spatial correction factor is an iterative procedure: in order to perform the calculations, the reactivity has to be known, but this is the parameter that we try to determine (using the calculated kinetic parameters). Fortunately, the calculated parameters are not very sensitive to small changes in reactivity, which limits the number of iterations required.

6.2.3 Results

In figure 6.3 an example is given of the IK analysis. The left-hand plot shows the normalised detector signal during experiment 3 (dropping shutdown rods 5 and 6) with (dotted line) and without (solid line) applying the spatial correction factor. In the right-hand plot the corresponding time-dependent reactivity (obtained from Eq. 2.10) can be found. The worth of the rods is the difference between the mean reactivity before the rod-drop (e.g. in figure 6.3 the mean reactivity in the time interval from $t=0$ s to $t=40$ s) and the mean reactivity after the rod-drop (e.g. in figure 6.3 the mean reactivity in the time interval from $t=60$ s to $t=130$ s). Since subsequent reactivity values are correlated, the variance in the rod-worth is taken to be the sum of the variances in the reactivity before and after the rod-drop.

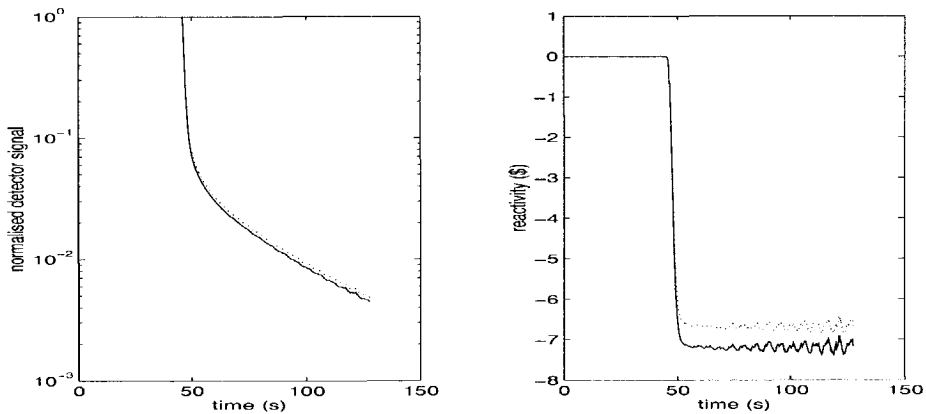


Figure 6.3 IK analysis of the simultaneous insertion of shutdown rods 5 and 6. The solid lines indicate the case in which no spatial correction factor is applied, the dotted lines the case including this correction (which amounts 1.0805).

Figure 6.4 shows the PNS response measured with shutdown rod 7 inserted. The plot on the left-hand side shows the total response. A simulated PNS equilibrium response is generated and fitted to the tail of the measured response (the start of this interval is indicated by the

vertical dotted line). The predicted response of the delayed neutrons is then subtracted from the measured response, leaving only the response of the prompt neutrons, shown in the right-hand plot. To this response, a single exponential function is fitted which yields the prompt decay constant. The reactivity is subsequently derived from Eq. (2.33).

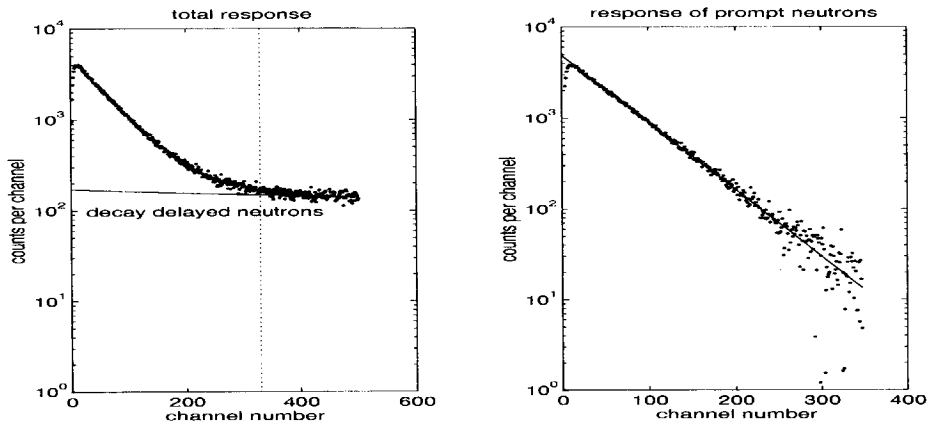


Figure 6.4. PNS response measured with shutdown rod 7 inserted. The channel width was 1 ms.

The emphasis in this section is put on the noise measurements. The reason is that the PNS and IK methods are adopted as standard measurement techniques at PSI, and therefore, these measurements are already described extensively elsewhere, e.g. [4]. Table 6.4 gives an overview of parameter values which are of importance for the noise analysis techniques. The low count rates in this table combined with a detector dead time of 1.5 μ s indicate that the effect of detector dead-time on the experimental methods (in particular the Feynman- α method) is small, except for the experiments performed in deep subcritical systems, i.e. in experiment 4.

Table 6.4 Parameters of noise analysis measurements

| | exp. 1 | exp. 2 | exp. 3 | exp. 4 |
|-----------------------|-----------------------|------------------------|------------------------|-------------------------|
| $N^{(1)}$ | 4095 | 4095 | 4095 | 4095 |
| $M^{(2)}$ | 50 | 50 | 26 | 50 |
| $\Delta t^{(3)}$ (ms) | 60 | 5 | 5 | 2 |
| $R^{(4)}$ det.1 | $12722 \pm 0.4^{(6)}$ | $1765.0 \pm 1.2^{(6)}$ | $1275.2 \pm 1.3^{(7)}$ | $11810 \pm 1.4^{(5,7)}$ |
| det.2 | $22961 \pm 0.7^{(7)}$ | $4804.1 \pm 2.3^{(7)}$ | | |

⁽¹⁾ number of channels per measurement

⁽²⁾ number of measurements

⁽³⁾ channel width

⁽⁴⁾ count rate in counts per second

⁽⁵⁾ external neutron source inserted

⁽⁶⁾ detector located on top of pebble bed

⁽⁷⁾ detector located in side reflector

Figures 6.5 to 6.7 show the results of Feynman's variance-over-mean, Bennet's δ -variance, and the auto-correlation analysis, respectively. The covariance and cross-correlation have also been calculated, but they are not shown here as they are similar to the variance-over-mean

ratio and to the auto-correlation, respectively. The figures illustrate how the amplitude of the experimental quantities decreases with subcriticality. This is due to the fact that the neutron chains become shorter with subcriticality and hence, the probability of detecting correlated neutrons (i.e. neutrons from the same chain) decreases. For the same reason, the uncertainty increases with subcriticality (assuming that the total number of measured channels and the count rate remain the same).

The variance-over-mean ratios shown in figure 6.5 yield experimental evidence for the effect of the finite number of channels. Although the statistical accuracy of the variance-over-mean ratio in experiments 2 and 4 is rather poor, it is obvious that it reduces as the count time (i.e. channel width) increases, which is in agreement with the predictions in chapter 2. The effect is most obvious in experiments 2 and 4, as in these experiments the number of broad channels is smaller than in the other experiments. For example in experiment 2, from the 4095 channels of 5 ms width, only 11 channels can be made with a width between 1.71 s and 1.86 s, and only 10 channels with a width between 1.86 s and 2.045 s. This small number of broad channels also explains the steps in the fitted curves. Note that in contrast to the variance-over-mean ratio, the δ -variance in experiment 4 reaches a saturation value, independent of the number of broad channels.

Furthermore, as in chapter 2, the models with and without the effect of the finite number of measured channels are fitted to the variance-over-mean ratio measured with detector 1 in experiment 1. The thus obtained values for the reactivity are shown in figure 6.9 as a function of the length of the fit interval. This experimental result confirms the results of the numerical experiment in chapter 2.

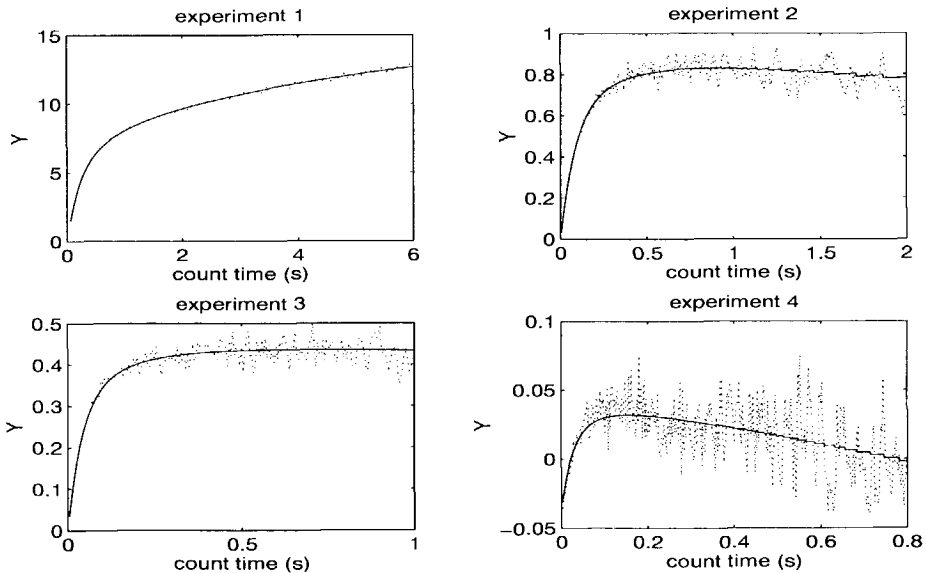


Figure 6.5 Feynman's variance-over-mean analysis. The solid line indicates the fit to the measurement (dotted line).

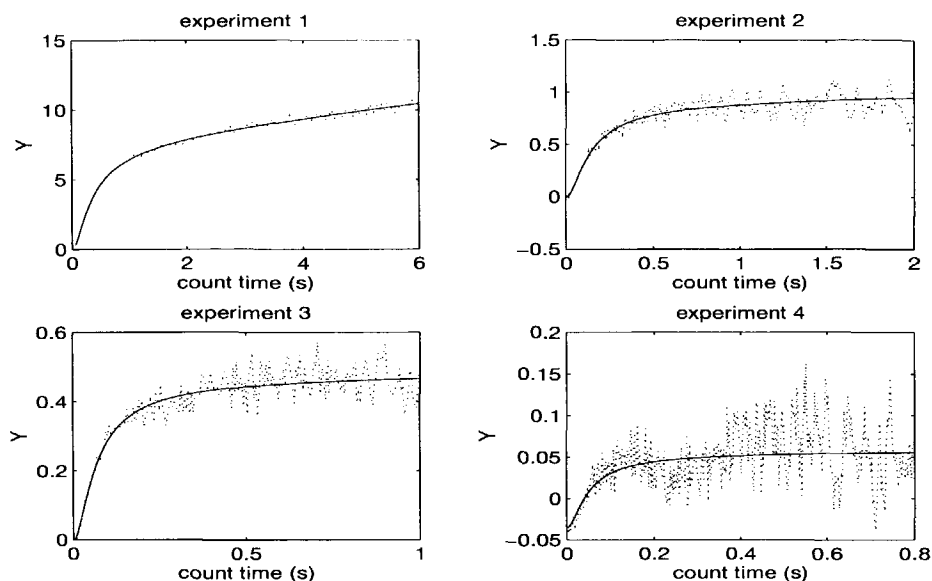


Figure 6.7 Bennet's δ -variance analysis. The solid line indicates the fit to the measurement (dotted line).

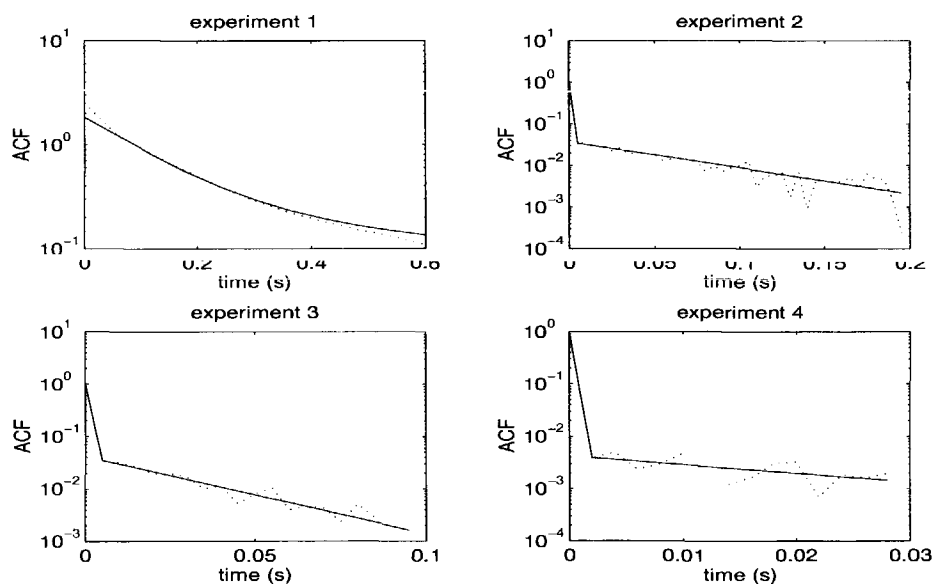


Figure 6.8 Auto-correlation analysis. The solid line indicates the fit to the measurement (dotted line).

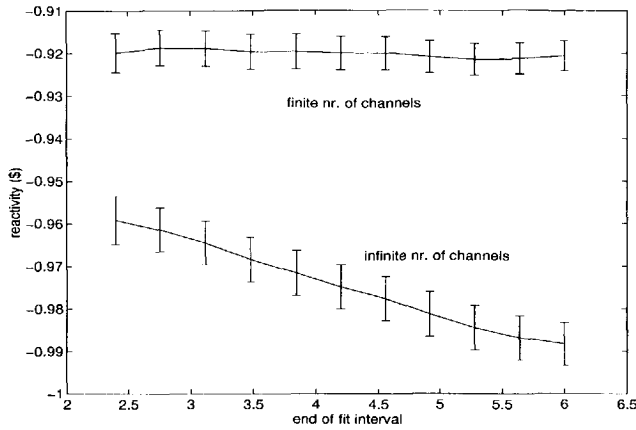


Figure 6.9 The fitted reactivity as a function of the length of the fit interval. The models with and without finite number of channels have been fitted to the variance-over-mean ratio of the neutron counts from detector 1 in experiment 1.

Table 6.5 summarises the results of all measurement techniques. The values in this table are displayed in figure 6.10. Recall that in experiment 1, the IK technique was not directly applied. The quoted value is derived from the rod calibration curve. In all cases the auto- and cross-correlation techniques are seen to lead to less accurate estimates of the reactivity than the variance techniques. Due to the poor statistical accuracy of the experimental noise quantities in experiment 4, it was very difficult to infer the reactivity. The length of the fit interval had to be limited in order to get meaningful results. Due to the small number of data points that were used for the fit, the inferred reactivity was seen to be rather sensitive to the length of the fit interval, and therefore, the results reported for experiment 4 should be considered with some caution.

Table 6.5 Inferred reactivity values (in dollars) per detector (\pm one standard deviation). Detector positions see tables 6.1 and 6.4. Between parentheses the reactivity from the IK method without applying the spatial correction factor.

| Method | experiment 1 (4 control rods) | experiment 2 (shutdown rod 7) | experiment 3 (shutdown rods 5+6) | experiment 4 (shutdown rods 5+6+7+8) |
|------------------------|--|--|--|--|
| IK | -0.843 \pm 0.004 | -3.22 \pm 0.02 -3.47 \pm 0.02 | -6.71 \pm 0.06 (-7.21 \pm 0.06) | -13.14 \pm 0.08 (-14.57 \pm 0.13) |
| PNS | -0.93 \pm 0.01 | -3.58 \pm 0.026 -3.56 \pm 0.026 | -7.48 \pm 0.05 | -15.5 \pm 0.11 |
| Feynman det.1 det.2 | -0.920 \pm 0.004 -0.925 \pm 0.004 | -3.68 \pm 0.041 -3.47 \pm 0.023 | -8.51 \pm 0.15 | -12.4 \pm 0.7 |
| Bennet det.1 det.2 | -0.910 \pm 0.006 -0.900 \pm 0.004 | -3.57 \pm 0.06 -3.48 \pm 0.03 | -8.33 \pm 0.22 | -11.0 \pm 0.8 |
| covariance | -0.924 \pm 0.004 | -3.585 \pm 0.022 | - | - |
| ACF det.1 det.2 | -0.890 \pm 0.017 -0.897 \pm 0.013 | -3.31 \pm 0.30 -3.54 \pm 0.10 | -7.65 \pm 0.69 | -7.6 \pm 2.3 |
| CCF | -0.92 \pm 0.013 | -3.58 \pm 0.18 | - | - |

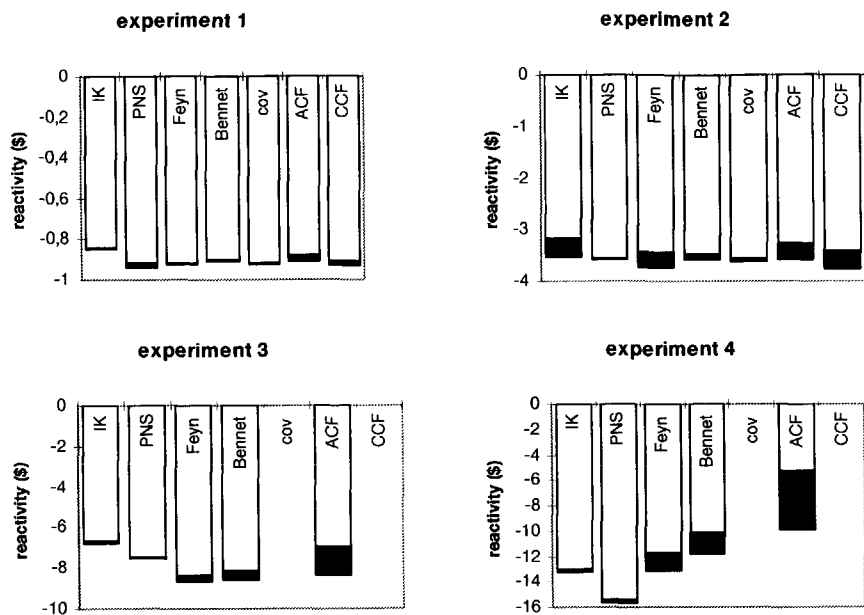


Figure 6.10 Illustration of the reactivities obtained with the various measurement techniques. The dark end of a bar indicates the (average) reactivity plus/minus one standard deviation.

6.2.4 Conclusions

It has been shown that in neutronically slow systems which are not too deeply subcritical, noise measurements can be successfully conducted. For instance in experiment 1, all measurement techniques except the IK, yield estimates of the reactivity which are in good agreement with each other. The fact that the IK result was derived indirectly and assuming that the presence of five extra detectors, among them three strong absorbers, might effect the reactivity worth of the fine control rods, lessens the discrepancy. Furthermore, experimental evidence was found for the finite measurement time effect predicted in chapter 2. The experiments indicate that variance techniques yield more accurate estimates of the reactivity than correlation functions.

The agreement between the various methods is seen to decrease with subcriticality. Especially in experiments 3 and 4, the application of the noise techniques is disappointing. In experiment 4, the use of the kinetic parameter calculated with the kinetic flux instead of the static flux would increase the absolute value of the reactivity by about 5.5% (compare the values of Λ^* in tables 6.2 and 6.3). Hence, the method of calculating this parameter does not solve the discrepancy. It is believed that better results can be obtained by increasing the total measurement time of the noise measurements significantly. Furthermore, the optimisation of the channel width could also contribute to the improvement of the accuracy of the fitted parameters.

The advantage of the IK method compared to the other techniques is that good results can be obtained within a short measurement time. Also, no special equipment is needed. However, observe that the result of the IK method depends directly on a calculated correction factor, which takes account of changes in the spatial distribution of the flux due to the insertion of one or more rods. Unfortunately, the application of the calculated correction factors in experiment 2 does not lead to a good agreement between the two detectors. Also, note that in experiments 3 and 4 the inferred reactivity without the application of the spatial correction factor is in better agreement with the PNS reactivity. A more detailed discussion about the correction factors and their application is postponed until section 6.5.

The advantage of the inhour method to analyse a PNS measurement is that the prompt decay constant is determined. This parameter is a global reactor parameter and hence does not depend on a calculated spatial correction factor. This is illustrated by the results of experiment 2, although it is recognised that more detectors are needed for a more convincing evidence. Whereas the correction factor applied in the IK in general becomes more important as the subcriticality increases, the delayed neutron background in PNS measurement reduces thus making the determination of the prompt decay constant easier. For this reason, the PNS results are considered to be the most reliable results in experiments 3 and 4. In general, the PNS technique is to be favoured in deep subcritical systems.

In subsequent sections the main goal is to use measured rod worths to verify the calculational methods. It is therefore preferred to use recognised measurement techniques which have been applied successfully before in similar systems. For this reason, only the use of PNS and IK techniques was considered. Because the available measurement time was limited, it was decided to adopt the IK technique as the standard technique to measure rod worths.

6.3 The reactivity worth of the auto-rod

6.3.1 Calculations

First-order perturbation theory was used to estimate the worth of the auto-rod, since its reactivity worth is small ($<0.1\%$). The reference state for the calculations was the fully inserted auto-rod, i.e. the worth is zero when the panel displays 0 mm. In order to compute the reactivity worth of a particular withdrawal, first the change in the amount of copper per unit length is calculated along the trajectory extending from the lower end of the fully inserted auto-rod (flush to the bottom of the system) to the upper end of the withdrawn auto-rod. This axial change in the amount of copper is multiplied by the spatial dependent reactivity worth of copper, and then integrated over the before mentioned trajectory. In formula:

$$r(x) = \int_0^{n(x)} \left(\frac{dm}{dz} \right) \Delta r_{cu}(z) dz \approx \sum_i \Delta m(z_i, z_{i+1}) \Delta r_{cu} \left(\frac{z_i + z_{i+1}}{2} \right) \quad (6.1)$$

where :

| | |
|--------|---|
| $r(x)$ | is the reactivity worth of the x mm withdrawn auto-rod |
| x | is the indication on the control panel (withdrawal in mm) |
| z | is the axial position |

- $\Delta m(z_i, z_{i+1})$ is the change in the amount of copper (in grams) between z_i and z_{i+1}
 $\Delta r_{cu}(z)$ is the reactivity worth per gram copper at a radius of 89 cm (calculated by PERT-V)
 $H(x)$ is the axial position of the upper end of the withdrawn auto-rod

6.3.2 Measurements

The worth of the auto-rod was determined by moving the auto-rod by hand control and meanwhile measuring the reactivity via the inverse kinetics technique. The other channel of the DSA-2 system was used to simultaneously measure the position of the auto-rod. In core 5 and 7, extra measurements were made with two neutron detectors, one in the radial centre, and the second one in the radial reflector (the linear channel of the nuclear instrumentation). The axial position of the first detector was chosen such that the signal was equal to that of the second detector. The results of both detectors were seen to agree within experimental uncertainty.

6.3.3 Results

The calculated and measured integral reactivity worths, i.e. the reactivity differences between the fully inserted and fully withdrawn states, can be found in table 6.6 below. It is seen that both the calculations with streaming correction and without streaming correction overestimate the worth by about 18% on average. Considering the steep gradient of the flux and the simplifications in the calculation of the rod worth, this difference between measurement and calculation is acceptable. The ratio of the worths calculated with and without streaming correction is seen to increase with the amount of moderation in the core from 0.953 in core 5 to 1.049 in core 7.

Table 6.6 The integral worth of the auto-rod in dollarcents. In core 7, $1\$=727$ pcm, in the other cores $1\$=720$ pcm.

| | core 5 | core 7 | core 9 | core 10 |
|-----------|-----------------|-----------------|-----------------|------------------|
| $E^{(1)}$ | 9.24 ± 0.08 | 5.73 ± 0.08 | 9.18 ± 0.06 | 6.96 ± 0.044 |
| $C^{(2)}$ | 10.375 | 6.867 | 10.282 | 8.867 |
| (C/E) | (1.123) | (1.198) | (1.120) | (1.274) |
| $C^{(3)}$ | 10.898 | 6.545 | 10.737 | 8.641 |
| (C/E) | (1.179) | (1.142) | (1.170) | (1.242) |

(1) experiment

(2) calculation with streaming correction in core region

(3) calculation without streaming correction in core region

In order to compare the computed to the measured rod-calibration curves (i.e. the auto-rod worth as a function of the withdrawal), both the computed and the measured integral worths were normalised to unity. The results are shown in figure 6.11. This figure shows that the curves are well predicted by the calculations. It turned out that these curves can be represented well by a third-order polynomial. Subsequently, the differential rod worth is estimated by differentiating the fitted third-order polynomials, see figure 6.12. From this figure, it can be concluded that the calibration curves tend more to linearity as the core height decreases. This could be expected since the auto-rod was designed for an one meter high core.

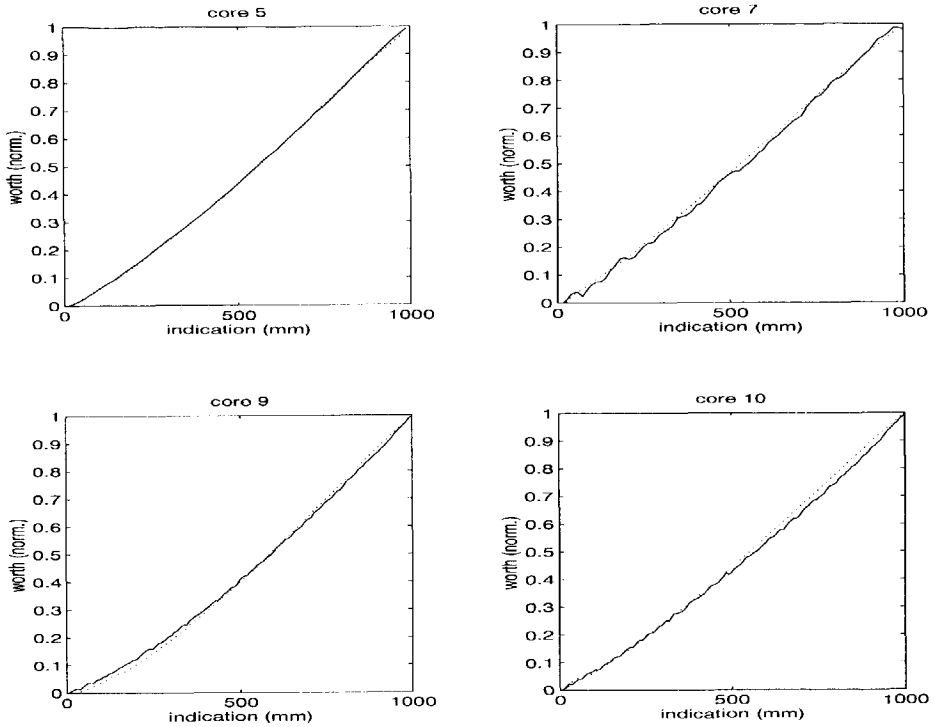


Figure 6.11 The normalised worth of the auto-rod as a function of the indication on the instrumentation panel. The solid lines indicate the measured curves, the dotted lines the calculated curves.

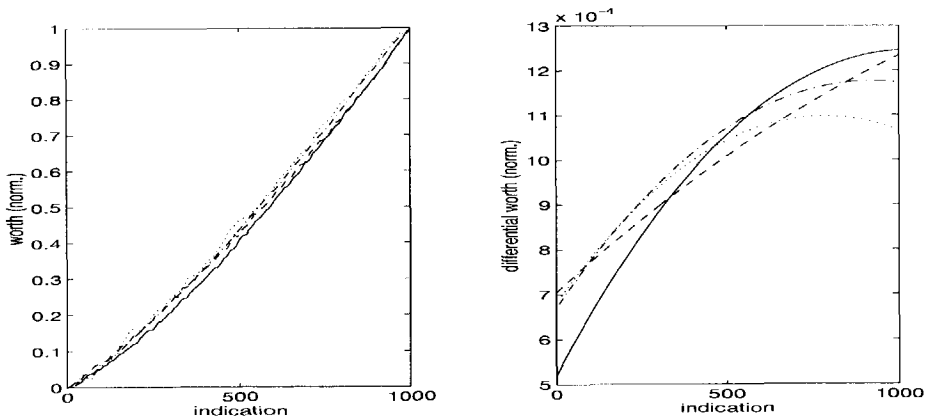


Figure 6.12 The worth (left) and the differential worth (right) as function of the indication on the instrumentation panel. The dotted line indicates the worth in core 7, the dash-dotted line in core 5, the dashed line in core 10, and the solid line core 9.

Due to the wedge-shape of the auto-rod, the amount of displaced rod-material in the region from the lower tip of the withdrawn rod to the upper end of the fully inserted rod, is proportional to the distance that the rod is withdrawn. If this would be the only contribution to the rod worth, the calibration curve would be linear. However, also the displacement of rod material below and above this region contribute to the rod worth, as a result of which the calibration curve becomes non-linear. The lower the core height, the smaller the contribution from these outer regions, and hence, the calibration curve tends more to linearity.

6.4 The reactivity worth of the fine control rods

6.4.1 Calculations

Use was made of a three-dimensional BOLD-VENTURE model in X-Y-Z geometry to calculate the reactivity worth of a fine control rod. An auxiliary code has been written which generates the geometric input data for the X-Y-Z model based on a given R-Z model and specified mesh sizes in the various zones. Additionally, rods and channels can be specified. The rod worth was calculated for nine different insertion depths. In order to limit the relatively large amount of time that is needed for the input and output to temporary files, the number of energy groups was limited to four. New values of the diffusion coefficient modifiers (introduced in section 4.4) were determined that yielded the same reduction in k_{eff} as determined with KENO-Va.

The reactivity worth of the (partial) insertion of a control rod is calculated via

$$|\Delta\rho| = \frac{k_1 - k_2}{k_1 k_2} \quad (6.2)$$

where k_1 is the multiplication constant of the system with the rod fully withdrawn and k_2 the multiplication constant of the system with the rod inserted. As the integral worth of a single control rod varies between 20 and 40 dollarcent, the use of KENO was not considered because of the limited attainable statistical accuracy. However, the bank worth (the worth of all four rods together) can be calculated with an acceptable accuracy. Also BOLD-VENTURE was used to compute the bank worth. A comparison to the single rod worth enables the investigation of possible interactions between the control rods.

6.4.2 Measurements

The inverse kinetics technique was selected as the standard technique to measure the worth of the fine control rods. Two experimental approaches were tested:

1. The reactor was in a critical state with the rod of interest completely inserted. Then, the rod was completely withdrawn in a few (typically three or four) steps. After each step, the reactor was made critical with the other rods. The positive reactivity of each step was determined with the inverse kinetics equation and the stable reactor period technique.
2. The reactor was in a critical state with the rod of interest completely withdrawn. Then, the rod was driven in completely, which takes 156 s. The reactivity was determined via the inverse kinetics equation.

With the first approach, only the integral worth is obtained, whereas with the second approach both the integral worth and the differential rod worth can be obtained. In core 5, only the first approach was used. In core 7, both approaches were applied, whereas in cores 9 and 10 only the second approach was used. Normally, two detectors were used, one located in the radial centre, the other in the radial reflector.

6.4.3 Results

The results of the stable period and the inverse kinetics technique for the positive reactivity steps were seen to agree within 0.7%. Recall, that both methods use the same experimental data. The comparison to the results of the second approach (an independent measurement) showed that they agreed within 1.7%. Hence, all results agree within two standard deviations and therefore only the average of all techniques (and detectors) is shown in table 6.7. In this table it can be seen that the rod worths of rods 2 and 3 are slightly lower than those of rods 1 and 4. This is attributed to the presence of the auto-rod. For this reason, the average of rods 1 and 4 was used as reference for the calculated values.

Table 6.7 The integral worth of the control rods in dollarcents. In core 7, $1\$/=727$ pcm, in the other cores $1\$/=720$ pcm.

| | core 5 | core 7 | core 9 | core 10 |
|---------------------|------------------|-------------------|------------------|-------------------|
| rod 1 | - | 21.76 ± 0.030 | 39.69 ± 0.09 | 28.19 ± 0.070 |
| rod 2 | 35.54 ± 0.04 | 21.69 ± 0.031 | 39.04 ± 0.09 | 27.85 ± 0.084 |
| rod 3 | - | 21.60 ± 0.040 | 39.07 ± 0.09 | 27.64 ± 0.074 |
| rod 4 | 36.03 ± 0.04 | 22.02 ± 0.046 | 39.61 ± 0.09 | 28.15 ± 0.071 |
| $E^{(1)}$ | 36.03 ± 0.04 | 21.84 ± 0.12 | 36.65 ± 0.04 | 28.17 ± 0.05 |
| B.V. ⁽²⁾ | 43.3 | 26.6 | 31.6 | 25.4 |
| (C/E) | (1.202) | (1.218) | (0.862) | (0.902) |

⁽¹⁾ average of rod 1 and 4

⁽²⁾ Bold Venture calculation

The bank worth of the four control rods can be found in table 6.8. It can be seen that according to the BOLD VENTURE calculations, there is no significant interaction between the rods. The difference between these calculated and measured rod worths is acceptable considering the approximations in the modelling of the system. Recall that the thermal flux gradient is quite large at the radial position of the control rods, which requires a detailed modelling of the rods for accurate results. Of course, KENO offers this possibility, and indeed, in general a better agreement with the measured results is obtained.

Table 6.8 The bank worth of the fine control rods in dollarcents.

| | core 5 | core 7 | core 9 | core 10 |
|----------------|--------------|-------------------|---------------------|-------------------|
| $E^{(1)}$ | - | 87.07 ± 0.075 | 157.41 ± 0.18 | 111.83 ± 0.15 |
| B.V. 4 x 1 rod | 173.2 | 106.4 | 126.4 | 101.6 |
| B.V. 4 rods | 175.1 | 108.6 | 127.1 | 101.7 |
| (C/E) | (-) | (1.247) | (0.807) | (0.909) |
| KENO | 148 ± 11 | 83 ± 10 | 148 ± 11 | 143 ± 12 |
| (C/E) | (-) | (0.95 \pm 0.12) | (0.940 \pm 0.070) | (1.28 \pm 0.11) |

⁽¹⁾ The sum of the measured rod worths in table 6.8

Identical to the procedure followed for the auto-rod, the calibration curves were normalised to unity for comparison to the calculated curves. It turned out that the normalised calibration curves of the individual rods in a core configuration, were practically identical. They are shown in figure 6.13 along with the calculated points. Although it is difficult to compute the absolute worth of the rods, it is seen that the functional dependence of the calibration curve can be predicted accurately.

In order to compute the differential rod worth, a high-order polynomial was fitted to the measured calibration curve. Since in core 5 the calibration curve was not measured, a polynomial was fitted to the calculated points. It turned out that this fitted polynomial has a local maximum at an indication of 164 mm, which is non-physical. For this reason, a 2nd-order polynomial of the form ax^2 is used for indications up to several hundred mm. Hence, the (normalised) calibration curve in core 5 is represented by:

$$\begin{aligned} 0 \leq x \leq B & \quad r(x) = ax^2 \\ B \leq x \leq 2500 & \quad r(x) = \sum_{n=0}^N b_n x^n \end{aligned} \quad (6.3)$$

For given coefficients b_n the parameter a can be calculated by requiring that the function $r(x)$ is continuous at the boundary B . The value of B was chosen by minimising the difference between the first derivatives of the two polynomials at the boundary. The differential worths, which were derived from the fitted polynomials, are also shown in figure 6.13. The vertical lines denote the indications which correspond to control rods withdrawn to the top of the core. The left-most vertical solid line denotes the indication corresponding to a rod withdrawn to the upper end of the cavity.

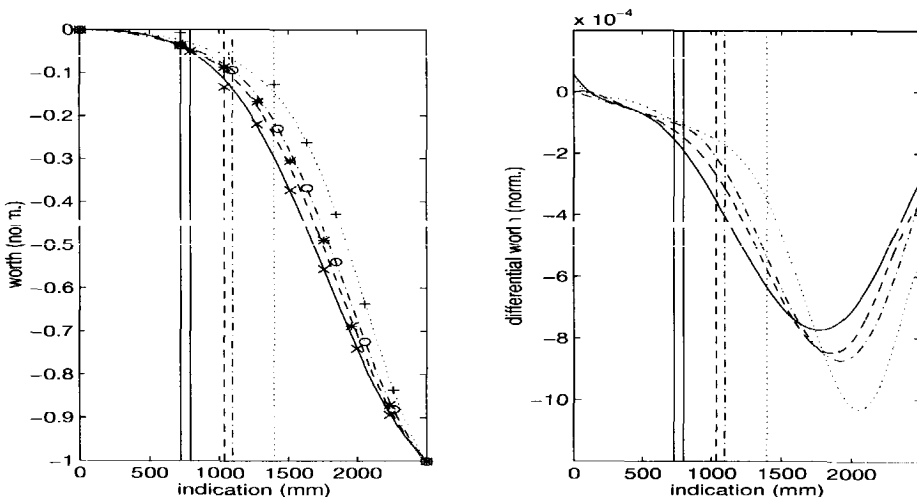


Figure 6.13 The normalised worth (left) and differential worth (right) as a function of the indication on the instrumentation panel. The dotted line indicates the measured calibration curve in core 7, the dashed line in core 10, and the solid line core 9. The dash-dotted line represents the polynomial fitted to the calculated points 'o' for core 5. The '+' represent the calculated points for core 7, the 'x' the points for core 9, and the '*' the points for core 10.

6.5 The reactivity worth of the shutdown rods

6.5.1 Calculation of the rod worth

The worths of single shutdown rods and of several combinations of two or more rods, have been calculated with KENO. The absolute reactivity worth, which was calculated via Eq. (6.2), was converted to the dollar unit using $\beta_{\text{eff}} = 727$ pcm for core 7 and $\beta_{\text{eff}} = 720$ pcm for the other cores. The obtained rod worths can be found in table 6.9 below.

Table 6.9 The worth (in dollars) of the safety/shutdown rods as calculated with KENO.

| rods inserted | core 5 | core 7 | core 9 | core 10 |
|-----------------|------------|------------|------------|------------|
| 1 | 3.43±0.10 | 2.31±0.07 | 3.62±0.10 | 2.84±0.12 |
| 2 | 3.50±0.14 | 2.14±0.08 | 3.75±0.10 | 2.90±0.12 |
| 3 | 3.39±0.11 | 2.32±0.10 | 3.63±0.10 | 2.99±0.12 |
| 4 | 3.47±0.09 | 2.29±0.10 | 3.63±0.10 | 2.85±0.12 |
| 1+2 | 7.17±0.10 | 4.69±0.10 | 7.64±0.10 | 5.72±0.12 |
| 1+3 | 7.06±0.10 | 4.46±0.10 | 7.42±0.10 | 5.18±0.12 |
| 3+4 | 7.44±0.10 | 4.73±0.10 | 7.58±0.10 | 5.80±0.12 |
| 1+2+3 | 11.24±0.10 | 6.90±0.10 | 11.70±0.10 | 8.75±0.13 |
| 2+3+4 | 11.16±0.10 | 6.96±0.10 | 11.78±0.10 | 8.44±0.13 |
| 1+2+3+4 | 15.57±0.13 | 9.42±0.10 | 16.43±0.10 | 11.81±0.14 |
| 1+2+3+4+5+6+7+8 | 32.21±0.15 | 18.07±0.11 | 33.97±0.10 | 23.32±0.13 |

The rod worths were also obtained from 2D transport theory calculations in R- θ geometry, which were primarily performed to obtain the spatial correction factors for the inverse kinetics measurements. For this reason, the details of these computations can be found in section 6.5.3. The rod worths are listed in table 6.10, and are seen to be smaller than the worths as calculated by KENO, in particular the rod worths in core 7. This is probably due to the fact that in the transport theory calculations, no streaming correction is applied in the core region.

Table 6.10 The worth (in dollars) of the safety/shutdown rods as calculated with the 2D transport theory code DORT. Between parentheses the ratio to the corresponding worth calculated by KENO.

| rods inserted | core 5 | core 7 | core 9 | core 10 |
|---------------|---------------|--------------|---------------|---------------|
| 5 | 3.26 (0.946) | 1.74 (0.770) | 3.49 (0.955) | 2.52 (0.870) |
| 6 | 3.22 (0.934) | 1.72 (0.761) | 3.45 (0.944) | 2.53 (0.874) |
| 7 | 3.24 (0.940) | 1.73 (0.765) | 3.48 (0.952) | 2.54 (0.877) |
| 8 | 3.39 (0.984) | 1.74 (0.770) | 3.53 (0.966) | 2.47 (0.853) |
| 5+6 | 6.89 (0.943) | - | 7.38 (0.970) | 5.35 (0.929) |
| 5+7 | 6.65 (0.942) | - | 7.14 (0.962) | 5.15 (0.994) |
| 5+8 | 6.72 (0.952) | - | 7.20 (0.970) | 5.21 (1.006) |
| 5+6+7+8 | 14.70 (0.944) | 7.50 (0.796) | 15.75 (0.959) | 11.21 (0.949) |

6.5.2 Measurement of the rod worth

The inverse kinetics technique was chosen as the standard technique to measure the rod worths. Measurements were made with at least two detectors: that of the standard linear channel (detector 2), the azimuthal position of which is indicated in figure 6.1, and a detector in the radial centre (detector 1). Usually, the axial position of this detector was chosen such that its signal value equals that of the standard linear channel. Table 6.11 gives an overview of the detector positions.

Table 6.11 Overview of the detector positions in the core configurations. The position is indicated by the radius (cm), the angle relative to the positive x-direction in anti-clockwise direction (degrees), and the axial position (cm) above the base of the system.

| core | det. 1 R,θ,Z | det. 2 R,θ,Z | det. 3 R,θ,Z |
|------|-----------------|-----------------|-----------------|
| 5 | 0, -, 275 | 127, 315, 157 | 127, 45, 157 |
| 7 | 0, -, 256 | 127, 315, 157 | 127, 45, 157 |
| 9 | 0, -, 297 | 127, 315, 157 | - |
| 10 | 0, -, 298 | 127, 315, 157 | 127, 225, 207 |

For the measurements in cores 5, 7, and 9, only the DSA-2 system was available which limited the maximum sampling frequency to 4 Hz. In fact, this sampling frequency is rather low compared to the change in the detector signal due to the insertion of one or more shutdown rods (drop time < 1.2 s). In core 10, the new data-acquisition software allowed higher sampling frequencies. In order to investigate the effect of the sampling frequency on the derived rod worth, the worth of shutdown rod 8 was measured with frequencies varying from 2 to 16 Hz. Figure 6.14 shows that the worth of the shutdown rod measured with a sampling frequency of 4 Hz is always slightly lower than the worth measured with a sampling frequency of 16 Hz, although the rod worths still agree within the statistical uncertainty. This statistical uncertainty is the square root of the sum of the variances in the reactivity before and after the rod drop, and hence, does not include the uncertainty due to the uncertainties in the delayed neutron parameters.

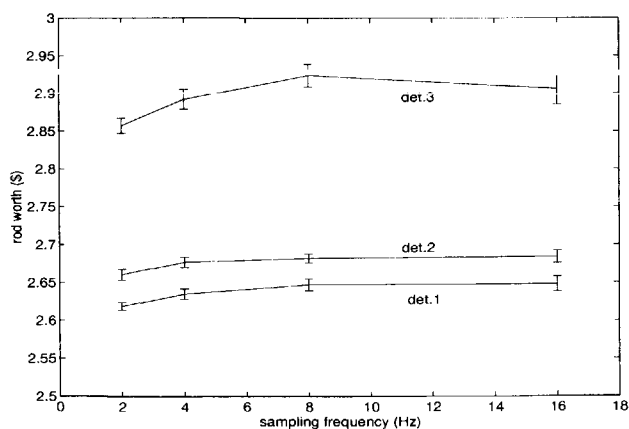


Figure 6.14 The effect of the sampling frequency on the derived worth of shutdown rod 8 in core 10.

Figure 6.14 also shows the need for the spatial correction factors. The calculation of this correction factor is the subject of the next section.

6.5.3 Calculation of correction factors

In order to compute the spatial correction factor $A(r,t)$, which is defined by Eq. (2.17) in section 2.2.1, use was made of a DORT R- θ model which is based upon an input description from A. Ziver of PSI. His input model is a conversion of the TWODANT input model developed by D. Mathews of PSI, which is described in detail elsewhere [7]. However, in some respects the applied DORT model differs from Mathews' TWODANT model:

1. an S_4 angular quadrature set was used
2. in the θ direction periodic boundary conditions were used
3. the P_1 scattering matrices were not modified
4. $\theta = 0$ was placed between shutdown rods 1 and 7, i.e. rod 1 is at an angle of 25.3125 degrees, and rod 7 at an angle of 334.6875 degrees.

The axial neutron leakage in R- θ geometry is taken into account via a $DB^2\phi$ term [10]. The energy- and space-dependent DB^2 -values were obtained from R-Z DORT calculations. Eleven radial regions were defined, each the height of the core region, which correspond to the eleven regions in the radial direction in the R- θ model. Per region and per energy group, the DB^2 values were obtained by dividing the total net leakage in the axial direction by the neutron flux integrated over the region volume, which are both specified in the region-wise neutron balance tables in the output of DORT. The DB^2 values for the region containing the safety and shutdown rods were set to zero, also for the unrodded cases.

Whereas TWODANT is reported to be completely unstable with periodic boundary conditions in the θ direction [7], the flux computed by DORT converges to below 10^{-4} in about 20 cpu minutes on a DEC- α computer of the IRI. The k_{eff} values for both the R-Z and R- θ calculations can be found in table 6.12 below.

Table 6.12 The k_{eff} values for the (P_3, S_{16}) R-Z and the (P_1, S_4) R- θ DORT calculations.

| geometry | core 5 | core 7 | core 9 | core 10 |
|-------------|---------|---------|---------|---------|
| R-Z | 1.03148 | 1.03837 | 1.03094 | 1.03367 |
| R- θ | 1.03669 | 1.04045 | 1.03432 | 1.03566 |

The converged flux distributions for the rodded and unrodded configurations are multiplied by the absorption cross-section of ^{10}B , and then the correction surface $A(r,t)$ is computed by dividing the unrodded ^{10}B absorption rate distribution by the rodded ^{10}B absorption rate distribution. In fact two correction surfaces are calculated: the first surface is based upon ^{10}B cross sections averaged over the core region neutron spectrum (for a detector located in the core region), and the second is based on ^{10}B cross sections averaged over the softer reflector neutron spectrum (for detectors located in the reflector). The shapes of both surfaces are practically identical. Figure 6.15 shows the correction surface in core 5 for one shutdown rod inserted, two rods at about 90 degrees (rods 5 and 7), two rods at about 180 degrees (rods 5 and 6), and four rods. The correction surfaces in the other configurations have similar shapes. For display purposes, the peaks at the position of the inserted rod(s) is limited to 2.5.

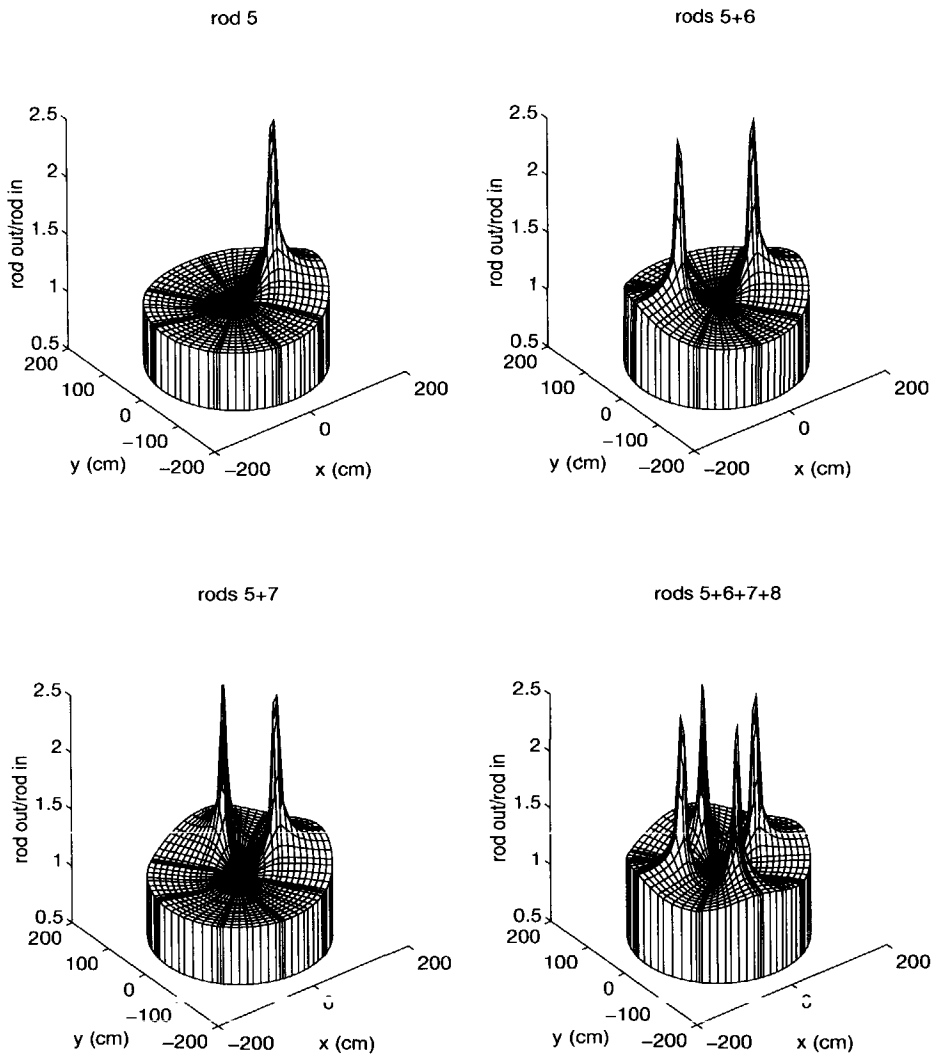


Figure 6.15 The spatial correction surface for insertion of rod 5, rods 5+6 (at ~ 180 degrees), rods 5+7 (at ~ 90 degrees), and rods 5+6+7+8.

The spatial correction factors for the detectors are assumed to be the values of the correction surfaces at the positions indicated in table 6.11, i.e. the size of the detectors is not taken into account. This also implies that the detector is not assumed to affect the flux distribution, which is, considering the size and neutron sensitivity of the detectors, questionable. Furthermore, the assumption is made that the axial detector position has no effect on the spatial correction factor. In fact, the R- θ calculations are characteristic of an axial plane in the centre of the core region. Hence, for the detector in the radial centre (detector 1 in table 6.11), which is always located in the cavity or in the upper axial reflector, separate calculation should be performed. A full three-dimensional presentation of the system (including the large

detectors) would be even more preferable. Due to time restrictions, this was not possible. The resulting spatial correction factors can be found in tables 6.13 to 6.16.

The second correction factor $B(t)$ takes account of the change in the energy distribution due to the insertion of one or more shutdown rods, see Eq. (2.21). In chapter 3 the calculation of the generation time Λ and the weighted neutron production F , which both appear in the definition of $B(t)$, is discussed in detail. As far as the calculation of the generation time is concerned, Williams [8] has shown that even a single inserted shutdown rod may be represented by a grey curtain in an R-Z model. Therefore, in the R-Z model that was used to compute the generation time at critical (see chapter 3), the ^{10}B density in an annular region in the reflector is increased until k_{eff} corresponds to the (uncorrected) measured value, and then the adjoint function is calculated.

Tables 6.13 to 6.16 list the correction factors $A(r,t)$ and $B(t)$ for the various detectors and subcriticalities in the four core configurations. Recall from chapter 2 that the values listed must be applied after the rod-drop. Before the rod-drop both $A(r,t)$ and $B(t)$ equal unity. As the factor $B(t)$ does not vary significantly with subcriticality, as can be seen in the tables, it has only been calculated for one, two and for four inserted rods per core and not for each individual rod or combination of rods. As a rule of thumb, it may be assumed that due to the correction AB after the rod drop, the rod worth obtained without any correction is increased by a factor of $1/AB$. As an illustration, the worth of shutdown rod 8 in core 10 (see also figure 6.14) is determined with and without correction factor, see figure 6.16. Without correction, the maximum (relative) difference between the reactivities measured with the three detectors amounts 9.7%. Due to the correction factors, the maximum difference is reduced to 6.3%. If only detectors 2 and 3 are considered, which axial positions are within the core region, the difference is seen to be reduced from 8.3% to 2.0%.

Table 6.13 Correction factors for inverse kinetics in core 5 (detector positions see table 6.11)

| rods inserted | detector 1 | | | detector 2 | | | detector 3 | | |
|---------------|------------|--------|--------|------------|--------|--------|------------|--------|--------|
| | A(r,t) | B(t) | AB | A(r,t) | B(t) | AB | A(r,t) | B(t) | AB |
| 5 | 1.0064 | 0.9962 | 1.0026 | 1.0969 | 0.9962 | 1.0928 | 1.0376 | 0.9962 | 1.0337 |
| 6 | 1.0061 | 0.9962 | 1.0023 | 0.9899 | 0.9962 | 0.9862 | 0.9978 | 0.9962 | 0.9940 |
| 7 | 1.0063 | 0.9962 | 1.0025 | 1.0071 | 0.9962 | 1.0033 | 1.0900 | 0.9962 | 1.0859 |
| 8 | 1.0068 | 0.9962 | 1.0030 | 1.0312 | 0.9962 | 1.0273 | 0.9978 | 0.9962 | 0.9940 |
| 5+6 | 1.0129 | 0.9916 | 1.0044 | 1.0896 | 0.9916 | 1.0805 | 1.0338 | 0.9916 | 1.0251 |
| 5+7 | 1.0126 | 0.9916 | 1.0041 | 1.0970 | 0.9916 | 1.0878 | 1.1659 | 0.9916 | 1.1561 |
| 5-8 | 1.0261 | 0.9832 | 1.0089 | 1.1319 | 0.9832 | 1.1129 | 1.1504 | 0.9832 | 1.1311 |

Table 6.14 Correction factors for inverse kinetics in core 7 (detector positions see table 6.11)

| rods inserted | detector 1 | | | detector 2 | | | detector 3 | | |
|---------------|------------|--------|--------|------------|--------|--------|------------|--------|--------|
| | A(r,t) | B(t) | AB | A(r,t) | B(t) | AB | A(r,t) | B(t) | AB |
| 5 | 0.9965 | 0.9848 | 0.9814 | 1.0935 | 0.9848 | 1.0769 | 1.0366 | 0.9848 | 1.0209 |
| 6 | 0.9964 | 0.9848 | 0.9813 | 0.9943 | 0.9848 | 0.9792 | 0.9969 | 0.9848 | 0.9818 |
| 7 | 0.9964 | 0.9848 | 0.9813 | 1.0110 | 0.9848 | 0.9957 | 1.0767 | 0.9848 | 1.0604 |
| 8 | 0.9968 | 0.9848 | 0.9817 | 1.0380 | 0.9848 | 1.0223 | 0.9940 | 0.9848 | 0.9789 |
| 5-8 | 0.9842 | 0.9240 | 0.9094 | 1.1338 | 0.9240 | 1.0476 | 1.1518 | 0.9240 | 1.0642 |

Table 6.15 Correction factors for inverse kinetics in core 9 (detector positions see table 6.11)

| rods inserted | detector 1 | | | detector 2 | | |
|---------------|------------|--------|--------|------------|--------|--------|
| | A(r,t) | B(t) | AB | A(r,t) | B(t) | AB |
| 5 | 1.0090 | 0.9979 | 1.0069 | 1.1020 | 0.9979 | 1.0997 |
| 6 | 1.0087 | 0.9979 | 1.0066 | 0.9925 | 0.9979 | 0.9904 |
| 7 | 1.0089 | 0.9979 | 1.0068 | 1.0100 | 0.9979 | 1.0079 |
| 8 | 1.0094 | 0.9979 | 1.0073 | 1.0312 | 0.9979 | 1.0290 |
| 5+6 | 1.0184 | 0.9962 | 1.0145 | 1.0943 | 0.9962 | 1.0901 |
| 5+7 | 1.0180 | 0.9962 | 1.0141 | - | - | - |
| 5+8 | 1.0185 | 0.9962 | 1.0146 | - | - | - |
| 5-8 | 1.0377 | 0.9930 | 1.0305 | - | - | - |

Table 6.16 Correction factors for inverse kinetics in core 10 (detector positions see table 6.11)

| rods inserted | detector 1 | | | detector 2 | | | detector 3 | | |
|---------------|------------|--------|--------|------------|--------|--------|------------|--------|--------|
| | A(r,t) | B(t) | AB | A(r,t) | B(t) | AB | A(r,t) | B(t) | AB |
| 5 | 1.0020 | 0.9907 | 0.9927 | 1.1143 | 0.9907 | 1.1039 | 0.9908 | 0.9907 | 0.9816 |
| 6 | 1.0019 | 0.9907 | 0.9926 | 0.9914 | 0.9907 | 0.9822 | 1.0427 | 0.9907 | 1.0330 |
| 7 | 1.0020 | 0.9907 | 0.9927 | 1.0067 | 0.9907 | 0.9973 | 1.0023 | 0.9907 | 0.9930 |
| 8 | 1.0023 | 0.9907 | 0.9930 | 1.0591 | 0.9907 | 1.0492 | 1.1696 | 0.9907 | 1.1587 |
| 5+6 | 1.0038 | 0.9801 | 0.9938 | 1.0934 | 0.9801 | 1.0716 | 1.0328 | 0.9801 | 1.0122 |
| 5+7 | 1.0038 | 0.9801 | 0.9938 | 1.0978 | 0.9801 | 1.0759 | 0.9887 | 0.9801 | 0.9690 |
| 5+8 | 1.0042 | 0.9801 | 0.9942 | 1.1631 | 0.9801 | 1.1399 | 1.1005 | 0.9801 | 1.0786 |
| 5-8 | 1.0074 | 0.9567 | 0.9638 | 1.1401 | 0.9567 | 1.0907 | 1.1353 | 0.9567 | 1.0861 |

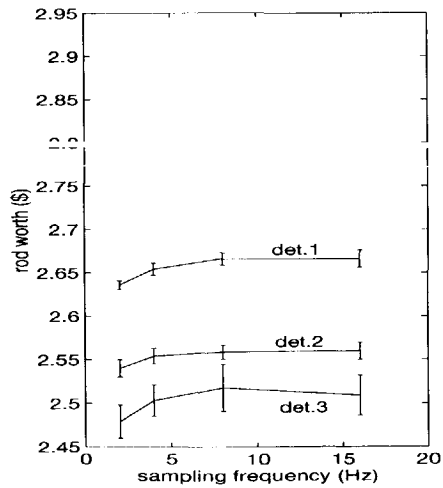
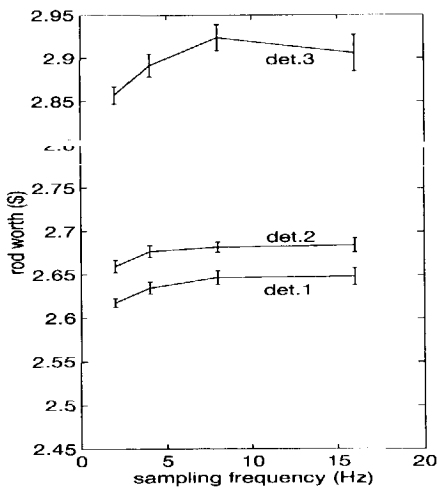


Figure 6.16 The worth of shutdown rod 8 in core 10 determined without (left) and with (right) applying the calculated correction factors.

6.5.4 Results

The measured rod worths (corrected for spatial dependence and neutron spectrum change) can be found in tables 6.17 to 6.20 (for detector positions see table 6.11). Despite the correction factors, the results obtained with the various detectors do not agree within the statistical uncertainty. In cores 5 and 7, the single rod worths agree within 10%, whereas the maximum difference in the bank-worth of the shutdown rods amounts 21%. The results obtained with detector 2 (the standard linear channel) in core 9 are suspiciously higher than the results obtained with detector 1. This was also observed during the analysis of the fine control rod measurements, and therefore, these results are not taken into account. Also in core 10, the rod worths obtained with detector 2 are higher than those obtained with the other two detectors, but in a lesser extent than in core 9. Except for rod 8, the maximum difference occurs always between detectors 2 and 3 with differences varying between 6 and 18%, whereas the difference between detectors 1 and 3 is seen to vary between 1 and 9%.

Table 6.17 Measured shutdown rod worths (in dollars) in core 5

| rods inserted | det. 1 | det. 2 | det. 3 | weighted average |
|---------------|------------|------------|-----------|------------------|
| 5 | 3.55±0.04 | 3.31±0.03 | 3.43±0.07 | 3.40±0.08 |
| 6 | 3.43±0.02 | 3.23±0.04 | 3.33±0.03 | 3.37±0.05 |
| 7 | 3.49±0.02 | 3.32±0.06 | - | 3.47±0.05 |
| 8 | 3.38±0.05 | 3.31±0.06 | - | 3.35±0.04 |
| 5+6 | - | 6.71±0.06 | - | 6.71±0.06 |
| 5+7 | - | 6.44±0.04 | - | 6.44±0.04 |
| 5+6+7+8 | 15.93±0.36 | 13.14±0.08 | - | 13.27±0.59 |

Table 6.18 Measured shutdown rod worths (in dollars) in core 7

| rods inserted | det. 1 | det. 2 | det. 3 | weighted average |
|---------------|------------|------------|------------|------------------|
| 5 | 2.22±0.060 | 2.11±0.010 | 2.16±0.025 | 2.13±0.013 |
| 6 | 2.23±0.087 | 2.04±0.027 | 2.18±0.011 | 2.10±0.033 |
| 7 | 2.22±0.025 | 2.02±0.016 | 2.33±0.017 | 2.08±0.053 |
| 8 | 2.16±0.043 | 2.03±0.023 | 2.09±0.013 | 2.06±0.019 |
| 5+6+7+8 | 10.74±0.09 | 8.82±0.11 | 9.23±0.11 | 9.70±0.50 |

Table 6.19 Measured shutdown rod worths (in dollars) in core 9

| rods inserted | det. 1 | det. 2 |
|---------------|-------------|-------------|
| 5 | 3.558±0.008 | 4.880±0.040 |
| 6 | 3.594±0.005 | 4.185±0.019 |
| 7 | 3.578±0.006 | 4.040±0.016 |
| 8 | 3.482±0.007 | - |
| 5+6 | 7.48±0.013 | 8.71±0.042 |
| 5+7 | 7.19±0.017 | - |
| 5+8 | 7.15±0.019 | - |
| 5+6+7+8 | 15.25±0.050 | - |

Table 6.20 Measured shutdown rod worths (in dollars) in core

| rods inserted | det. 1 | det. 2 | det. 3 | weighted average |
|---------------|-------------|-------------|-------------|------------------|
| 5 | 2.72±0.006 | 3.10±0.010 | 2.63±0.007 | 2.75±0.12 |
| 6 | 2.74±0.007 | 2.92±0.010 | 2.71±0.009 | 2.77±0.06 |
| 7 | 2.73±0.049 | 2.92±0.010 | 2.60±0.009 | 2.74±0.09 |
| 8 | 2.67±0.008 | 2.56±0.010 | 2.51±0.026 | 2.62±0.04 |
| 5+6 | 5.79±0.012 | 6.43±0.028 | 5.52±0.015 | 5.76±0.18 |
| 5+7 | 5.65±0.015 | 6.17±0.021 | 5.26±0.012 | 5.54±0.23 |
| 5+8 | 5.59±0.013 | 6.25±0.022 | 5.35±0.017 | 5.64±0.22 |
| 5+6+7+8 | 12.63±0.025 | 12.93±0.066 | 11.57±0.045 | 12.43±0.32 |

In order to compare the calculated rod worths to the measured worths, the average of the individual rod worths is taken, as well as of those combinations which have the same relative positions, see table 6.21. Except for the bank-worth of the shutdown rods in core 5, all calculated and measured worths agree within 10%. Note that the calculated bank-worth in core 5 agrees within 2.3% with the worth obtained with detector 1.

Interaction between rods results in a change in the worth of one or more rods due to the insertion of other rods, i.e. $\text{worth}(N \text{ rods}) \neq N \times \text{worth}(1 \text{ rod})$, and has been observed before [5]. Also in the studied configurations, interactions between shutdown rods are observed. Figure 6.17 shows the worth per rod inserted as a function of the number of rods inserted. The measurements indicate that in all configurations the worth per rod increases as more rods are inserted. In cores 5 and 7, the measured bank worth is about 15% higher than the sum of the individual shutdown rods, in core 9 7%, and in core 10 16%. This increase in rod worth is also predicted by the calculations for cores 5 and 9: the bank worth is 13% and 12.4% higher than the sum of the individual rod worths, respectively.

Table 6.21 The average worth of 1, 2 or 4 inserted rods as calculated by KENO and as measured (in dollars¹). The third number in a row is the ratio between calculation and experiment.

| # rods inserted | | core 5 | core 7 | core 9 | core 10 |
|------------------|----------------|-------------|-------------|-------------|-------------|
| 1 | C ² | 3.445±0.053 | 2.261±0.044 | 3.654±0.056 | 2.895±0.060 |
| | E ³ | 3.39±0.03 | 2.11±0.02 | 3.56±0.02 | 2.68±0.04 |
| | C/E | 1.016±0.018 | 1.072±0.023 | 1.026±0.017 | 1.080±0.028 |
| 2 (at 174.4 deg) | C | 7.31±0.14 | 4.71±0.07 | 7.61±0.07 | 5.76±0.09 |
| | E | 6.71±0.06 | - | 7.48±0.013 | 5.76±0.18 |
| | C/E | 1.089±0.023 | - | 1.017±0.010 | 1.000±0.035 |
| 2 (at 90.0 deg) | C | 7.06±0.10 | 4.46±0.10 | 7.42±0.10 | 5.18±0.12 |
| | E | 6.44±0.04 | - | 7.17±0.02 | 5.59±0.16 |
| | C/E | 1.096±0.017 | - | 1.035±0.014 | 0.927±0.034 |
| 4 | C | 15.57±0.13 | 9.42±0.10 | 16.43±0.10 | 11.81±0.14 |
| | E | 13.27±0.59 | 9.70±0.50 | 15.25±0.05 | 12.43±0.32 |
| | C/E | 1.173±0.053 | 0.971±0.051 | 1.077±0.007 | 0.950±0.027 |

¹ The worth of one dollar is 727 pcm in core 7 and 720 pcm in the other cores.

² calculated worth

³ average of measured worths

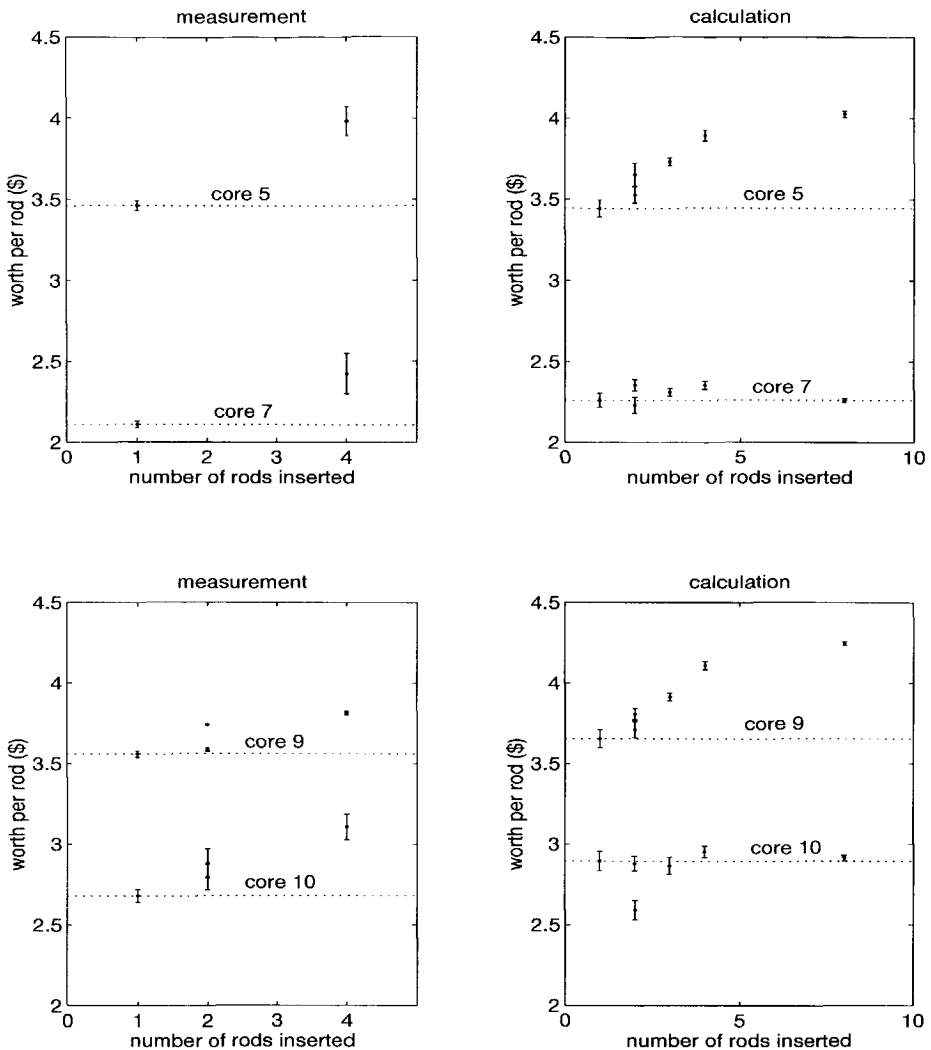


Figure 6.17 The measured and calculated worth per rod inserted as a function of the number of rods inserted. For core 5, only the worths obtained with detector 1 were used.

However, for the cores with the polyethylene rods inserted between the pebbles, the calculations yield much smaller rod interactions (4.2% in core 7 and 2.0% in core 10). This was ascribed to the fact that in these well moderated cores, the root mean square length of the prompt neutron chain (see section 2.1) is small compared to those in the much less moderated cores 5 and 9. This implicates that the individual shutdown rods in cores 7 and 10 are located further apart from each other (from a neutronic point of view) than in cores 5 and 9. Since the change in the flux due to the insertion of a rod in general decreases with the distance from this rod, the shutdown rods in cores 7 and 10 experience the insertion of one or more other shutdown rods less than in cores 5 and 9.

It has to be mentioned that the calculational results are in better agreement with rod worths measured by Rosselet with the epi-thermal PNS technique [9], which indicate an increase in individual rod worth of 12% in cores 5 and 9, and of 6% in core 10 (in core 7, he only measured the bank worth). This result questions the quality of the calculated correction factors for the inverse kinetics technique.

6.6 Discussion and conclusions

In section 6.2 it was demonstrated that noise measurements with pulse detectors in not too deep subcritical systems can be conducted successfully. Experimental evidence has been found for the effect of the finite number of channels predicted in chapter 2. From all applied noise techniques, the Feynman- α method (and its two-detector variant the covariance method) yielded reactivities with the smallest statistical uncertainty, and is therefore the recommended noise analysis technique. It also became clear that in order to achieve the same statistical accuracy in the experimental quantities in various subcritical systems, the total measurement time should increase with subcriticality.

The worth of the auto-rod could be predicted within 18% with first-order perturbation theory. Direct calculations with diffusion theory were seen to overpredict the worth of the fine control rods in cores 5 and 7 by ~21%, whereas the worth in cores 9 and 10 was underestimated by ~12%. Monte-Carlo calculations were seen to agree within 5% with the measured worths, except for core 10, in which the worth was overestimated by 28%. Although in licensing procedures an agreement within 10% is required, the discrepancies found are not expected to have consequences for the HTR design. Recall that the fine control rods are only used for fine control of the reactor and the auto-rod only for maintaining a constant flux level. Shutdown of the reactor is assured by means of the safety and shutdown rods (and the worths of these do agree within 10%). Hence, the worth of the fine control rods and the auto-rod is not a safety issue. In fact, the differences are believed to be acceptable considering the approximations involved in the calculations. Besides this, it must be realised that an accurate calculation of the reactivity worth of the auto-rod and the fine control rods is difficult due to the steep gradient in the thermal flux at the rod locations. In contrast to the absolute worth, the shape of the calibration curves (the variation of the reactivity worth with insertion depth) could be predicted very well, for both the auto-rod and the fine control rods.

The reactivity worth of the safety and shutdown rods was measured with inverse kinetics. Measurements with two or more detectors show that the measured worth depends on the position of the detector, which can be ascribed to changes in the spatial dependence of the flux shape due to the insertion of these rods. This effect is accounted for via calculated correction factors. Although in general the agreement between the various detectors is improved, the differences remain significant. This could be due to an error in the applied correction factors. First of all, the calculated factors are characteristic for an axial plane in the centre of the core region, whereas some detectors were located in the cavity or in the upper axial reflector above the core. Furthermore, the detectors used are quite large (of 22 cm length and of 9 cm diameter) and are quite sensitive, which suggests that they will affect the local flux distribution. This effect is not taken into account in the calculation. For these reasons, it would be preferable to use a full three-dimensional presentation of the system (including the large detectors) to calculate the spatial correction factors.

On the other hand, one should also realise that the detector signal becomes very small after the rod-drop. As the lower limit of the range of the current amplifier is reached, the output of the amplifiers may be no longer proportional to the current from the detector. Furthermore, the output signal may then also be affected by current leakages in the amplifiers. These effects might appear in the linear channel of the nuclear instrumentation, which current amplifiers still originate from the late 1960s.

Monte-Carlo calculations of the reactivity worth of the safety and shutdown rods were seen to be within 10% of the experimental results. Rod worths were also obtained from the (transport theory) calculations of the spatial correction factor. These worths are 4 to 23% lower than the Monte-Carlo worths, which can be explained by the fact that no corrections were applied to the core region to account for the streaming of neutrons. Both the experiments and the calculations showed that the individual rod worth increases as more rods are inserted. This is due to the redistribution of the neutron flux following the insertion of one or more shutdown rods. Because the flux in the vicinity of the inserted rod(s) has decreased, at larger distances from the rod(s) the flux has to increase, and apparently, the shutdown rods are located in a region where the flux has increased. (Note that to compare the flux distributions before and after the rod insertion, the total amount of fissions must be the same).

REFERENCES

- [1] Wallerbos E.J.M., Hoogenboom J.E. and van Dam H.: 'IRI Results for LEU-HTR PROTEUS Cores 5, 7, 9 and 10', report IRI-131-97-005, *Interfaculty Reactor Institute*, Delft, The Netherlands (1997)
- [2] Mathews D. and Williams T.: 'LEU-HTR PROTEUS System Component Description', report TM-41-93-43, *Paul Scherrer Institute*, Villigen, Switzerland (1996)
- [3] Williams, T. et al.: 'Experimental Investigation of the Kinetics Parameter $\beta_{\text{eff}}/\Lambda$ in Graphite-Moderated, LEU-Fuelled, Critical Configurations', *Proc. Int. Conf. on the Physics of Reactors (Physor 96)*, Sept 16-20, Mito, Ibaraki, Japan, Vol. 2, p. E200 (1996)
- [4] Williams, T.: 'Current Status of Methods for Subcriticality Measurement on the PROTEUS Facility', report TM-41-95-08, *Paul Scherrer Institute*, Villigen, Switzerland (1995)
- [5] Williams T. et al.: 'Absorber-Rod Interaction and Asymmetry Effect in Experimental LEU-HTR Configurations', *Proc. 1994 ANS Topical Mtg. on Advances in Reactor Physics*, April 11-15, 1994, Knoxville, USA
- [6] Williams T., Chawla R. and Hager H.: 'Experimental Findings on Reflector Control-Rod Worths in an MHTGR-Like System', *Proc. IAEA Tech. Mtg. on Development Status of Modular HTGRs and their Future Role*, November 28-30, 1994, Petten, The Netherlands
- [7] Mathews, D.: 'HTR-PROTEUS Cores 5 and 7 Safety & Shutdown Rod Worths', report TM-41-96-14, *Paul Scherrer Institute*, Villigen, Switzerland (1996)
- [8] Williams, T.: 'The Calculation of Kinetics Data for Use in the Simmons-King Analysis of Pulsed Neutron Measurements', report TM-41-93-36, *Paul Scherrer Institute*, Villigen, Switzerland (1994)
- [9] Rosselet, M.: personal communication, Febr. 1997
- [10] Massimo L.: 'Physics of High-Temperature Reactors', Pergamon Press, Oxford, section 4.14 (1976)

Chapter 7

Effects of accidental water ingress

7.1 Introduction

The cores of high-temperature reactors are usually undermoderated in order to give the reflector enough importance to enable one to locate the shutdown rods in the reflector, and as a result of economic considerations. It is well known that water ingress in such a core can lead to a significant increase in reactivity [1]. However, many publications (e.g. Ref. 2, 3, 4) on water ingress in an HTR focus on the response of power reactors and are of thermalhydraulic or chemical nature with no or very little attention for neutronic effects. For in such a reactor, the water vaporises on entering the core which leads to a pressure rise. Furthermore, the steam corrodes the graphite of the pebbles and of the core structure, which can weaken the structure, influence the heat transfer characteristics of the core, and can lead to explosive mixtures of air/helium/hydrogen/carbon-monoxide. These effects are considered more dangerous than a power excursion.

Nevertheless, some studies of water ingress from a neutronic point of view have been published, e.g. Ref. 5 and 6, and show that an introduction of water leads to higher neutron thermalization which results in a fission increase in the thermal range. Furthermore, the presence of water in the inter-pebble void reduces the leakage of neutrons from the core. Due to these two effects the reactivity increases. However, as more water enters the core the absorption in hydrogen becomes more and more dominating which results in a decrease of the reactivity.

In PROTEUS, detailed insight into the space-dependent effect of local water ingress was obtained by oscillating a small water sample near the axis of the core, see chapter 5. As figure 5.16 shows, the reactivity effect is negative in the reflector which can be ascribed to the higher absorption cross-section of hydrogen as compared to graphite in a well thermalised spectrum. In the undermoderated cores the effect is positive with the maximum in the lower half of the core.

The presence of larger amounts of water was simulated with CH_2 as the use of water was not practical. With oscillations of both CH_2 and H_2O samples, it could be demonstrated experimentally that the reactivity worths per mole are the same (see chapter 5). Note however that due to the different molecular weights the worths per unit mass are not the same ! Also, replacing the CH_2 by H_2O (leaving the atomic densities unchanged) in the KENO model of core 7 yielded the same multiplication constant within the statistical uncertainty. These results justify the use of polyethylene instead of water.

In this chapter, various neutronic effects of water ingress will be addressed, starting in section 7.2 with the effect on the kinetic parameter. In section 7.3 the effect on the multiplication constant in two systems with different moderation ratios will be investigated, followed by a study of the worth of the safety/shutdown rods in the dry and wet configurations in section 7.4. In section 7.5 two accidental water ingress scenarios in core 5 are investigated. As PROTEUS operates at room temperature, an incident that might happen is the flooding of the core due to a break of a water pipe in the reactor building. In the second scenario it is assumed that the inter-pebble void and the cavity above the pebble bed is filled with water vapour. This chapter ends with a summary in section 7.6.

7.2 Effect on the kinetic parameter $\beta_{\text{eff}}/\Lambda$

Although the kinetic parameter was discussed in chapter 3, this section about the effect of water on the kinetic parameter is included as a change of its value is of importance for transient analysis. From chapter 3, one can conclude that the ingress of water reduces the generation time Λ . First of all, this is due to the fact that water is a more effective moderator than graphite, as a result of which neutrons get thermalised faster and thus (on average) induce a fission earlier. Note that neutrons reside a relatively long time in the reflector before returning to the core, and therefore reflector neutrons increase the generation time. Since the ingress of water reduces the streaming of neutrons from the core to the reflector, this also leads to a reduction of the generation time.

Besides the generation time, the ingress of water also influences the effective fraction of delayed neutrons. Since the average energy of prompt neutrons is higher than that of delayed neutrons, and the absorption cross section of water increases with decreasing energy, the leakage of delayed neutrons decreases more significantly than the leakage of prompt neutrons, i.e. β_{eff} increases. Note however, that the change in β_{eff} is much smaller than the change in the generation time (see also chapter 3). Furthermore, it should be mentioned that also the core height has some effect on β_{eff} : with decreasing core height, the core surface-volume ratio increases. As the slower (delayed) neutrons can escape from a smaller area near the core-reflector boundary than the fast (prompt) neutrons, the leakage of delayed neutrons increases with regard to the leakage of prompt neutrons, i.e. β_{eff} decreases (compare β_{eff} of cores 5 and 9).

Hence, due to the water ingress β_{eff} increases and Λ decreases, and thus the kinetic parameter $\beta_{\text{eff}}/\Lambda$ increases. As was demonstrated in chapter 3, this change in particular influences the prompt decay constant, and is thus of importance for transient analysis on a short time scale.

7.3 Effect on the multiplication constant

The effect of the CH_2 rods alone cannot be derived from a comparison of the measured multiplication constants of the dry cores (cores 5 and 9) and of the wet cores (cores 7 and 10), for the core heights are not the same. Hence, the k_{eff} has to be known of the core 7 and 10 configurations from which all CH_2 rods are removed. Unfortunately, (to the knowledge of the author) these have not been measured, but, as was demonstrated in chapter 4, with a detailed KENO model they can be accurately predicted. As the layout of cores 7 and 10 without CH_2

rods are identical to those of cores 5 and 9, no new cross sections were required. The results can be found in table 7.1.

Table 7.1. The calculated reactivity effects ($\pm 1\sigma$) of inserting CH_2 rods

| | core 7 | core 10 |
|-----------------------|--|--|
| with CH_2 | $k_{\text{eff}} = 1.00572 \pm 0.00051$ | $k_{\text{eff}} = 1.00434 \pm 0.00059$ |
| without CH_2 | $k_{\text{eff}} = 0.93202 \pm 0.00071$ | $k_{\text{eff}} = 0.97024 \pm 0.00051$ |
| adding CH_2 | $\Delta k = +0.07370 \pm 0.00087$ | $\Delta k = +0.03410 \pm 0.00078$ |

According to these KENO calculations, the placement of the 654 CH_2 rods in the core 7 configuration increases k_{eff} by 7.37 %. Assuming that k_{eff} of core 7 without CH_2 , just like k_{eff} of core 5, is over predicted by 0.74 % compared to the experiment (see section 4.3.1), and knowing that k_{eff} of core 7 is over predicted by 0.05 %, the estimated effect on k_{eff} of the polyethylene rods is $7.37 + 0.74 - 0.05 = (8.06 \pm 0.13)$ %, which is in good agreement with the result obtained by PSI [7]. Similarly, for the core 10 configuration the estimated effect on k_{eff} is an increase of (3.72 ± 0.11) %. The most important reason for the large difference between the increases in k_{eff} is not the different moderation ratios in the cores before the CH_2 was inserted, but the difference in CH_2 loadings. Recall that in core 7 the CH_2 loading is 32.63 kg/m^3 whereas in core 10 it amounts only 15.21 kg/m^3 . In particular in case of core 7, the increase of k_{eff} is considerable, but Monte Carlo calculations by Xu [7] showed that dispersion of the water (or CH_2) in the inter-pebble space results in an even larger increase of k_{eff} (8.52 %). These large increases rise the question whether they can be compensated by the insertion of the safety and shutdown rods. This will be the subject of the next section.

7.4 Effect on reflector-based absorber-rods

In order to assess the effect of the insertion of CH_2 rods in the core region on the worth of the safety and shutdown rods, the worths of individual rods and of some combinations of rods in cores 7 and 10 without CH_2 rods have been calculated with KENO. The results can be found in tables 7.2 and 7.3.

Table 7.2. The reactivity worths (%) of safety/shutdown rods in core 7 with and without CH_2

| rods inserted | core 7 without CH_2 | core 7 | ratio with/ without CH_2 |
|---------------|---------------------------------|--------------------|--------------------------------------|
| 1 | 2.837 ± 0.152 | 1.679 ± 0.051 | 0.592 ± 0.036 |
| 1+2 | 6.012 ± 0.122 | 3.410 ± 0.073 | 0.567 ± 0.017 |
| 1+2+3 | - | 5.038 ± 0.073 | - |
| 1 - 4 | 12.766 ± 0.140 | 6.848 ± 0.073 | 0.536 ± 0.008 |
| 1 - 8 | 25.515 ± 0.141 | 13.137 ± 0.080 | 0.515 ± 0.004 |

Table 7.3. The reactivity worths (%) of safety/shutdown rods in core 10 with and without CH₂

| rods inserted | core 10 without CH ₂ | core 10 | ratio with/without CH ₂ |
|---------------|---------------------------------|--------------|------------------------------------|
| 1 | 2.899±0.079 | 2.045±0.086 | 0.705±0.035 |
| 1+2 | 6.072±0.090 | 4.118±0.086 | 0.678±0.017 |
| 1+2+3 | 9.076±0.091 | 6.300±0.094 | 0.694±0.012 |
| 1 - 4 | 12.712±0.090 | 8.503±0.101 | 0.669±0.009 |
| 1 - 8 | 26.137±0.102 | 16.790±0.094 | 0.642±0.004 |

These tables show that due to the water ingress the worth of the reflector based safety and shutdown rods decreases dramatically. This decrease can be explained by the decreased leakage of neutrons from the core to the reflector, which is due to the softer neutron spectrum and the partial blocking of the inter-pebble channels. Indeed, of the two configurations investigated, the core 7 configuration shows the largest increase in reactivity and the maximal decrease in rod worth due to the insertion of CH₂ rods. In fact, in that particular case the reactivity increase cannot be compensated anymore by the four shutdown rods alone. However, the reactor can still be shutdown by inserting all shutdown and safety rods simultaneously.

Furthermore, the tables show that the decrease in rod worth depends on the number of rods inserted. This is due to the interactions between the rods in the 'dry' configurations: in core 7 without CH₂ the worth per rod increases from ~2.8 % with one rod inserted to ~3.2 % with eight rods inserted. On the other hand, in core 7 the rod interactions are weak with the worth per rod varying only between 1.64 and 1.71 %. For a more detailed discussion of these effects, see section 6.5.

7.5 Simulation of water ingress in core 5

As mentioned in the introduction of this chapter, in this section two different water ingress scenarios in core 5 are investigated. In the first scenario it is assumed that water entering the core remains in the liquid phase. For HTR-PROTEUS this is a reasonable assumption since the facility operates at room temperature. In the second scenario the presence of water vapour in the inter-pebble void and in the cavity above the pebble bed is assumed. This is the scenario normally considered for a power reactor. Because of the high temperature in such a reactor water entering the core vaporises and the steam will then spread out in the entire inter-pebble space.

The investigations of the first scenario comprised a simulation of the flooding of core 5. The reactivity was calculated with KENO for 12 different water levels. It was assumed that the water had a density of 1 g/cm³. First, the Dancoff factor was recalculated and found to be 0.271. In chapter 4 the Dancoff factor of the dry core was calculated to be 0.292. The second term of the total Dancoff factor, i.e. the probability that a neutron from one pebble is absorbed by fuel in another pebble, almost completely vanishes (now 0.0025 compared to 0.0235 in the dry core; a reduction of 89.4 %), but as this term contributed only about 9 % to the total value, the net effect is modest (a reduction by 7.8 %). Using the new Dancoff factor, and water added to the third region of the unit cell of the pebble lattice (see section 4.1.3), new cross sections

were generated that were added to the existing cross-sections library for core 5. The XSDRNPM run of step 4 of the cross-section generation procedure (see section 4.1.3) yielded $k_{\infty}=0.756272$, whereas in the case of core 5, $k_{\infty}=1.72899$. This indicates that the flooded region of the core is considerably over moderated and that the negative effect of absorptions by hydrogen strongly dominates the positive effect of the extra moderation.

Figure 7.1 shows the calculated multiplication constant for various water levels in the core. It can be seen that the reactivity effect of the water is always negative, and hence, the flooding of the core will not lead to problems with respect to reactivity.

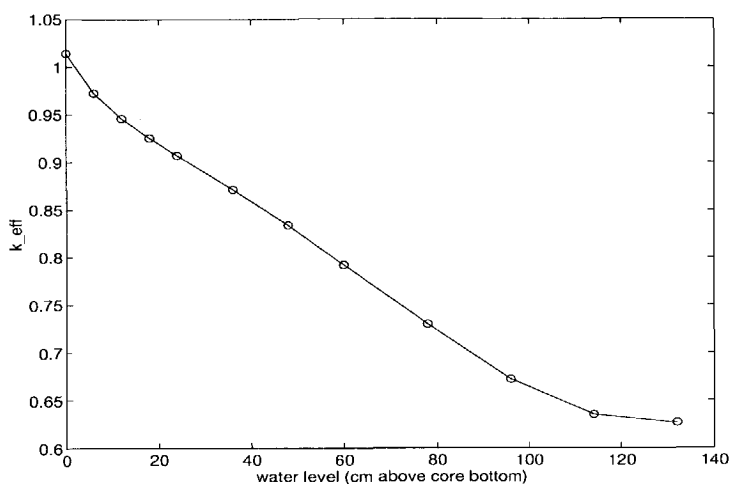


Figure 7.1 The multiplication constant as a function of the water level in core 5.

The second water ingress scenario comprises the entrance of water vapour into the core and cavity region of core 5. Although it would be very illustrative to show the multiplication constant versus the vapour density, just one point of this curve was calculated. A vapour density of 0.106 g/cm^3 was assumed, as this corresponds to the amount of CH_2 in core 7. Therefore, the cross section library of core 7 can be used, and thus the need to generate new cross sections is avoided. This vapour density turned out to have a strong positive reactivity effect: $k_{eff} = 1.05913 \pm 0.00052$, which means an increase of 0.0441 ± 0.0008 relative to the dry core ! With four shutdown rods inserted to compensate this reactivity, it was found that $k_{eff} = 1.00952 \pm 0.00057$. By inserting the four safety rods as well, the reactor becomes subcritical: $k_{eff} = 0.96613 \pm 0.00051$. The following conclusions can be drawn:

1. The reactor cannot be made subcritical with four shutdown rods. By inserting the four safety rods as well, the reactor can be shutdown.
2. Compared to the dry core the worth of the four shutdown rods is decreased by 58.6 % (from 15.57 \$ to 6.44 \$). This relative reduction is even larger than that due to the insertion of 8.3 mm CH_2 rods.
3. As more rods are inserted, the rod worth decreases relatively: the worth of the eight rods now is 12.62 ± 0.10 \$, which in core 5 used to be 32.21 ± 0.15 \$, which means a reduction of 60.8 % !

7.6 Summary

In this chapter some effects of accidental water ingress on the neutronics of an HTR were discussed. Although the emphasis is on reactivity effects, one should realise that also the generation time, and in lesser extent, the effective fraction of delayed neutrons are affected. The generation time decreases as a result of which the system reacts faster on reactivity changes, which is of importance for transient analysis on short time scales. The effective fraction of delayed neutrons increases somewhat, which means that the margin to prompt criticality also increases a little bit.

In the undermoderated HTR cores, extra moderating material in general increases the reactivity. It has been demonstrated that due to the reduced leakage of fast neutrons to the reflector, the worth of the reflector-based absorber rods decreases dramatically, e.g. due to the ingress of water vapour with a density of 0.106 g/cm^3 in core 5, the rods lose about 60 % of their worth. This leads to the question whether the wet system can still be shutdown with the safety and shutdown rods. In the example of the ingress of vapour presented in section 7.5, the system could only be shutdown with all eight safety and shutdown rods.

In section 7.5 it was also shown that the ingress of water leads to a decrease of system reactivity, even if only one layer of pebbles was flooded. The net reactivity effect is negative as the flooded part of the core is over moderated, meaning that the negative reactivity effect of the extra absorptions in hydrogen dominates the positive reactivity effect due to the extra moderation. It can be concluded that the ingress of water in undermoderated cores is not a safety issue.

REFERENCES

- [1] Baust E., *Atomwirtschaft*, **14** 122 (1969)
- [2] Kugeler K. and Schulten R., *Hochtemperaturreaktortechnik*, Springer-Verlag, Berlin (1989)
- [3] Wawrzik U., *Numerische Simulation des Anlagenverhaltens eines Hochtemperaturreaktors bei Wassereinbruchstörfällen am Beispiel des AVR*, Dissertation RWTH Aachen (1983)
- [4] Fassbender J. et al., 'Zur Störfalltopologie des Hochtemperaturreaktors', *Atomkernenergie/Kerntechnik* **37** 81-86 (1981)
- [5] Chawla R., 'On the reactivity effects of water entry in pebble-bed HTR lattices', *Ann. Nucl. Energy* **8** 525-529 (1981)
- [6] Pelloni S. et al., 'Parameter study on water ingress in a high temperature reactor', *Kerntechnik* **53** 233-238 (1989)
- [7] Xu Y. and Joneja O.P., 'Monte Carlo Simulation of HTR-PROTEUS Core 7 and Comparison of Results with the Measurements and TWODANT Calculations', *PSI technical memorandum TM-41-96-30*, Paul Scherrer Institute, Villigen, Switzerland (1996)

Summary

There is a renewed interest in the concept of the high-temperature gas-cooled reactor, mainly because of its passive safety characteristics. In order to provide data against which safety-related calculations could be validated, a four-year experimental programme was carried out at the HTR-PROTEUS facility of the Paul Scherrer Institute (Switzerland). In the framework of this programme, a both experimental and calculational study of various reactivity effects in HTR-PROTEUS was performed. Reactivity quantifies the balance between the production and loss of neutrons in a system. Some methods to measure (changes in) the reactivity are reviewed, including the pulsed-neutron source method, the inverse-kinetics technique, and noise analysis techniques. It was found that the models commonly used in the analysis of noise measurements do not yield the expectation values of the experimental quantities. As a result, the inferred reactivity values are biased. New expressions which truly represent the expectation values of the experimental quantities have been derived.

All presented reactivity measurement techniques depend on kinetics parameters. Recommendations are given for the method of calculation of these parameters. One parameter, the reduced neutron generation time, has been measured with a noise technique applied to the reactor in a critical state. In two of the four core configurations that have been analysed, the measured values are in good agreement with the calculated values. The application of noise techniques is problematic due to the long generation time, which was found to be about 2 ms. Because this is at least a factor of 10 longer than in a light water reactor, in many practical cases the decay of the prompt and of the delayed neutrons cannot be separated, and the commonly encountered simplifying assumptions in the analysis of kinetic experiments in light water reactors are not valid.

Both Monte Carlo and deterministic codes have been used to analyse the experiments. However, before these calculations can be started, neutron interaction cross sections have to be generated. A multi-step procedure was developed which explicitly considers the coated fuel particles within the fuel pebbles. The multi-group Monte Carlo code KENO-Va enables a very detailed modelling of the facility; the fuel zone of a fuel pebble was homogenised, but all pebbles in the core region were treated explicitly. The calculated critical balances of four configurations agreed within 0.64% with the experimental results. The agreement was seen to improve with the amount of moderation in the core region, which could indicate shortcomings in the treatment of epi-thermal resonance absorptions in ^{238}U . The calculations with deterministic codes overestimate the reactivity by several percent. As in these codes the pebbles cannot be modelled explicitly, the core region was homogenised. The homogenisation conserves the reaction rates, but not the neutron diffusion properties. As a result, the streaming of neutrons from the core to the reflector is underestimated.

In diffusion theory calculations, the diffusion of neutrons in a region can be increased by increasing the diffusion coefficient. In the code BOLD VENTURE the diffusion coefficient of the homogenised core region was increased until the reduction in k_{eff} was in agreement with the reduction calculated with KENO. Although a correct neutron balance is obtained in this way, and hence the flux and adjoint function can be used to compute integral parameters like the generation time, the flux profile in the core is not correct, as a comparison of computed and measured reaction rates in ^{235}U and ^{238}U showed.

The calculated fluxes were also used by the first-order perturbation theory code PERT-V to compute the spatially dependent reactivity effect of several small material samples. The calculations with modified diffusion coefficient do not entirely predict the shape of the traverse correctly. All calculations overestimate the reactivity effect by about 17%. The only exception is the gadolinium oxide sample, which effect is underestimated by about 70%. This could indicate an error in the gadolinium cross section, but an error in the specification of the sample composition is believed to be more likely. The overestimation could be shown not to be the result of self-shielding alone. The application of first-order perturbation theory, i.e. the assumption that the disturbance of flux and adjoint function is not significant, might also explain the overestimation. This could be investigated by calculating the reactivity effect by direct calculations.

The use of CH_2 to simulate the presence of water was justified by calculations with KENO and by the oscillation of CH_2 and water samples. The oscillation of the small water sample yielded detailed insight in the effect of local water ingress, which is a safety issue. In the undermoderated core the reactivity effect is positive. In the reflector on the other hand, the effect is negative as the absorption cross section of hydrogen is larger than that of graphite in a well moderated environment. The insertion of CH_2 rods into the core increases the reactivity because they simultaneously enhance the moderation in the undermoderated core and reduce the leakage of neutrons to the reflector. This reactivity increase was compensated by reducing the core height.

Although the application of noise analysis to determine the reactivity is difficult in systems with a long generation time, meaningful results were obtained. For instance, experimental evidence has been found for the predicted effect of the finite measurement time. However, the measurements in deep subcritical states were not very successful. The inverse kinetics technique was selected as the standard technique to measure the worth of reflector-based absorber-rods. The worth of the auto-rod was calculated with first-order perturbation theory and was seen to agree with the measurements within 18%. With diffusion theory, the worth of the fine control rods could be predicted within about 20%. Except for one configuration, the Monte-Carlo calculations were seen to agree within 5%. Considering the approximations involved in the calculations and the steep gradient in the thermal flux at the rod locations, these results are acceptable. Note that these rods are only used for the fine control of the reactor and not to shutdown the reactor. Therefore, these rod worths and the accuracy with which they can be calculated are not safety issues and will not have consequences for the HTR design.

The measurement of the worth of safety and shutdown rods with two or more detectors, demonstrated the presence of significant spatial effects. Due to the application of calculated correction factors, the agreement between reactivities obtained with individual detectors was seen to improve. Monte-Carlo calculations of the reactivity worths agreed within 10% with the experimental results, and hence meet the requirements of licensing procedures. Both the calculations and the measurements demonstrate how due to the insertion of CH_2 rods into the core, the reactivity worth of the reflector based control rods reduces significantly (e.g. the worth of the four shutdown rods in core 7 is about 40% lower than in core 5). This can be ascribed to the reduced leakage of neutrons to the reflector.

Finally, two abnormal situations in core 5 have been simulated with KENO. First of all, the presence of water vapour with a density of 0.106 g/cm^3 (which corresponds to the amount of CH_2 in core 7) was calculated to yield a reactivity increase of 4.4%. The worth of the four shutdown rods was seen to reduce from 11.2% in the 'dry' configuration to 5.0%. In fact, this is not enough to compensate the total overreactivity of the 'wet' configuration. However, by inserting the four safety rods as well, the reactor can be safely shutdown. In the second case, it was assumed that water enters the core and remains in the liquid phase. The flooded part of the core was varied. It turned out that the reactivity effect of this flooding is always negative. Due to the high hydrogen density, the flooded part of the core is strongly overmoderated and hence, the negative effect of the absorptions in hydrogen dominates the positive effects of the extra moderation and the reduced neutron leakage.

Samenvatting

Er is een hernieuwde belangstelling voor de hoge-temperatuur, gasgekoelde kernreactor, voornamelijk vanwege zijn passieve veiligheidseigenschappen. Om gegevens te verkrijgen waarmee berekeningen gevalideerd kunnen worden, is er een vier jaren durend experimenteel programma uitgevoerd in de HTR-PROTEUS faciliteit van het Paul Scherrer Instituut. In het kader van dit programma is zowel experimenteel als numeriek onderzoek naar verschillende reactiviteitseffecten in HTR-PROTEUS verricht. Reactiviteit kwantificeert de balans tussen de productie en het verlies van neutronen in een systeem. Een aantal methoden om (veranderingen in) de reactiviteit te meten, zoals de methode met de gepulste neutronen bron, de inverse kinetica en ruisanalyse-technieken, worden kort behandeld. Er is geconstateerd dat de modellen die gewoonlijk gebruikt worden in de ruisanalyse-technieken niet de verwachtingswaarden van de experimentele grootheden opleveren. Daardoor vertonen de waarden die met deze methoden bepaald worden een systematische afwijking. Nieuwe uitdrukkingen zijn afgeleid die wel overeenkomen met de verwachtingswaarde van de experimentele grootheden.

De geïntroduceerde reactiviteitsmeettechnieken zijn afhankelijk van kinetische parameters. Er worden aanbevelingen gedaan betreffende de te gebruiken berekeningsmethode voor deze parameters. De gereduceerde neutronengeneratietijd, één van de parameters, is m.b.v. een ruisteknik gemeten in een kritieke situatie. In twee van de vier onderzochte kernconfiguraties blijken de gemeten en berekende waarden goed overeen te stemmen. De toepassing van ruis-analysetechnieken is problematisch door de lange generatietijd, die ongeveer 2 ms bedraagt. Dit is minimaal een factor 10 langer is dan voor een typische lichtwaterreactor. Hierdoor kan in veel praktische gevallen het verval van de prompte neutronen niet gescheiden worden van het verval van de nakomende neutronen. Dientengevolge zijn de vereenvoudigende aannamen die gewoonlijk in de analyse van kinetische experimenten in lichtwaterreactoren gemaakt worden, nu niet meer geldig.

Voor de analyse van de experimenten zijn zowel Monte-Carlo als deterministische computerprogramma's gebruikt. Voordat deze berekeningen uitgevoerd kunnen worden, moeten er werkzame doorsneden voor neutroneninteracties gegenereerd worden. Er is een procedure ontwikkeld, bestaande uit meerdere stappen, waarin de gecoate brandstofdeeltjes in de brandstofbollen expliciet in rekening gebracht worden. De multi-groep Monte-Carlo code KENO-Va maakt een zeer gedetailleerde modellering van de experimentele faciliteit mogelijk; in het model is weliswaar de brandstofzone van een brandstofbol gehomogeniseerd, maar alle bollen zijn bijvoorbeeld wel expliciet gemodelleerd. De berekende kritieke balans voor ieder van de vier kernconfiguraties komt binnen 0.64% overeen met de experimentele waarde. De overeenstemming wordt beter naarmate de moderatie in de kern toeneemt, wat zou kunnen duiden op een tekortkoming in de behandeling van epithermische resonantieabsorpties in ^{238}U . De berekeningen met deterministische codes overschatten de reactiviteit met een aantal procenten. Omdat in deze codes de bollen niet expliciet gemodelleerd kunnen worden, wordt de kern gehomogeniseerd. Door deze homogenisatie worden wel de reactietempo's geconserveerd maar niet de diffusie-eigenschappen van neutronen. Dit resulteert in een onderschatting van de lek van neutronen van de kern naar de reflector.

In diffusietheorieberekeningen kan de diffusie van neutronen in een zone vergroot worden door de diffusiecoëfficiënt groter te maken. In de code BOLD VENTURE is de diffusiecoëfficiënt van de gehomogeniseerde kern vergroot totdat de afname in k_{eff} in overeenstemming was met de afname zoals berekend met KENO. Alhoewel op deze manier een correcte neutronenbalans verkregen wordt, zodat de flux en de geadjungeerde functie gebruikt kunnen worden voor de berekening van een integrale parameter zoals de generatietijd, is het fluxprofiel in de kern niet correct. Dit kan gedemonstreerd worden door een vergelijking van berekende axiale verdelingen van reactietempo's in ^{235}U en ^{238}U met gemeten verdelingen.

De berekende fluxen zijn ook gebruikt in de eerste-orde verstoringstheorie code PERT-V om het plaatsafhankelijke reactiviteitseffect van verschillende materiaalmonsters te berekenen. De berekeningen met de gemodificeerde diffusiecoëfficiënt voorspellen de vorm van de plaatsafhankelijkheid niet helemaal correct. Alle berekeningen overschatten het reactiviteitseffect met ongeveer 17%. De enige uitzondering vormt het gadoliniumoxyde monster, waarvan het effect met ongeveer 70% onderschat wordt. Dit kan duiden op een fout in de werkzame doorsnede van gadolinium, maar een fout in de specificatie van de samenstelling van het monster lijkt waarschijnlijker. Het is aangetoond dat zelfafscherming alleen niet verantwoordelijk kan zijn voor de overschatting. De toepassing van eerste-orde verstoringstheorie, met andere woorden, de aanname dat de verstoringen in de flux en de geadjungeerde functie niet significant zijn, zou ook de overschatting kunnen verklaren. Dit zou onderzocht kunnen worden door het reactiviteitseffect te bepalen m.b.v. het verschil tussen twee directe k -eigenwaarde berekeningen.

Het gebruik van CH_2 om de aanwezigheid van water te simuleren is gerechtvaardigd d.m.v. berekeningen met KENO en oscillaties van zowel CH_2 - als watermonsters. De oscillatie van het watermonster levert een gedetailleerd inzicht in het effect van een lokale waterinbreuk, wat een veiligheidskwestie is. In de ondergemodereerde kern is het reactiviteitseffect positief. In de reflector echter is het effect negatief omdat de absorptie werkzame doorsnede van waterstof groter is dan van grafiët. De plaatsing van CH_2 staven in de kern verhoogt de reactiviteit omdat ze zowel de moderatie in de ondergemodereerde kern verhogen als de lek van neutronen naar de reflector verminderen. Deze reactiviteitstoename is gecompenseerd door de kernhoogte te verminderen.

Alhoewel de toepassing van ruis-analysetechnieken voor de bepaling van de reactiviteit moeilijk is in systemen met een lange generatietijd, zijn er zinvolle resultaten behaald. Zo is er experimenteel bewijs gevonden voor het voorspelde effect van de eindige meettijd. De metingen in diep subkritieke systemen waren echter niet succesvol. De inverse kinetica techniek is gekozen als standaard techniek om de waarde van de regelstaven in de reflector te meten. De waarde van de automatische regelstaaf is berekend met eerste-orde verstoringstheorie. Deze bleek beter dan 18% overeen te komen met de gemeten waarden. Met diffusietheorie kon de waarde van de fijne regelstaven met een nauwkeurigheid van 20% berekend worden. Met uitzondering van één configuratie, kwamen de Monte-Carlo berekeningen binnen 5% overeen met de gemeten waarden. Rekening houdend met de vereenvoudigende aannamen in de berekeningen en de steile gradiënt in de thermische flux ter hoogte van de staafposities, zijn deze resultaten aanvaardbaar. Omdat deze regelstaven alleen gebruikt worden voor de fijne afregeling en niet voor de afschakeling van de reactor, zijn deze regelstaafwaarden en de nauwkeurigheid waarmee deze berekend kunnen worden

geen veiligheidskwesties. Ze zullen daarom geen consequenties hebben voor het ontwerp van een HTR.

De meting van de waarde van de veiligheids- en afschakelstaven met twee of meer detectoren, toonden de aanwezigheid van plaatsafhankelijk effecten aan. Door de toepassing van berekende correctiefactoren verbeterde de overeenkomst in de reactiviteiten zoals gemeten met de individuele detectoren. Monte-Carlo berekeningen kwamen binnen 10% overeen met de metingen, waarmee voldaan wordt aan de eisen van goedkeuringsprocedures. Zowel de metingen als de berekeningen laten zien hoe door de plaatsing van CH_2 staven tussen de bollen, de reactiviteitswaarde van de staven in de reflector drastisch afneemt (de waarde van de vier afschakelstaven in kern 7 bijvoorbeeld is ongeveer 40% lager dan in kern 5). Dit kan worden toegeschreven aan de afgenomen lek van neutronen naar de reflector.

Twee abnormale situaties in kern 5 zijn gesimuleerd met KENO. In het eerste geval is het reactiviteitseffect van de aanwezigheid van waterdamp met een dichtheid van 0.106 g/cm^3 (dit komt overeen met de hoeveelheid CH_2 in kern 7) berekend. Dit leidt tot een toename van de overreactiviteit van 4.4% terwijl de waarde van de vier afschakelstaven afneemt van 11.2% in de 'droge' configuratie tot 5.0% in de 'natte' configuratie. Dit is niet genoeg om de totale overreactiviteit van de 'natte' configuratie te compenseren. Door echter ook de vier veiligheidsstaven in te drijven zou de reactor zonder problemen afgeschakeld kunnen worden. In het tweede geval is aangenomen dat water in de kern stroomt en niet verdampt. De hoogte van het ondergelopen deel van de kern is gevarieerd. In alle gevallen blijkt het reactiviteitseffect negatief. Door de hoge dichtheid van waterstofatomen in water is het ondergelopen deel overgemodereerd. Hierdoor overheerst het negatieve reactiviteitseffect ten gevolge van absorpties in waterstof de positieve effecten ten gevolge van de extra moderatie en de afname van de lek van neutronen.

List of publications

E.J.M. Wallerbos and J.E. Hoogenboom, "Experimental demonstration of the finite measurement time effect on the Feynman- α technique", accepted for publication in *Annals of Nuclear Energy*

E.J.M. Wallerbos, J.E. Hoogenboom, T. Williams, "Experimental and calculational analysis of reactivity effects in an HTR core configuration", accepted for publication on ICENES '98, June 28 - July 2, Tel Aviv, Israel (1998)

E.J.M. Wallerbos and J.E. Hoogenboom: "The forgotten effect of the finite measurement time on various noise analysis techniques", *Annals of Nuclear Energy* **25** p. 733-746 (1998)

E.J.M. Wallerbos and J.E. Hoogenboom: "On the measurement and calculation of the kinetic parameter β_{eff}/Λ of a small high-temperature like, critical system", *Journal of Nuclear Science and Technology* **35** p.26-33 (1998)

E.J.M. Wallerbos and J.E. Hoogenboom: "Experimental investigation of the count-loss effect due to the time interval between counting-gates in the Feynman- α method", *Annals of Nuclear Energy* **25** p. 203-208 (1998)

E.J.M. Wallerbos, A. Hogenbirk and J.E. Hoogenboom: "Calculations of reactivity effects of water ingress and neutron streaming in HTR-PROTEUS, a small low-enriched uranium fuelled pebble-bed system", *Proc. Joint Int. Conf. on Mathematical methods and supercomputing for nuclear applications*, Saratoga Springs, New York, 6-10 Oct, p. 637-646 (1997)

E.J.M. Wallerbos and R. van Geemert: "Academic Nuclear Education: The Dutch Way", *Nuclear Europe Worldscan*, Vol XVII, no. 9-10, Sept-Oct, p. 43 (1997)

E.J.M. Wallerbos and D. Mathews, "Reactivity effects of small samples in a graphite-moderated low-enriched uranium fueled, critical configuration", *Proc. Jahrestagung Kerntechnik*, May 21-23, Mannheim, Germany, p.35-38 (1996)

J.E. Hoogenboom, E.J.M. Wallerbos, T.H.J.J. van der Hagen, H. van Dam, E. Turkcan, "Survey of HTR related research at IRI, Delft", *NEA Workshop on High Temperature Engineering research facilities and experiments*, Petten, The Netherlands, November 12-14 (1997)

T. Williams, M. Rosselet, R. Chawla, E. Wallerbos, H. van Dam: "Experimental Investigation of the kinetics parameter β_{eff}/Λ in graphite-moderated, LEU-fuelled, critical configurations", *Proc. Int. Conf. On the Physics of Reactors (Physor)*, Sept 16-20, Mito, Ibaraki, Japan, Vol. 2, p. E200-E209 (1996)

J. Valko, E.J.M. Wallerbos, J.E. Hoogenboom, H. van Dam, "Calculations of the LEU HTR-PROTEUS Benchmarks and preliminary experimental results of the HTR research programme of IRI", *Proc. ECN Workshop on the role of modular HTRs in the Netherlands*, Nov 30 - Dec 1, Petten, The Netherlands (1994)

E.J.M. Wallerbos, J.E. Hoogenboom, H. van Dam: "IRI results for LEU HTR-PROTEUS Cores 5, 7, 9, and 10", report IRI-131-97-005, *Interfaculty Reactor Institute*, Delft, The Netherlands (1997)

E.J.M. Wallerbos: "The spatially dependent reactivity effects of various small samples in HTR-PROTEUS Cores 5 and 7", report IRI-131-96-027, *Interfaculty Reactor Institute*, Delft, The Netherlands (1996)

E.J.M. Wallerbos: "Determination of the reduced generation time Λ/β from power spectral density measurements", report TM-41-95-13, *Paul Scherrer Institute*, Villigen, Switzerland (1995)

E.J.M. Wallerbos: "Investigation of the application of noise techniques to HTR-PROTEUS", report TM-41-94-24, *Paul Scherrer Institute*, Villigen, Switzerland (1994)

Curriculum Vitae

The author of this thesis was born on January 1st 1968 in Lichtenvoorde, the Netherlands. In 1986, after completing the secondary school ('VWO') in Groenlo, he went to the Twente University of Technology, located in Enschede, to study applied physics. In his third year at the university, he developed during a three months stay at VG Elemental, Winsford, England, an auto-tune system for the electrostatic ion-lenses of a mass-spectrometer. He graduated in the Instrumentation and Measurement Technology department of prof. ir. J.E. Rijnsdorp. He performed his graduation work at Shell Moerdijk, where he worked on the development of mathematical models to describe the dynamic behaviour of various heat exchangers and distillation-columns. He obtained his masters degree in April 1992 with a specialisation in computer science.

After having fulfilled his national service, he joined the reactor physics department of the Interfaculty Reactor Institute (IRI) in September 1993 to commence his PhD-work on reactivity effects in pebble-bed type nuclear reactors under supervision of dr. ir. J.E. Hoogenboom and prof. dr. ir. H. van Dam. In the framework of the IAEA co-ordinated research program on the validation of safety related physics calculations for low-enriched gas-cooled reactors, he was assigned to the HTR-PROTEUS group of the Swiss Paul Scherrer Institute (PSI) in the period from June 1994 till September 1995. During this period, as well as during several short visits in 1996, he performed the experimental part of his PhD-work, supervised also by dr. T. Williams and prof. dr. R. Chawla of PSI. At the IRI, he worked till November 1997 on the analysis of the HTR-PROTEUS experiments, described in this thesis.

From November 1997 till February 1998, he was again employed by the IRI to work in the framework of the IAEA co-ordinated research program 'Evaluation of high-temperature gas-cooled reactor performance' on the theoretical analysis of the start-up core physics of the Japanese High-Temperature Engineering Test Reactor. Since February 1998, he works at ASM Lithography in Veldhoven as a designer in the metrology group of the software development department.

Acknowledgement

I would like to thank everybody who in some way made a contribution to the realisation of this thesis. In particular, I would like to thank:

- Eduard Hoogenboom and prof. dr. ir. H. van Dam for their contribution to my scientific education. I hope they are not disappointed in the result;
- prof. dr. R. Chawla, Rudi Seiler and Tony Williams, for the opportunity they offered me to work at HTR-PROTEUS;
- Tony Williams, for his help in the execution and analysis of experiments and the proof-reading of manuscripts. I also thank him and his family for their hospitality and the very enjoyable time I had in Switzerland;
- the HTR-PROTEUS team for their co-operation, good-fellowship and support;
- Piet de Leege and Addy Hersman, for their help to the calculational work;
- Hans Verhoef and Erdiñ Turkan, for providing the DSA-2 system and their support during its usage;
- Tim van der Hagen, for his continuing interest in my research;
- Rene van Geemert, for his company and help. I will never forget the numerous conversations that we had during the time we shared a room in 'barak C';
- all residents in 'barak C' and all colleagues of the reactor physics department, for their good-fellowship;
- Riny and Sonja, the mothers of the department, for their support and the organisation of the social events;
- my wife Wilma, for her love, assistance, and for listening to me, though she often didn't understand anything or only little of what I was telling about my research.

Erik

